UNIVERSITÀ
DEGLI STUDI
FIRENZE

DOTTORATO DI RICERCA IN FISICA E ASTRONOMIA

CICLO XXVIII

COORDINATORE Prof. Roberto Livi

MHD numerical models for the dynamics and non-thermal emission of Pulsar Wind Nebulae

Settore Scientifico Disciplinare: FIS/05 Astronomia e Astrofisica

Dottoranda
Dott. Barbara Olmi

Tutor
Dott. Luca Del Zanna

Coordinatore
Prof. Roberto Livi

Anni 2012/2013-2013/2014-2014/2015

Contents

Introduction

Pulsar wind nebulae (PWNe) are a particular class of supernova remnants, born in the violent death of massive stars as supernovae. They are characterized by the presence of a fast spinning neutron star, the pulsar, usually located at the explosion center, surrounded by the slow expanding debris of the supernova. The interaction of the relativistic wind emanating from the neutron star with its surroundings gives rise to the PWN. The effective confinement of the pulsar wind by the debris of the parent supernova explosion induces the formation of a termination shock at which the wind is slowed down and its energy is transformed into that of the magnetized relativistic plasma responsible for the nebular emission.

PWNe collect most of the rotational energy lost by their parent pulsars. As such they are a privileged location to look for answers to old and new questions in pulsar physics.

First of all, while pulsars are thought to be the primary leptonic antimatter factories in the Galaxy, a big open question concerns the exact amount of pair production in their magnetospheres, the so-called pair multiplicity. In this time of new observational and theoretical developments on the subject, modeling of PWNe is likely to provide the most solid constraints.

Moreover, the fact that PWNe are so close and bright, also makes them a perfect place for studying the physics of relativistic and magnetized plasmas.

PWNe are also extremely interesting from the point of view of particle acceleration: together with supernova remnants they are the most powerful accelerators in the Galaxy. While supernova remnants are thought to be the primary sources of hadronic cosmic rays in the Galaxy, in PWNe we have direct evidence of the presence of electrons with PeV energies (the highest energy observed in cosmic rays of Galactic origin). The acceleration of these particles is likely to be associated with the presence of a magnetized relativistic shock, an

environment where acceleration is most difficult to understand.

In recent years relativistic axisymmetric MHD models have proven to be excellent tools for describing the physics of such objects, and particularly successful at explaining their high energy morphology, down to very fine details. These models, however, have several problems at accounting for the spectral properties of the Crab nebula. The average magnetic field in the nebula results to be underestimated by a factor of $3 \div 4$ with respect to the observational estimations, which predict $< B >_V \simeq (200 \div 300)\,\mu$G. As a consequence the synchrotron emission can only be reproduced by assuming an enhanced number of emitting particles, respect to those predicted by spherical models. Moreover particles experience too low synchrotron losses on average, and the integrated spectrum must be artificially softened to fit the data: $N(E) \propto E^{-\alpha_p}$, with the spectral index $\alpha_p \simeq 2.8$ rather than the 2.2 predicted by various models. The artificial enhancement of the number of emitting particles is clearly visible when the Inverse Compton (IC) spectral emission is computed: the gamma-ray emission is in fact largely over-estimated.

Moreover, some important aspects of the physics of PWNe are still obscure: the mechanism(s) responsible for the acceleration of particles of all energies is (are) still unclear, and the origin of the lowest energy (radio emitting) particles is most mysterious. The correct interpretation of the origin of radio emitting particles is of fundamental importance, as this holds information about the amount of pair production in the pulsar magnetosphere, and hence on the role of pulsars as antimatter factories. On the other hand, the long lifetime of these particles against synchrotron losses, allows them to travel far from their injection location, making their acceleration site difficult to constrain. As far as the highest energy (X and gamma-ray emitting) particles are concerned, their acceleration is commonly believed to occur at the pulsar wind termination shock. But since the upstream flow is thought to have non-uniform properties along the shock surface, important constraints on the acceleration mechanism(s) could come from an exact knowledge of the location and flow properties where particles are being accelerated.

In this work we have investigated in detail both topics by means of 2D numerical MHD simulations. In Chap. 4 and 5 different assumptions on the origin of radio particles and more generally on the injection sites of all particles are considered, and the corresponding emission properties are computed. The physical constraints that can be inferred from a comparison of the synthetic emission properties with multi-wavelength observations of the PWN class

prototype, the Crab nebula, are discussed.

Despite 2D MHD models have proven to be very efficient in reproducing the high-energy emitting properties of the Crab nebula, they cannot obviously account for the whole dynamics of that object, since real PWNe are not 2D. In that sense full 3D modeling is absolutely mandatory.

A first attempt to model the Crab nebula within a 3D MHD framework was recently done, but only about the 10% of the Crab lifetime ($\sim$ 1000 yr) has been reproduced. As a consequence only preliminary results on the nebular dynamics and emission properties have been inferred. In particular the integrated spectrum is not evaluated, since emitting particles experience only a small part of their energetic evolution, too small to be able to reproduce the real spectral properties of the nebula. Since the IC emission is of extreme importance in constraining the number of emitting particle in the nebula, this is really important to be computed. These primary results must thus be confirmed and expanded by a long-term simulation, which can account for the whole energetic and magnetic evolution of the system, up to its actual age. At present we are still working on a full 3D simulation of the Crab nebula, and our preliminary results are presented and discussed in Chap. 6. We mean in particular to compute the complete emitting properties of the Crab, with special attention to the integrated spectrum, and to the IC emission. More comprehensive results are expected in the next few months.

This Ph.D. thesis is structured as follows: in Chap. 1 and 2 a general introduction about supernova remnants and PWNe is presented, with particular attention to the observational properties of PWNe and their theoretical modeling. A summary of the state of art of MHD numerical modeling of such objects is also given in 2. Our numerical model is introduced and discussed in Chap. 3, with reference to similar models and common results of the past years. As already mentioned, Chap. 4 and 5 are devoted the our newest findings on the radio particles origin and on particles acceleration at the wind termination shock of the Crab nebula. Chap. 6 contains our latest and preliminary results concerning the 3D numerical simulation of the Crab nebula. Finally, our conclusions have been drawn at the end of the manuscript.

Publications and communications concerning this thesis

Part of the research described in the present thesis (in particular the content of Chap. 4 and Chap. 5) has been presented in the following journal papers, conference proceedings and talks/posters at scientific workshops:

- B. Olmi , L. Del Zanna, E. Amato, N. Bucciantini and R. Bandiera, *Particle acceleration and non-thermal emission in Pulsar Wind Nebulae from relativistic MHD simulations*, **2015**, Journal of Physics: Conference Series, 642 012019, DOI: http://dx.doi.org/10.1088/1742-6596/642/1/012019;

- B. Olmi , L. Del Zanna, E. Amato, N. Bucciantini ,*Constraints on particle acceleration sites in the Crab nebula from relativistic magnetohydrodynamic simulations*, **2015**, MNRAS, 449, p.3149-3159, http://de.arxiv.org/abs/1502.06394;

- B. Olmi , L. Del Zanna, E. Amato, R. Bandiera, N. Bucciantini, *On the MHD modeling of the Crab Nebula radio emission*, **2014**, MNRAS, 438, p.1518-1525, http://de.arxiv.org/abs/1310.8496;

- **B. Olmi**, L. Del Zanna, E. Amato, N. Bucciantini, *On the MHD modeling of the Crab Nebula radio emission*, poster presented at: 28th Texas Symposium on Relativistic Astrophysics, December 13th – 18th 2015, Geneva, Switzerland;

- **B. Olmi**, L. Del Zanna, E. Amato, N. Bucciantini, R. Bandiera, *Particle acceleration and non-thermal emission in the Crab Nebula from relativistic MHD simula-*

tions , ISSI workshop 'Jets and Winds in Pulsar Wind Nebulae, Gamma-ray Bursts and Blazars: Physics of Extreme Energy Release', November 16th – 20th 2015, Bern, Switzerland;

- **B. Olmi**, L. Del Zanna, E. Amato, N. Bucciantini, *Winds from pulsars: constraints on particle acceleration mechanism(s) at the termination shock through relativistic MHD simulations*, 9th CNOC, September 22th – 25th 2015, Monteporzio Catone (Rome), Italy;

- **B. Olmi**, *How to cook your own Pulsar Wind Nebula*, PhD Day[6], May 27th 2015, Florence, Italy;

- **B. Olmi**, L. Del Zanna, E. Amato, N. Bucciantini, *On the MHD modeling of the Crab Nebula radio emission*, 14th AIAC, April 20th – 24th 2015, Tampa (FL), USA;

- **B. Olmi**, L. Del Zanna, E. Amato, N. Bucciantini, *On the MHD modeling of the Crab Nebula radio emission*, poster presented at: 40th COSPAR, August 2nd – 10th 2014, Moscow, Russia;

- **B. Olmi**, L. Del Zanna, E. Amato, N. Bucciantini, *On the MHD modeling of the Crab Nebula radio emission*, BOHEME, April 7th – 9th 2014, Bologna, Italy;

- B. Olmi, L. Del Zanna, E. Amato, **N. Bucciantini**, R. Bandiera *MHD modeling of Pulsar Wind Nebulae: from radio to X rays*, Astrospheres: From the Sun to Red Super Giants, December 9-13 2013 Lorentz Centre, Leiden, Holland;

- **B. Olmi**, L. Del Zanna, E. Amato, N. Bucciantini, *On the MHD Modeling of the Crab Nebula radio emission*, PICS mini-workshop on Pulsar Wind Nebulae and Cosmic Rays @LUMP, November 18th – 20th 2013, Montpellier, France;

- **B. Olmi**, L. Del Zanna, E. Amato, N. Bucciantini, *Open issues in relativistic MHD simulations of Pulsar Wind Nebulae*, Arcetri Workshop on Plasma Astrophysics, October 14th – 17th 2013, Florence, Italy;

- **B. Olmi**, L. Del Zanna, E. Amato, N. Bucciantini, *Axisymmetric MHD models of PWNe: critical issues*, poster presented at: Cosmic Accelerators School, Cargèse, Corse (France); PhD Day[5], Florence (Italy); SAIt LVII Congresso, May 7th-10th 2013, Bologna, Italy.

Chapter 1

Overview on the supernovae and supernova remnants zoo

Supernovae are of primary importance for the chemical evolution of the Universe: they have made most of the elements of nature, including those that form our planet, and they are one of the most important sources of energy for the InterStellar Medium (ISM). They also give birth to some of the most exotic states of matter known, as neutron stars and black holes.

The extremely violent death of a star as a supernova gives rise to a Supernova Remnant (SNR). SNRs are not only beautiful astronomical objects, but they are also of high scientific interest, because they provide insights into supernova explosion mechanisms and they are presumably sources of Galactic cosmic rays (CRs) up to $E \sim 10^{15}$ eV. Since supernovae explosions are rare events, about $2 \div 3$ per century in a typical spiral galaxy, SNRs provide the best way to study local supernovae. They also allow us to infer details on the explosion mechanism, that are difficult to extract directly from supernova observations. Another interesting aspect of SNRs is the physics of their high Mach[1] number and collisionless shocks, at which part of the explosion energy is converted into acceleration of cosmic rays.

In this Chapter we will briefly introduce the basic properties of supernovae and their remnants, from the final stage of stellar evolution to the SNRs classification.

[1]The Mach number of a shock wave is defined as the ratio between the shock propagation speed in the ambient medium and the sound speed in the same medium: $M = v/c_s$.

1.1 Stellar evolution basics

Standard stars are supported by the thermal pressure of hot gas, heated by nuclear reactions occurring in the central region. They spend the most of their life in the main sequence of the Hertzsprung-Russell (H-R) diagram, converting hydrogen into helium.

When the helium core reaches a mass of about $\sim 10\%$ of the total mass of the star, and the hydrogen in the core is exhausted, the star begins to move off the main sequence, to reach the giant branch. Here the inner regions of the star begin to contract and heat, and new nuclear reactions become feasible, burning heavier elements. As the evolution proceeds, also shells at larger radii attain the temperature and density required for trigger the reactions that produce progressively heavier elements. The duration of this phase depends on the mass of the star: from a billion years for a star with $M \sim M_\odot$ to an amount of the order of a million years for one with $M \sim 10M_\odot$, down to a few 10^5 years for the most massive stars.

If the star initial mass is less then $8M_\odot$, as the giant phase proceeds the dense matter in the core reaches the equilibrium in the degenerate electron gas state, supporting the star against gravitational collapse, even in the absence of nuclear reactions. The density and temperature reached by the core are not sufficient for the synthesis of the heavier elements, and their giant phase ends with an He-C-O core. The outer layers of the star expand up to a point where they are completely dispersed. The exposed remnant of the core becomes a white dwarf, a star composed by degenerate matter, supported agains gravity by the electron degeneracy pressure (Shapiro and Teukolsky, 1983).

Most massive stars ($M \gtrsim 8M_\odot$) are likely to proceed all the way through iron, continuing the sequence of contraction and synthesis of progressively heavier elements. The end point of this process is the iron group (elements with mass number A=56, consisting of isotopes of Cr, Mn, Fe, Co, Ni), since the synthesis of those elements into heavier ones consumes thermal energy, rather then releasing it. The final stage of this 'long contraction' phase is the formation of a neutron star or a black hole, depending roughly on the initial mass of the progenitor star (Woosley and Janka, 2005).

Along the way the contraction sometimes 'pauses' for millions of years, as nuclear fusion of new elements provides the energy necessary to replenish what the star is losing to radiation and neutrinos. Each time one fuel runs out, the star contracts, heats up and then starts to burn the next one. After helium burning the amount of neutrinos losses increases dramatically, and the evolution is accelerated. Although hydrogen and helium burning phases take millions of

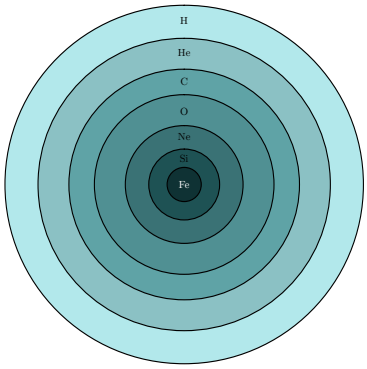

Figure 1.1: Schematic picture of the onion-like structure, and distribution of elements, of a massive star at the end of its evolutionary path via nuclear reactions, just before the core collapse phase.

years, silicon burning takes only about 20 days. Eventually an iron-group elements core of about $1.5 M_{\odot}$ is generated. Now the star has an onion like structure, with the heavier elements in the center, and the lighter in the outer shells (Fig. 1.1). Now temperature and density are high enough to activate two new processes that collaborate to take off the nucleus the energy it needs to maintain the necessary pressure and avoid the collapse: the photo disintegration and the neutronization.

In the photo disintegration processes energetic photons are absorbed via the endothermic reaction

$$\gamma + {}^{56}\mathrm{Fe} \rightarrow 13\,{}^{4}\mathrm{He} + 4\mathrm{n}\,, \tag{1.1}$$

consuming 28.3 MeV corresponding to the binding energy of an ^{4}He nucleus. Moreover, processes as

$$\begin{aligned} &e^- + p \rightarrow n + \nu_e\,, \\ &e^- + {}^{56}\mathrm{Fe} \rightarrow {}^{56}\mathrm{Mn} + \nu_\mathrm{e}\,, \\ &e^- + {}^{56}\mathrm{Mn} \rightarrow {}^{56}\mathrm{Cr} + \nu_\mathrm{e}\,, \end{aligned} \tag{1.2}$$

are likely to occur, leading to depletion of electrons, to the neutronization of the star, and to a substantial energy loss via neutrino emission. The amount of energy released with these processes is enormous, more than $10^{51} L_{\odot}$ (equivalent to $3{\times}10^{46}$ Js^{-1}), corresponding to about 10% of the rest-mass energy of the $1.5 M_{\odot}$ core.

The removal of the pressure support from the iron core, with such high densities, results in a collapse of the core on a time scale of the order of few seconds. Collapse continues until the core becomes a proto-neutron star: a hot, dense neutronic sphere with about 30 km radius. During the collapse, the core temperature increases and the reaction $e^- + p \rightarrow n + \nu_e$

becomes more and more common, while the inverse process of neutron decay $n \rightarrow e^- + p + \bar{\nu}_e$ is not so frequent. As a result most of the nucleons in the core are converted into neutrons.

If the mass of the stellar core is below a certain limit, an equilibrium is reached (with about $n_e = n_p \approx n_n/200$), and the nucleus ceases to collapse. The star is now a neutron star, supported against gravity by the degenerate pressure of neutrons (rather than electrons).

An estimation of the mass limit can be easily obtained from the Chandrasekhar mass, assuming an unitary ratio between the atomic and mass number of the star, $Z/A = 1$,

$$M_{ch} = 0.2 \left(\frac{Z}{A}\right)^2 \left(\frac{hc}{Gm_p^2}\right)^{3/2} m_p = 5.6 M_\odot \,. \tag{1.3}$$

Actually the previous value is lowered to about $2 \div 3 M_\odot$ taking into account both the effects of General Relativity and of the strong interactions of nuclear matter.

Stars with cores more massive than this limit cannot be stabilized against gravity, and nothing can stop the collapse. Those stars are fated to become black holes.

1.2 Supernova explosions

The time scale of gravitational collapse is inversely proportional to the density of the star $\tau_{\rm G} \propto (G\rho)^{-1/2}$ and thus the denser inner shells collapse before the outers, less dense. When finally the outer layers of the progenitor star begin to collapse toward the center, they found the just formed proto-neutron star on their way. A strong shock wave is generated when they hit the neutron star surface, which propagates outward and blows away the outer shells of the progenitor star. The ejection of this material into the interstellar medium (ISM) gives rise to the formation of the supernova remnant (SNR). The kinetic energy imparted to the ejected material is about $\sim 10^{51}$ erg (as determined from measurements of the mass and velocity of the ejecta). Even if only $\sim 1\%$ of that energy goes into luminosity, a supernova is an extremely luminous and impressive event: the mean luminosity during the first month after the explosion is of order $L_{\rm SN} \sim 10^9 L_\odot$, comparable to the the total luminosity of a small galaxy.

To our knowledge, during the last millennium, only five supernova events have been observed in our Galaxy (Fig. 1.2): SN 1006, SN 1054 (which gave birth to the Crab nebula), SN 1181 (associated to the SNR 3C 58), Tycho's supernova (observed in 1572) and Kepler's supernova (in 1604).

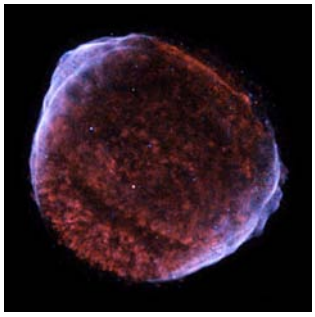

(a) Chandra's X-ray image of SN 1006. Thermal emission of the hot gases is in red/green, synchrotron emission is in blue.

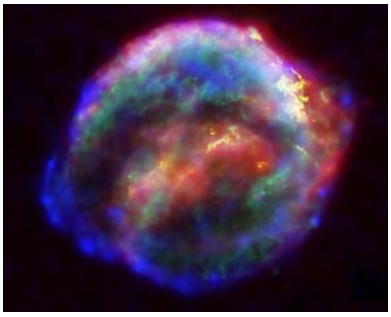

(b) X-ray, optical and IR composite image of the Kepler's SNR.

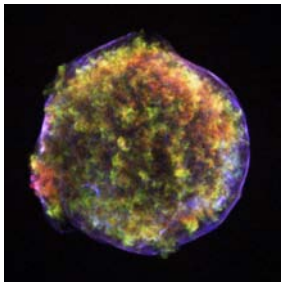

(c) False color X-ray image of the Tycho's SNR.

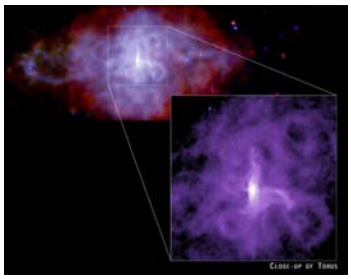

(d) Remnant of SN 1181 X-ray image (Chandra).

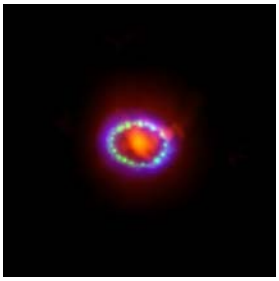

(e) Composite image of the SNR 1987A.

Figure 1.2: Fig. (a), (b), (c) and (d) show X-ray and composite images of some of the remnant associated with supernova events occurred in the Milky Way. Fig. (e) shows a picture of the SNR 1987A, occurred recently in the Large Magellanic Cloud. In red data from ALMA, showing the newly formed dust in the centre of the remnant, in green and blue Hubble and Chandra data show the expanding shock wave.

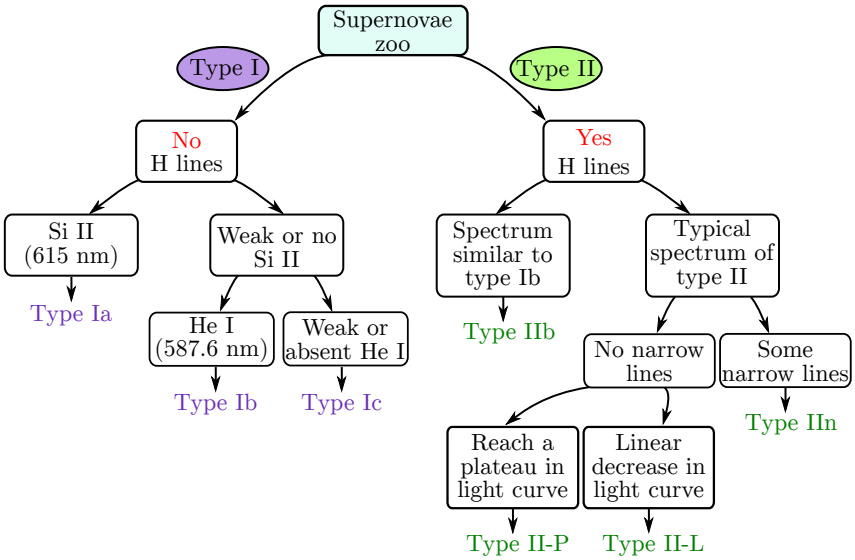

Figure 1.3: The zoo of supernovae classification.

Many other events have been recorded from other galaxies. The most recent bright supernova was SN 1987A, which exploded in the Large Magellanic Cloud in 1987, at a distance of $\sim$ 50 kpc from Earth, which reached an apparent magnitude 3 and was visible to the naked eyes from the southern hemisphere (shown in panel (e) of Fig. 1.2). This was the closest supernova observed since 1604, and it was crucial for understanding many aspects of the physics of supernovae.

Supernovae are classified into two principal types, depending upon the shape of their light curves and the nature of their spectra (the detailed classification is shown in Fig. 1.3). The key difference is the presence or the absence of the hydrogen Balmer series in the optical spectrum at peak light, and further sub-classifications are possible on the basis of more detailed analysis of the spectra. Type I supernovae are characterized by the absence of hydrogen lines, and sub-types are defined by looking at the presence or absence of ionized Silicon lines and neutral Helium lines. Type II supernovae show hydrogen lines, and the more detailed distinctions are based on the features of light curves.

The physical reason behind this classification is the presence, or the absence, of an hydrogen envelope in the progenitor star at the time of the explosion, which depends on the initial mass of the star and on its evolutionary path.

Type Ia supernovae are found in all types of galaxies, showing no preference for newly star forming regions, indicating that they are associated with old or middle-aged star forming regions. Type Ia are believed to be associated with the thermonuclear explosion of carbon-

oxygen accreting white dwarf stars.

On the contrary, all the other types of supernovae are found only in the vicinity of star-forming regions and are associated with core collapse events of massive stars.

1.2.1 Thermonuclear supernovae: type Ia

Type Ia supernovae are the most luminous ones, but also the most rare.

When a white dwarf is in a closed binary system, it can increase its mass by mass accretion from its companion star. When the C-O white dwarf approaches the Chandrasekhar limit of $M_{\rm Ch} \sim 1.4 M_{\odot}$, it would be no longer able to support itself against gravity through electron degeneracy pressure, and would begin to collapse (Janka, 2007). Actually it is not clear at all what kind of companion star is needed to trigger the supernova explosion: it can be a main sequence or evolved star, or even a double white dwarf system in a merger state (Vink, 2012).

When the star mass approaches $M_{\rm ch}$, the increase of temperature and density inside the core triggers the thermonuclear ignition of carbon. In the degenerate state, the white dwarf structure is insensitive to the rise in temperature ignited by thermonuclear reactions, and the nuclear reaction rate raises more and more. Within a few seconds, a substantial fraction of the star matter undergoes nuclear fusion, and the energy released can unbind the star in a supernova explosion (for a complete discussion see for example Woosley and Weaver (1986)).

Even though the picture of the accreting white dwarf is widespread accepted, the exact details of the explosion mechanisms are still not totally understood (for a complete discussion see Hillebrandt et al. (2000)).

1.2.2 Core-collapse supernovae

All the other types of supernovae are thought to be formed during the core collapse of massive stars, and represent the most frequent kind of supernovae events.

As previously discussed, when the progenitor star is a massive star ($M \gtrsim 8 M_{\odot}$), its evolution ends up with an iron core of about $1.5 M_{\odot}$, and an onion like structure with a specific burning product in each layer. Since the iron-group elements have the highest binding energy per nucleon, no further energy can be released and the star undergoes a gravitational collapse. Moreover the electron capture in iron-group nuclei, which converts electrons into neutrons

and releases neutrinos, represents another source of energy loss and also accelerates the star collapse. When the core collapses, it almost freely falls until the density reaches a value of about two times the nuclear density ($\sim 10^{14}$ g cm^{-3}). The core collapse is decelerated abruptly, and an undergoing shock wave is initialized by the outer layers crashing down upon the forming pro-neutron star. Originally it was believed this shock was the 'prompt mechanism' of the supernova explosion, expelling the outer layers of the star. It is now believed that the energy loss due to photo disintegration and neutrino emission is sufficiently great to cause the shock stalling while the proto-neutron star accretes matter from the outer layers at high rates (a few tenth of a solar mass per second).

The formation of the real neutron star depends on the duration of this accreting phase. According to Woosley and Janka (2005), if this accretion continued unabated for even one second, the proto-neutron star would be transformed into a black hole, and no supernova would explode. The reason for in some cases the accretion is stopped so rapidly to avoid the black hole formation is not totally clear. It seems that in massive stars, characterized by bigger iron-group nuclei and denser silicon and oxygen layers, accretion must be more rapid, quickly leading to the formation of a black hole.

The missing energy to trigger the explosion can be the absorption of neutrinos emitted by the proto-neutron star (Janka, 2007). However, numerical simulations have yet not been able to reproduce supernova explosions at all, suggesting that additional conditions are needed (Vink, 2012).

1.3 Supernova remnants

Supernova remnants are the aftermath of Supernova explosions, with the ejected material interacting with the ambient ISM. The resulting structure is of great scientific interest, as it provides insights into the Supernova explosion mechanisms, the cosmic ray production, and the chemical enrichment of the Universe.

Even though Supernovae can be classified in core collapse and thermonuclear/Type Ia Supernovae, it is often very difficult to establish the progenitor of a SNR. Today it is possible to determine the Supernova origin of a given remnant by means of X-ray spectroscopy in the very early stages, when the explosion is ejecta-dominated and it therefore still contains the fingerprints of the progenitor star (Vink, 2012). On the contrary, emission from the

oldest SNRs is no longer originated from the ejecta, and is thus difficult to trace back to the progenitor type. Only secondary indicators can be used for this aim. The most reliable one is of course the presence of a neutron star in the remnant, which should make the core collapse origin of the remnant almost clear . Unfortunately it is also possible that the observed central object is a foreground source, and therefore not related to the remnant at all (Kaspi, 1998). The location of the SNR can be also used as an indicator: it is in fact typical for core collapse Supernovae to occur in the Galactic disk, in star forming regions or OB associations, while Type Ia Supernovae are likely to occur above or below the Galactic plane, and associated with older stellar populations.

1.3.1 A very crude picture of SNRs evolution

The evolutionary path of a SNR can be roughly divided into four consecutive phases, irrespective of the remnant explosion type:

1. the ejecta dominated phase, when the expansion is almost free;
2. the Sedov-Taylor phase, when the ISM becomes dominant and the ejecta profile is not taken into account;
3. the 'snow plough' phase, when the expansion of the remnant is pressure driven;
4. the merging phase, in which the expansion becomes subsonic.

These phases have to be obviously considered only as guidelines for SNRs evolution, as the phases of a SNR are not always clearly determined and different parts of the same remnant can be in different evolutionary stages, since neither the remnant nor the ISM are homogeneous.

1. The ejecta dominated phase: free expansion of the ejecta in the ISM

Intially, when the total swept up mass of ISM, M_s, is much less then the ejected mass, M_{ej}, the expansion must proceed freely. Since the pressure gradient would be extremely large, the ejecta will impact the ISM with a velocity which is in every case much higher with respect to the typical speed of sound in the ISM, $c_s \simeq 10\,\mathrm{km\,s^{-1}}$ (Reynolds, 2008). In fact the impact velocity of the ejecta is about $10000\,\mathrm{km\,s^{-1}}$ for a SN Ia explosion and about $5000\,\mathrm{km\,s^{-1}}$ for

a core collapse event. The expansion velocity of the ejecta during the free expansion phase can easily be obtained from their kinetic energy $E_{\rm ej}$, as

$$v = \sqrt{\frac{2E_{\rm ej}}{M_{\rm ej}}}\,. \tag{1.4}$$

During this initial phase the supersonic behavior of the expanding ejecta drives the formation of a shock, the Supernova blast wave. The blast wave will sweep up, heat, compress and accelerate the ISM in which it expands. The free expansion of the ejecta behind the shock front goes on as long as $M_{\rm s} \ll M_{\rm ej}$. This phase will continue through the first few hundred years of the SNR lifetime, and it definitively ends when the swept up ISM mass becomes comparable with the ejected mass, namely:

$$\frac{4\pi}{3}\rho_0 R_{\rm s}^3 = M_{\rm ej}\,, \tag{1.5}$$

in which $R_{\rm s}$ is the radial position of the shock at the time of the equality $M_{\rm s} = M_{\rm ej}$. For typical values, $M_{\rm ej} \sim 10 M\odot$, $\rho_0 = nm_p = 10^{-24}$ g cm^{-3}, this leads to $R_{\rm s} = 4$ pc and $t_{\rm s} = 300$ yr.

When $M_{\rm S}$ approaches $M_{\rm ej}$, ejecta must decelerate as their density is lowered by expansion. As a consequence a rarefaction wave develops, moving inward towards the center of the remnant, lowering the expansion velocity of the ejected material and its pressure. Because of the low sound speed in the ejecta, this wave will transform into a reverse shock wave, which moves inward, heating up the material it encounters at sufficiently high temperatures to trigger X-ray emission. This emission is the last still containing the fingerprints of the progenitor star.

At this point, the structure of the SNR is the following (see Fig.1.4): the central region is still in free expansion, the reverse shock separates the freely expanding material from the decelerating one and a contact discontinuity separates the reverse shock from the forward shock of the expanding shell. The contact discontinuity is subjected to Rayleigh-Taylor instabilities[2] and small irregularities develop at its surface, which will grow and cause mixing of the inner and outer ejecta on large scales (Chevalier, 1976; Bandiera et al., 1984). This is a transient phase between free expansion and Sedov-Taylor evolution, in which the dynamic of the system is dominated by the interaction between the two shocks (the forward and reverse shock).

[2]Rayleigh-Taylor instabilities develop when a light fluid is accelerated into a denser one, because the interface between the two fluids can not remain sharp.

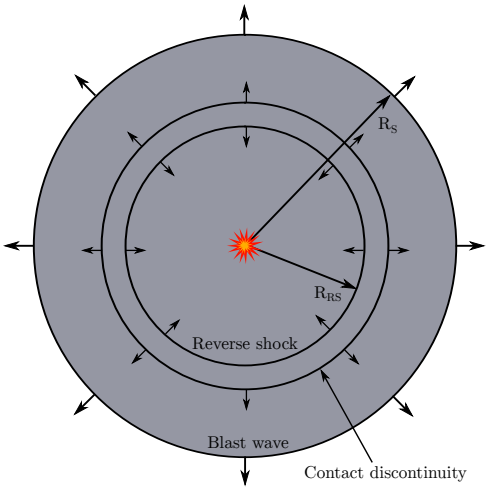

Figure 1.4: A schematic representation of a SNR in the ejecta dominated phase. Here R_S is the blast wave radius and R_{RS} the radius of the reverse shock. A contact discontinuity separates the shocked ISM from the shocked ejecta.

Since the density profile of ejecta can be assumed as a steep power law $\rho \propto r^{-n}$, with $n > 5$, and that of the circumstellar material as a shallow one, with $s < 3$, the early evolution of a core collapse SNR can be described by a self-similar solution (Chevalier, 1982; Vink, 2012)

$$R_s \propto t^{\beta}\,, \tag{1.6}$$

where $\beta = (n-3)/(n-s)$ is the expansion parameter. As it is a self-similar solution, its form does not change for different problems, and it is independent also on the time scale.

The two-shock phase can go on up to few thousand years and it will end when the reverse shock finally reaches the center of the remnant (Reynolds, 2008). This will happen at a time

$$t_{ST} \sim \left(\frac{M_{ej}}{10 M\odot}\right)^{5/6} \left(\frac{E_{SN}}{10^{51}\ \mathrm{erg}}\right)^{-1/2} \left(\frac{n_0}{1\ \mathrm{cm}^{-3}}\right)^{-1/3} \mathrm{kyr}\,, \tag{1.7}$$

where n_0 is the number density of the ISM. At this time the remnant effectively enters in the Sedov-Taylor phase.

2. The Sedov-Taylor phase

When finally the reverse shock has reached the innermost part of the remnant and the mass of the swept up material is sufficiently large, the remnant effectively enters the following phase.

Assuming the explosion as point-like and adiabatic, in which a finite amount of energy E was released in the uniform ISM with density ρ_0, the solution can still be described by a

self-similar expression, without considering the ejecta profile and radiation losses. Namely the radius of the shock front can be written as

$$R_{\rm s} = S(\Gamma)\left(\frac{E}{\rho_0}\right)^{1/5} t^{2/5}\,, \tag{1.8}$$

where S is a calculated function of the adiabatic index Γ, t is the age, E the explosion energy and ρ_0 the density of the surrounding medium. According to this, the velocity of the shock front decreases with time as

$$v_{\rm s} = \frac{2}{5}\frac{R_{\rm s}}{t} \propto t^{-3/5}\,. \tag{1.9}$$

3 and 4. The Snow-Plough and merging phases

When radiation losses cannot be neglected anymore, the Sedov-Taylor solution is no more applicable, since the adiabatic approximation breaks down. At this time the shock is slowed down to $\sim$ 100 km s^{-1}, and the remnant has grown to about 10 pc radius. Now the SNR expands according to momentum conservation

$$Mv_{\rm s} = \frac{4\pi}{3}R_{\rm s}^3\rho v_{\rm s} = \text{const.}\,, \tag{1.10}$$

where M is the mass of the swept up material and $v_{\rm s}$ the velocity of the forward shock. From the previous formula we can immediately find $R_{\rm s} \propto t^{1/4}$ and $v_{\rm s} \propto t^{-3/4}$.

The reason for the name 'snow-plough' is that during this phase the most part of the material is collected in a very tiny layer immediately downstream to the shock front, where the material is rapidly cooled down after shock heating. Since the shock is largely decelerated and the material is cooled down, in the snow-plough phase the most of the emission is concentrated at radio frequencies.

The expansion of the SNR continues with $R_{\rm s} \propto t^{1/4}$ until the remnants merges completely with the ISM, at the time at which the expansion velocity becomes subsonic.

1.3.2 Classification of supernova remnants

Since the Supernova progenitor type is so difficult to establish for certain, SNRs have their own classification, which is mostly based on their emission morphology. They are traditionally divided into three classes: shell-type remnants, plerions and composite SNRs.

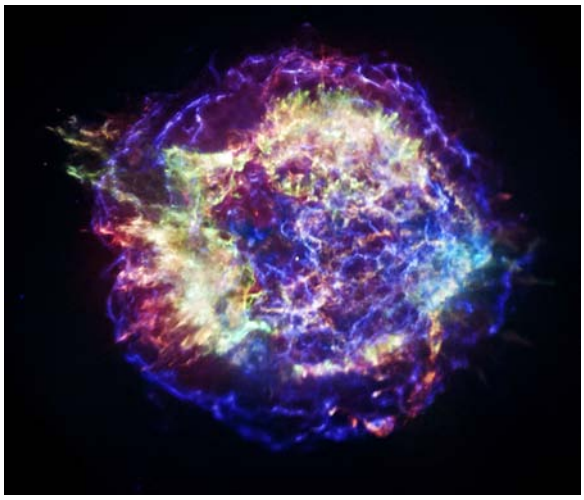

Figure 1.5: Cas A is a shell type Supernova remnant, and one of the most famous objects in the sky. The image is taken with the Chandra X-ray Observatory. *Image credit*: CHANDRA.

Shell-like supernova remnants

Shell-like remnants are the most common type in the Universe. The most famous example is Cassiopeia A (Fig. 1.5), Cas A in short, a core collapse remnant located in the Cassiopeia constellation. Also Tycho's and Kepler's, shown in Fig. 1.2, are famous examples of shell-type remnant, but their progenitor were Type Ia Supernovae (Ferrand and Safi-Harb, 2012). Shell-type remnants emit most of their radiation from a shell of shocked material. As the shock wave from the explosion ploughs through space, it heats and stirs up the interstellar material it encounters, producing a big shell of hot material. Since at the edge of the remnant shell the quantity of shocked (hot) material along our line of sight is bigger than in the middle, these remnants are seen with a ring-like morphology (limb brightening effect). The shell region is a source of both X-ray continuum emission and line emission from ionized elements, and its spectral properties can tell us about the Supernova nucleosynthesis and initial properties.

In the case of a very bright remnant, the shell can be resolved in such great detail, that it is possible to distinguish different regions and the contact discontinuity separating them. The positions of the blast wave and of the reverse shock can be determined from a surface brightness profile, where the two are indicated by distinct peaks. The ratio between these two quantities is a strong indicator of the evolutionary stage of the remnant. This value was determined for instance for Cassiopeia A, where the reverse shock and the blast wave shock appear to be quite close one another. Since the Sedov-Taylor phase will set up approximately

Figure 1.6: The Crab nebula in a composite image from the Hubble Space Telescope. *Image credit*: NASA, ESA.

in the time the reverse shock reaches the core of the ejecta, Cas A must be in the transition phase between the ejecta-dominated phase and the Sedov-Taylor one (Gotthelf et al., 2001).

Probably the most intriguing and relevant thing about these remnants is that observation of the forward shock and the precursor can reveal the presence of an efficient particle acceleration (see for example Morlino (2013) and references therein).

Pulsar wind nebulae

Pulsar wind nebulae (PWNe), or plerions[3] are also known as Crab-like remnants, from the most famous PWN and class prototype, the Crab nebula (Fig. 1.6). They are formed as a result of a core collapse Supernova, but it is important to stress that not all core collapse Supernovae become PWNe: the presence of a neutron star in the remnant does not guarantee the formation of a plerionic remnant (Vink, 2012).

PWN are bubbles of relativistic particles inflated by the relativistic and magnetized outflow emanating from the pulsar, the so called 'pulsar wind' (PW). Plerions allow us to probe the interaction between neutron star relativistic winds and their surroundings, consisting in the Supernova ejecta at the earlier stages of SNR evolution, the shocked ISM or Supernova blast wave as the neutron star encounter the expanding SNR shell, and the ISM after the neutron star has left its parent SNR. Moreover they seed the Galaxy with highly energetic particles and strong magnetic fields, and are thus considered efficient engines for cosmic ray acceleration up to PeV energies.

PWNe are characterized by very broad band emission, ranging from radio to γ-rays fre-

[3]From the Greek term 'pleres', meaning full.

quencies. Their spectrum is dominated by non thermal synchrotron emission from relativistic particles injected by the neutron star from radio up to X-rays, and by Inverse Compton scattering (IC) at higher energies. They are characterized by an enhanced brightness towards the center, which makes them easily distinguishable from shell-type remnants, which show a limb-brightened morphology. The X-ray size of a PWN is smaller than its radio and optical size, due to the shorter synchrotron life time of the higher energy electrons (the synchrotron burn-off effect). They also show flat radio spectral indices ($-0.3 \lesssim \alpha_r \lesssim 0.0$) and much steeper ones in X-rays ($\Gamma_X \equiv \alpha_x - 1 \sim 2$), which imply one or more spectral breaks between these two frequency bands (Gaensler and Slane, 2006).

PWNe properties will be extensively discussed in Chap. (2).

Bow shock nebulae

It has been estimated that about $10\% \div 50\%$ of the pulsars are born with kick velocities of the order of 500 km s^{-1} (Arzoumanian et al., 2002).

The expansion of the SNR shell is decelerated by mass loading by the swept up ISM, or some residual material from the progenitor wind. Since the pulsar moves with almost constant velocity, it is fated to escape its parent SNR in less than 20000 years.

Since typical sound speeds in the ISM are $c_s \simeq 10 \div 100$ km s^{-1}, these pulsars are moving with highly supersonic velocities into the ISM. Moreover their escape time scale is sufficiently short, with respect to the pulsar age, to allow the star to produce even powerful relativistic winds. The interaction of such winds with the ISM produces the so called 'bow-shock' nebulae, characterized by a cometary morphology, with the pulsar in the head and an extended tail of emission. If the ambient medium is partially ionized, they can be usually revealed as Hα nebulae, with emission mainly due to charge exchange and/or collisional excitation of neutral hydrogen atoms in the post-shock flows (Chevalier et al., 1980).

Up to now only nine bow-shock nebulae have been detected (Brownsberger and Romani, 2014). A famous example of bow-shock nebulae with the pulsars still inside the remnant is IC 443 (Bocchino and Bykov, 2001), also known as the 'jellyfish nebula', in which the elongated emission and the spectral index map suggests that the pulsar is already moving inside its SNR (Fig. 1.7).

CTB80 is an example of bow-shock nebula in which the pulsar is going to escape its SNR (Fesen et al., 1988). Here the pulsar PSR B1951+32 is located just at the outer edge of

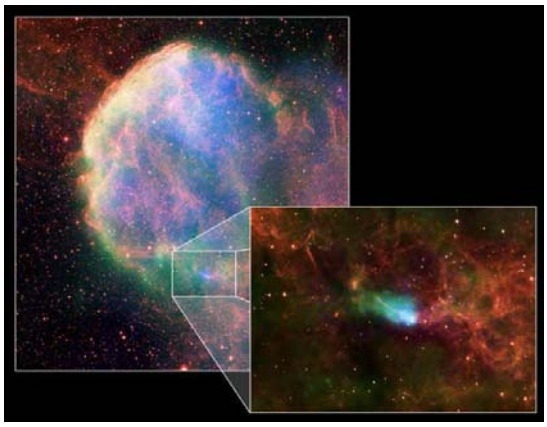

Figure 1.7: The IC 443 Supernova remnant and pulsar, in a composite image from Chandra, Rosat, VLT and DSS. The close-up inset shows the swept-back trail created as the neutron star rushes through the hot gas.

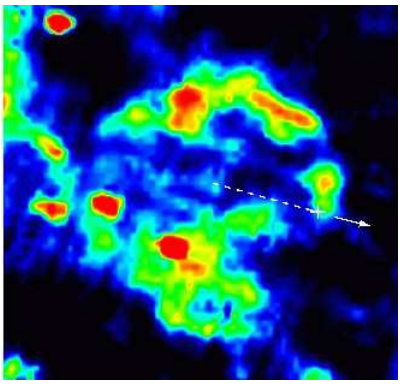

Figure 1.8: The SNR CTB80 and PSR B1951+32, which position is indicated by the plus sign. Pulsar motion from its birthplace at the center of the remnant is represented by the dashed arrow.
Image credits: VLA.

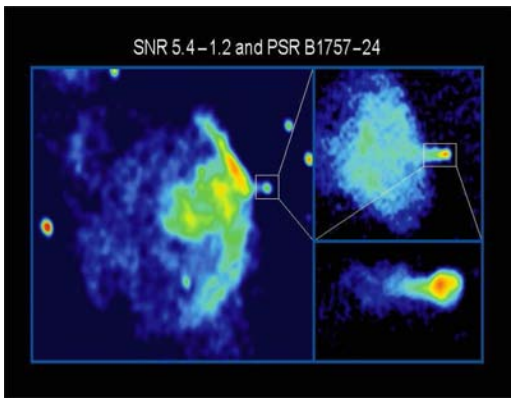

Figure 1.9: Color representation of radio emission from the supernova remnant G5.4-1.2 (large scale image) and the associated pulsar B1757-24 (insets). Blue indicates fainter radio emission, yellow and orange more intense radio emission. *Image credits*: NRAO/AUI .

the remnant (Fig. 1.8). Synchrotron emission shows that the pulsar lays in a narrow finger of emission that protrudes from the main body of the PWN.

In G5.4-1.2 the pulsar B1757-24 appears to have just emerged from the remnant, and it is located at a tip of a flat spectrum radio protuberance just outside the remnant shell as shown in Fig. 1.9 (Frail and Kulkarni, 1991; Gaensler and Frail, 2000). The pulsar and the shell together are dubbed 'the duck' because of their unusual appearance.

Hydrodynamical (HD) simulations of bow-shock nebulae predict that the wind is terminated in the same way of standard PWNe. It results in a double-shock structure: a forward shock where the ISM is heated, and a termination shock (TS), where the energy density of the free wind balances the external pressure in the same way as in the case of standard PWNe. The main difference is in the TS shape, which is extremely elongated in the case of bow-shock nebulae, giving rise to particular emission morphology. Particles shocked at the TS behind the pulsar are thus confined to a cylindrical narrow region trailing behind the pulsar, giving rise to the 'tail', while particles shocked in front of the pulsar spread out and create a larger and broader structure, the 'head'. By comparing HD simulations with observations, it results that X-ray emission is mainly associated to the termination shock, while the more diffuse lower energy emission is due to the shocked wind (Bucciantini, 2002; Bucciantini et al., 2005a).

Spectra of bow-shock nebulae are expected to be similar to those of standard PWNe: a non-thermal spectrum characterized by a spectral softening with increasing distance from the pulsar (Gaensler et al., 2004).

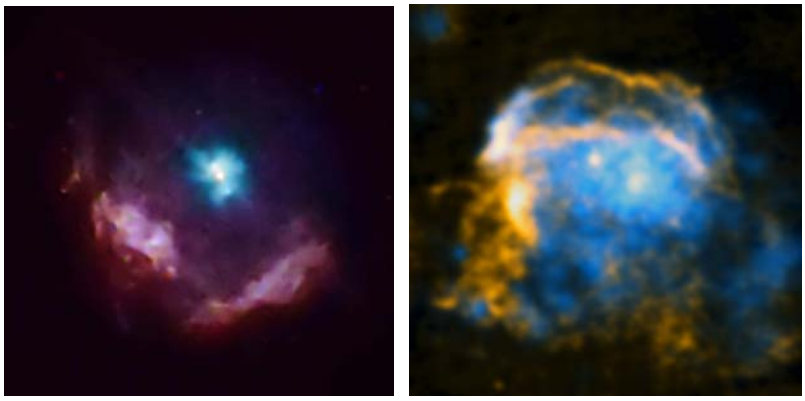

Figure 1.10: *Left panel:* The composite SNR Kes 75, observed by Chandra. The inner pulsar wind nebula has an hard X-ray spectrum. Red and green colors indicate emission from gases, blue indicates mostly the continuum emission from the pulsar wind nebula (Helfand et al., 2003).
Right panel: The thermal composite SNR W28 as observed in X-rays by Rosat PSPC (blue) and in radio by VLA (Dubner et al., 2000).

Composite remnants: plerionic and thermal composites

Some objects are a cross between shell-type and Crab-like remnants. They appear shell-like, Crab-like or both depending on the wavelength of observation. They are divided in two kinds: plerionic composites and thermal composites.

Plerionic-composites show a central filled morphology in X-rays, with the central part being a PWN, while they have a shell type morphology at radio frequencies.

Thermal-composite remnants, also referred as mixed-morphology, are a relatively new class and they are only poorly understood. They are characterized by a centrally dominating thermal X-ray emission and a shell-like appearance in radio. The most famous explanation for this appearance at X-rays is that of clouds surviving the interaction with the remnant forward shock, and subsequently starting to evaporate in the center of the remnant (White and Long, 1991).

They are older remnant, and thus they usually have reach pressure equilibrium, leading to a rather homogeneous density (Vink, 2012). Some of them also show continuum emission from radiative recombination in their spectra, which suggests that they are close to the ionization equilibrium.

Examples of composite remnant (left side) and thermal composite remnant (right side) are shown in Fig. 1.10.

Chapter 2

Pulsar Wind Nebulae

As briefly introduced in the previous chapter, PWNe are a particular class of supernova remnants, born in the core collapse supernova explosion of a massive star ($M \gtrsim 8\ M_{\odot}$). The nucleus of the progenitor star gives rise to a highly magnetized, rapidly rotating neutron star, often observed as a pulsar, that emits a magnetized relativistic wind (the Pulsar Wind, PW). Effective confinement of the PW by the slowly expanding debris of the explosion induces the formation of a Termination Shock (TS), at which the flow is slowed down and heated. The Pulsar Wind Nebula arises downstream of this shock as non-thermal emission of the shocked material.

PWNe are interesting objects from several points of view. The first obvious reason is that they enclose the most of the pulsar spin-down energy (in the sense that most of the MHD energy released in the pulsar spin-down process is deposited in the nebula in the form of Poynting flux and energetic particles), and so they are the perfect place to look at for investigating open questions in pulsar physics.

Moreover pulsars have an important role as galactic antimatter factories, and the knowledge of the exact amount of pair production in their magnetospheres can be fundamental in understanding the cosmic ray positron excess measured by PAMELA coll. (2009) and AMS-02 coll. (2013).

Moreover, the fact that they are so close and bright makes them a perfect place for studying the physics of relativistic magnetized plasmas.

PWNe are also extremely interesting from the point if view of particle acceleration. Together with Supernova remnants they are the most powerful accelerators in the Galaxy. While Supernova Remnants are thought to be the primary sources of hadronic cosmic rays (CR) in

the Galaxy, in PWNe we have direct evidence of the presence of electrons with PeV energies (the highest energy observed in CR of Galactic origin). The acceleration of these particles is likely to be associated with the presence of a magnetized relativistic shock, an environment where acceleration is most difficult to understand, and the acceleration mechanism at work still represents a deep mystery.

2.1 Emission from PWNe

At present time about 100 PWNe are known, and they all show common features: a center-filled emission morphology, flat radio spectra and very broad band non thermal emission, usually extending from radio frequencies to X-rays or even γ-rays (Gaensler and Slane, 2006; Kargaltsev et al., 2013). The radio synchrotron emission is characterized by a power law distribution of the observed flux density $S_\nu \propto \nu^{\alpha_r}$, with α_r the spectral index in radio. Usually at higher energies the emission is described as a power law distribution of photons $N_E \propto E^{-\Gamma}$, with $\Gamma = 1 - \alpha_x$ the photon index and N_E representing the number of emitted photons in the energy range between E and $E+dE$. Typical indices for PWNe are $-0.3 \lesssim \alpha_r \lesssim 0$ and $\Gamma \simeq 2$, that imply a spectral steepening with increasing energy, and thus one or more spectral break between radio and X-ray frequencies. The frequency of the spectral break is proportional to the magnetic field in the nebula $B_{\rm PWN}$ (Ginzburg and Syrovatskii, 1965)

$$\nu_b = 10^{21} \left(\frac{B_{\rm PWN}}{10^{-6}\,{\rm G}}\right)^{-3} \left(\frac{t}{10^3\,{\rm yr}}\right)^{-2} {\rm Hz}\,. \tag{2.1}$$

Particles emitting at frequencies beyond ν_b reach the outer portions of the nebula in a diminishing number, most of them radiate all their energy before traveling so far from the pulsar. As a result the observed size of the PWN decreases with increasing energy, as clearly visible in the Crab nebula (Fig. 2.2). This is a natural effect of the synchrotron emission (the 'burn-off effect'): the more energetic the particles are, the shorter their synchrotron life time is ($\tau_{\rm sync} \propto 1/\gamma$). For PWNe with low magnetic field this effect is less stronger, leading usually to comparable dimensions in radio and X-rays (this is the case of 3C 58, Fig.2.1).

2.1.1 The Crab Nebula: the PWN prototype

Thanks to its proximity ($\sim$ 2 kpc) and to the high power it emits, the Crab nebula (Fig. 2.2) is unique among PWNe, and it is logically considered the prototype of the whole class. It is

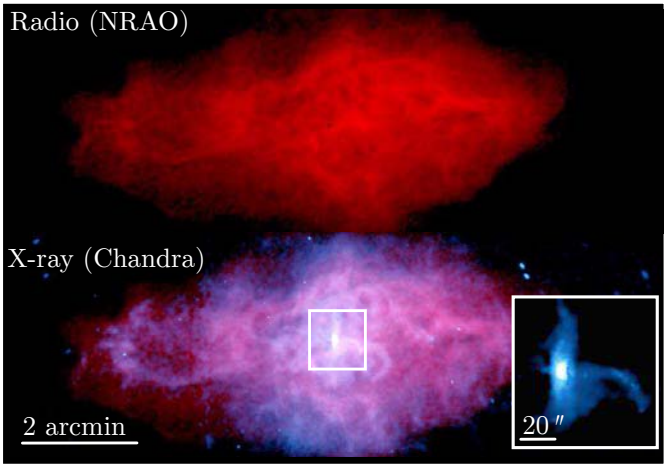

Figure 2.1: Radio (top row) and X-ray/optical (bottom row) images of the PWN 3C 58. In the right box the X-ray torus is expanded. The size of radio and X-ray images are comparable

thus one of the best studied objects in the sky, and the one from which we have learnt most of what we know about PWNe (Hester, 2008).

The Crab nebula is almost certainly associated with a supernova explosion observed by Chinese astrologers in 1054 AD. They reported that the 'guest' star was visible during daytime for three weeks, and was visible for 22 months at night (Stephenson and Green (2002) and references therein). The remnant was then rediscovered in 1731 by John Bevis. The first set of observations came a few years later, thanks to Charles Messier, and the Crab became the first object of its famous catalog of nebulous non cometary objects (with the name M1). Its current name was given it by William Parsons, third Earl of Rosse, who first observed its appearance in 1840 with a 90-cm reflecting telescope and produced a drawing that looked somewhat like a spider crab (Fig. 2.3).

The connection between the historical event of 1054 AD was first suggested by Lundmark (1921), but it became clear only in 1942, when Duyvendak (1942) and Mayall and Oort (1942) presented complete studies of the nebula expansion compared with Chinese records.

The central engine of the Crab nebula is a rapidly rotating young neutron star. It was first presumed with theoretical arguments by Pacini (1967), some months before the star pulsed signal was indeed detected at radio and optical wavelengths (Staelin and Reifenstein, 1968; Cocke et al., 1969). The spinning neutron star, or 'pulsar', has a period of 33 ms, which is slowly increasing with time $\dot{P} = 4.21 \times 10^{-13}$. This observed rate of spin-down implies that kinetic energy is dissipated at a rate of $L \sim 5 \times 10^{38}$ erg s^{-1}, or $130{\times}10^3$ L$_\odot$, a value similar to the inferred rate at which energy is supplied to the nebula (Gold, 1969). The Crab

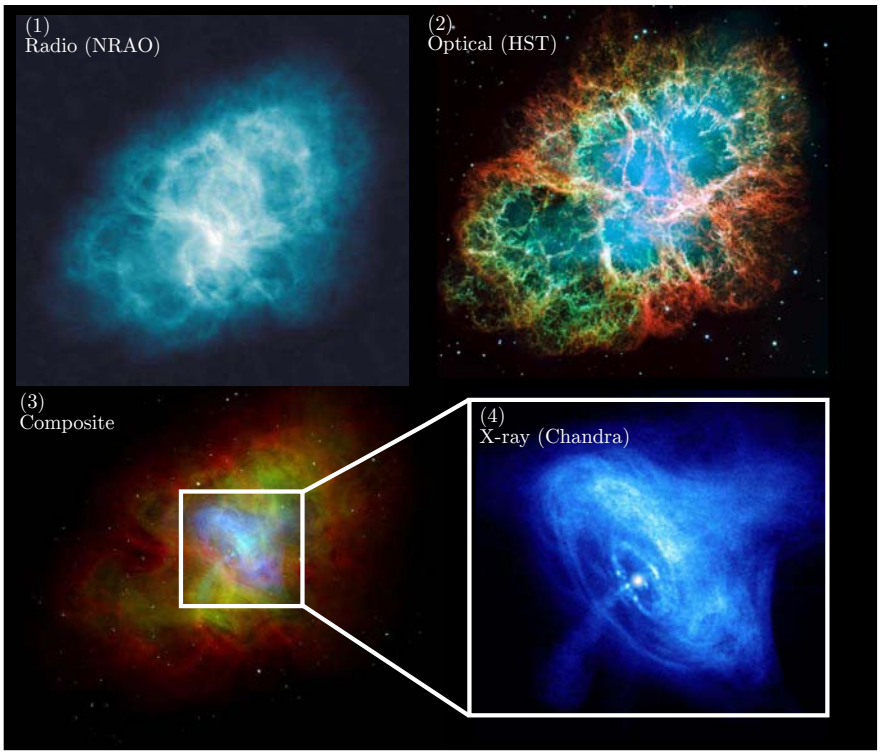

Figure 2.2: Images of the Crab nebula at different wavelengths. (1) Radio synchrotron emission from the confined wind, with enanchements along the thermal filaments. (2) Optical synchrotron emission (blue and green colors) surrounded by emission lines from the filaments (red color). (3) Composite image of the radio (in red), optical (green) and X-ray emission (blue). (4) The X-ray synchrotron emission from polar jets and equatorial torus. Note the decreasing size of the nebula from the composite image to the X-ray one.

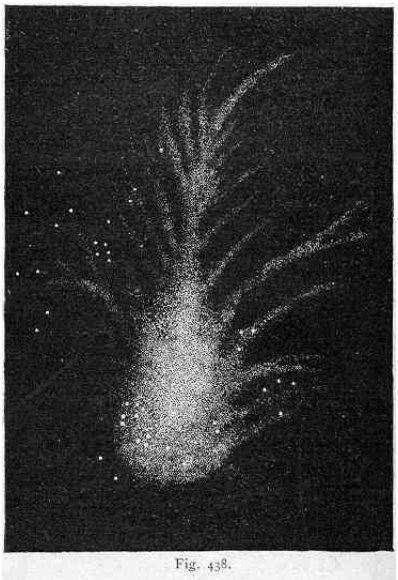

Figure 2.3: A graphical representation of the first observation of the Crab nebula by W. Parsons, in 1840.

pulsar is the most powerful pulsar inside a PWN. Among the known PWNe only two other pulsars present the same spin-down energy, but they are located at ~ 50 kpc from us. Pulsars which are at comparable distances, in the range between 1 and 5 kpc, are characterized by a spin-down luminosity weaker of $1 \div 5$ orders of magnitude.

Later on a theoretical modelization was soon developed: the central pulsar generates a magnetized wind of particles, mainly positron and electrons, which radiate synchrotron emission across the electromagnetic spectrum (Pacini and Salvati, 1973; Rees and Gunn, 1974). Electrons and positrons are generated in the pulsar magnetosphere, where they are extracted from the star by the strong electric field present at its surface interacting with photons and generating pair cascades, as we will discuss in the following (see Sec. 2.2.2).

Only a small fraction of the spin-down energy of the pulsar, of the order of 1%, is converted into pulsed emission. The most of the energy is effectively carried away by the highly magnetized plasma made up of electrons and positrons generated by the pulsar magnetosphere, with maybe a small component of hadrons (ions), eventually extracted by the neutron star surface (Gallant and Arons, 1994). This energy is then converted into synchrotron emission with an high efficiency (about 20%), as pointed out in Kennel and Coroniti (1984b).

As expected, the Crab nebula spectrum is very broad-band (Fig. 2.4), with primary emission extending from radio frequencies to $\nu \sim 10^{22}$ Hz, due to synchrotron radiation produced by relativistic particles interacting with the intense ($\sim 100 B_{\rm ISM}$) and highly ordered magnetic field of the nebula. At higher energies (up to $\nu \sim 10^{28}$ Hz), the emission is produced via the Inverse Compton scattering process, between electrons and different target photon fields. The most important of these are photons produced by synchrotron emission, photons from the Cosmic Microwave Background (CMB) and thermal photons emitted by warm dust. Dust, in the form of silicates and graphite at $T \simeq 40 - 50$ K, is a common left over of SN explosions, and in the Crab nebula its thermal emission produces a 'bump' in the spectrum at infrared frequencies.

High resolution images at optical frequencies are obtained thanks to the *Hubble Space Telescope* (HST), as that shown in Fig. 2.2. Filamentary finger-like structures characterize the outer nebula at these wavelengths, visible as thermal emission. Filaments are produced by Rayleigh-Taylor instabilities between the fast expanding nebula and the slow moving supernova ejecta.

In the last decade, the *Chandra* X-ray observatory also allowed us to observe the high

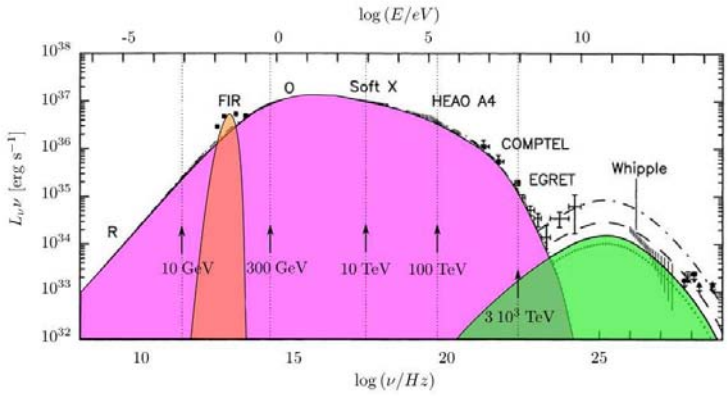

Figure 2.4: The integrated spectrum of the Crab nebula, from Atoyan and Aharonian (1996). The electron energies shown correspond to peak synchrotron emission assuming an ambient magnetic field of 300 μG. The red low energy bump indicates the thermal emission from dust residuals of the explosion, while the most of the emission is between optical and X-ray frequencies, as synchrotron emission (pink zone). The higher energy emission is due to IC radiation (green zone).

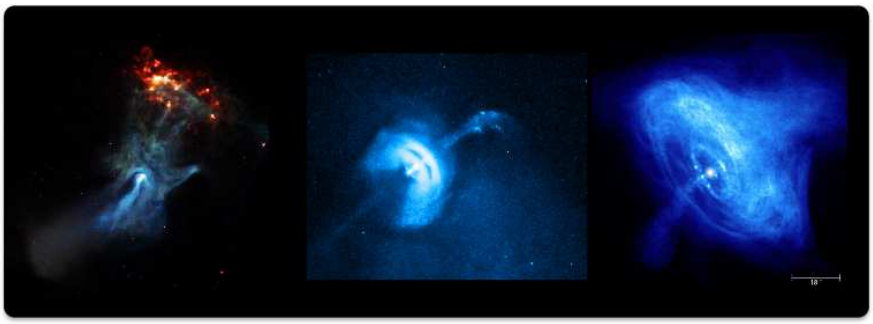

Figure 2.5: Some X-ray pictures of PWNe showing clearly the jet-torus morphology. From left to right: PSR B1509-58, the 'Hand of God' nebula, the Vela and finally the Crab.

energy emission properties of PWNe with great detail. A very puzzling jet-torus morphology was seen in the Crab nebula and some other PWNe (Fig. 2.5). The presence of polar jets was the most intriguing feature, since they appeared to originate so close to the pulsar location that collimation upstream of the TS seemed to be required. The best candidate mechanism for jet collimation in PWNe appeared to be magnetic collimation, but this can be shown to be very inefficient in ultrarelativistic flows, such as the flow upstream of the TS is (Lyubarsky, 2002; Bogovalov and Khangoulyan, 2002). The curvature radius of a field line can be expressed as a function of the cylindrical radius r and the Lorentz factor as $R_c \propto r\gamma^2$. In the case of an ultra relativistic wind $\gamma \gg 1$ and flow lines are almost straight, and collimation is possible only near to the axis. In the ultra-relativistic case the collimation in the upstream is strongly suppressed, since $\rho_e \vec{E} + \vec{J} \wedge \vec{B} = 0$, while in the downstream, the first term of the

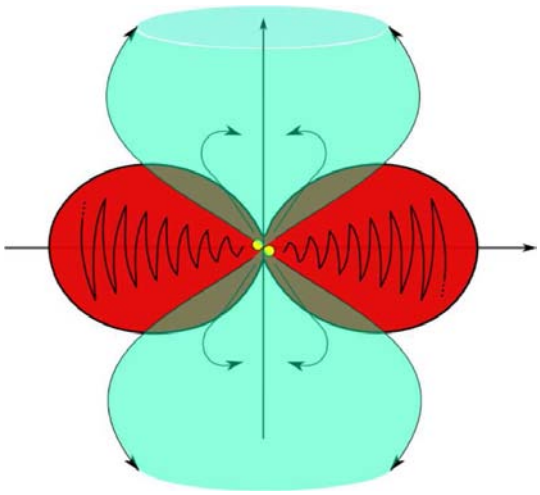

Figure 2.6: The graphic representation of the oblate TS (in red) and polar jets (in light blue). Collimation of jets takes place near to the polar axis, where the TS is closer to the pulsar. In yellow is represented the pulsar closed magnetosphere. Note that the picture is not in scale, since $R_{\rm TS} \simeq 10^9 R_L$.

previous relation tends to vanish, and the collimation become feasible.

The termination shock must be highly non spherical. Hoop stresses[1] squeeze the post-shock flow near to the axis, and consequently the pressure is sufficiently enhanced to push the shock closer to the pulsar. Since the most of the energy is transported along the equator, the termination shock is more expanded in the equatorial direction, assuming a characteristic oblate shape (Fig. 2.6) This behavior was then confirmed by different numerical simulations (Komissarov, 2004; Del Zanna et al., 2004; Bogovalov et al., 2005), that also show that collimation by hoop-stresses can be effective immediately beyond the TS near to the polar axis, where the wind decelerates.

Thanks to *Chandra* many different bright and variable features were also found, as *knots*, *rings* and *wisps* in the inner region of many PWNe. Thanks to the higher available resolution, these features were first identified and studied for the Crab nebula (Weisskopf et al., 2000).

The Crab torus appears to be composed by several rings. At a distance of ~ 0.1 pc from the pulsar, the *inner ring* is perfectly visible. Crab's wisps were first observed by Scargle (1969), who identified many arc-like, shining, periodic structures, which move outward from the inner ring with mildly relativistic velocities ($v \lesssim 0.5c$). The life time period of wisps is of the order of days, months or years, depending on the wavelength of observation (X-rays, optical and radio respectively). In Fig. 2.7 wisps are visible in consecutive images taken by HST between August 2000 and April 2001. As we will see in the following, since wisps

[1] Hoop stresses are the expression of the magnetic tension generated by the toroidal magnetic field.

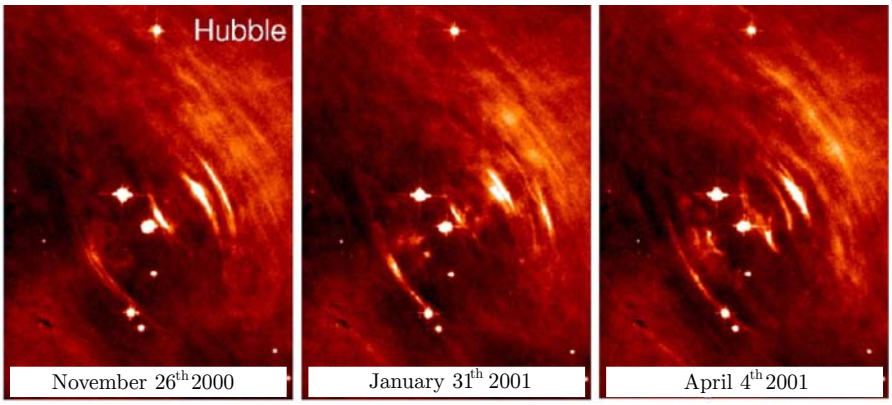

Figure 2.7: Wisp variability in an HST images collection of the Crab nebula.

originate close to the TS, where the flow is highly turbulent and swirling, they represent a perfect tool to investigate the plasma's physical conditions at the shock surface.

Other variable features has been successively observed by van den Bergh and Pritchet (1989) as point-like structures that always appear and fade out in the same locations. They are visible at all the wavelengths. In the optical band the most luminous knot (knot-1) is located at 0.65″ from the pulsar, while the second brightest is at a distance of 3.8″. Knots are aligned with the polar jet in the SE direction. The bright ring at the center of the torus is likely to be associated with the TS (Weisskopf et al., 2000). The inner ring semi-major axis is 14″ along NE-SW and the semi-minor axis is 7″ in the NW-SE direction.

2.2 Overall properties

In this section we will resume some of the key theoretical models of PWNe, starting from an introduction on pulsars emission properties up to PWNe models.

2.2.1 The pulsar spin-down mechanism

As the source of the observed emission from a PWN is the spin-down of the pulsar, we need to understand the spin evolution of a young pulsar. As a first approximation the physical mechanism can be conveniently described with the simple model of the oblique rotator by Pacini (1967).

Le us consider the pulsar as an isolated, rotating, rigid sphere with radius $r_\star$ and angular velocity ω around the z axis (as schematized in Fig. 2.8). The magnetic moment $\vec{\mu}$ of the

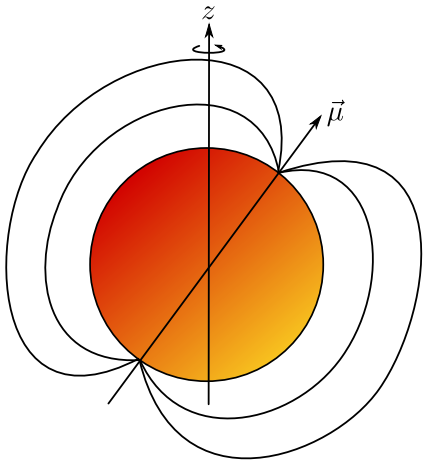

Figure 2.8: Schematic representation of a pulsar in the oblique rotator model (Pacini, 1967).

dipolar field of the pulsar, with an inclination angle α with respect to the rotational axis, is

$$\vec{B}(\vec{r}) = \frac{3\hat{r}(\vec{\mu}\cdot\hat{r}) - \vec{\mu}}{r^3} \,. \tag{2.2}$$

The power emitted by a magnetic dipole is

$$\frac{dW}{dt} = -\frac{2}{3c^3} \mid \ddot{\vec{\mu}} \mid , \tag{2.3}$$

where $\ddot{\vec{\mu}}$ is the second time derivative of the dipole moment μ. By expressing $\vec{\mu}$ in polar coordinates, referring to the z axis ($\vec{\mu} = \mu(\cos\omega t, \sin\omega t, \cos\alpha)$), we can easily obtain the so-called 'Pacini's formula'

$$\frac{dW}{dt} = -\frac{B_p^2 r_\star^6 \omega^4 \sin^2\alpha}{6c^3} \,, \tag{2.4}$$

in which $B_p = 2\mu/r_\star^3$ represents the magnetic field of the star at the pole.

The spin-down luminosity of the pulsar is the rate at which its rotational energy is dissipated

$$\dot{E} = -\frac{dE_{\rm rot}}{dt} \,. \tag{2.5}$$

The variation of the rotational energy with time is $dE_{\rm rot}/dt = d(I\omega^2/2)/dt = I\omega\dot{\omega}$, with I the star moment of inertia, that it is usually assumed to be $I \sim 10^{45}$ g cm^{-2}.

By matching Eq. 2.2.1 and Eq. 2.5, we finally find

$$\dot{\omega} = -\frac{B_p^2 \omega^3 r_\star^6 \sin^2\alpha}{6Ic^3} \,. \tag{2.6}$$

As expected from observations, this variation is negative, and thus the rotation slows down with time.

The whole argument can be generalized without specifying the physical mechanism at the base of the energy losses, considering a spin-down law such that $\dot{\omega} = -K\omega^n$, with K being a proportionality constant and n the 'braking index'. Integrating this expression between the initial values (ω_0, t_0) and the general ones (ω, t), we can obtain an expression for the age of the system

$$\tau \equiv (t - t_0) = -\frac{\omega}{\dot{\omega}(n-1)}\left[1 - \left(\frac{\omega}{\omega_0}\right)^{(n-1)}\right], \tag{2.7}$$

The braking index has been confidently measured only for a few pulsars, in each case falling in the range $2 < n < 3$ (Livingstone et al., 2005). The value $n = 3$ corresponds to the spin-down via magnetic dipole radiation. If we assume this value for the rest of the pulsar population, and assuming $\omega_0 \gg \omega$, eq. 2.7 reduces to the so called 'characteristic age' of a pulsar

$$\tau_c \equiv \frac{P}{2\dot{P}}, \tag{2.8}$$

where $P = 2\pi/\omega$ is the pulsar period. This equation usually overestimates the actual age of a system, indicating that the difference between the initial rotational velocity ω_0 and the final one ω is not so great (Migliazzo et al., 2002).

As previously mentioned, Crab-like PWNe tend to be observed only for pulsars younger than 20000 years, while older pulsars with high space velocities are usually observed as bow-shock nebulae (see 1.3.2).

From the previous formulas we can also estimate the equatorial magnetic field strength as

$$B_p \sin\alpha = \sqrt{\frac{3c^3 I P \dot{P}}{2\pi^2 r_\star^6}}. \tag{2.9}$$

With the period ranging from few milliseconds (for 'milliseconds pulsars') to few seconds (for 'magnetars'), this value ranges from 10^8 G to $\gtrsim 10^{15}$ G. In the case of the Crab nebula, which has a prominent PWN, the inferred magnetic field is of the order of 8×10^{12} G.

If n is constant, the spin-down luminosity of the pulsar evolves with time according to (Pacini and Salvati, 1973)

$$L = \dot{E}_0 \left(1 + \frac{t}{\tau_0}\right)^{-(n+1)/(n-1)}, \tag{2.10}$$

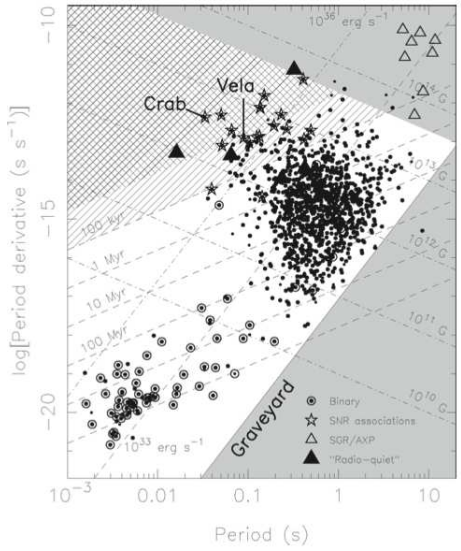

Figure 2.9: The $P - \dot{P}$ diagram for the known pulsar zoo. The figure is extracted from Becker (2009).

where $\dot{E}_0$ is the initial spin-down luminosity and $\tau_0 = P_0/[(n-1)\dot{P}_0]$ is the initial spin-down time scale. The energy input is thus roughly constant until $t \sim \tau_0$, and $L \propto t^{-(n+1)/(n-1)}$ for $t \gtrsim \tau_0$. The spin period evolves with a similar law,

$$P = P_0 \left(1 + \frac{t}{\tau_0}\right)^{1/(n-1)} , \tag{2.11}$$

ant thus $P \sim P_0$ for $t \ll \tau_0$ and $P \propto t^{1/(n-1)}$ otherwhise.

The pulsars primary observables are P and $\dot{P}$, and they give us insights into the spin evolution of neutron stars, which are summarized in Fig. 2.9, the so called '$P - \dot{P}$' diagram (Becker, 2009). It plays a role similar to the Hertzsprung-Russell diagram for ordinary stars, encoding a huge amount of information about the pulsar properties. In this diagram contrasts normal pulsars (with $P \sim 0.5$ s and $\dot{P} \sim 10^{-15}$ ss^{-1}) and millisecond pulsars (with $P \sim 3$ ms and $\dot{P} \sim 10^{-20}$ ss^{-1}), with the first populating the 'island' of points and the second populating the lower part of the plot. As infer from the previous formulas, differences in P and $\dot{P}$ imply different ages and values of the magnetic field for the two populations. Lines of constant $B \propto \sqrt{P\dot{P}}$ and $\tau \propto P/\dot{P}$ are drawn on the diagram. from which we can infer typical magnetic fields and ages of $\sim 10^{12}$ G and $\sim 10^7$ years for normal pulsars, and 10^8 G and 10^9 years for millisecond pulsars. As expected the rate of spin-down energy, also shown in the figure, is higher for the young and for the millisecond pulsars.

Another important difference between normal and millisecond pulsars is that these are 'accretion powered' rather than 'rotation powered'. Their high spinning velocities are in fact produced as a consequence of the presence of a companion star in a closed binary system.

In this systems the angular momentum is transferred from the companion to the neutron star, spinning it up to short periods and reducing its magnetic field. Such stars are usually referred to as 'recycled pulsars'. Companion stars are seen orbiting around a millisecond pulsar in the 80% of the cases, while only the 1% of the normal pulsars show a companion. These companion stars are either white dwarf, main sequence stars of neutron stars, with different orbital parameters for the different types.

2.2.2 Pulsar magnetospheres

The previous argument works only in the case of an isolated neutron star, i.e. for electromagnetic emission in a vacuum. Since the gravitational force acting on the surface of a neutron star have to be really high, it has been long supposed that pulsars must be surrounded by a very low density plasma. On the contrary Goldreich and Julian (1969) demonstrated that a neutron star rotating about its dipole axis has to be surrounded by a dense magnetosphere.

The rotation of the magnetized neutron star induces an enormous superficial electric field. The equilibrium at the star surface is thus

$$\vec{E} + \frac{\vec{\omega} \times \vec{r}}{c} \times \vec{B} = 0 \,. \tag{2.12}$$

The tangential component of the electric field must be conserved at the star surface crossing. Assuming that the star is effectively in a vacuum, the Lorentz invariant $\vec{E} \cdot \vec{B}$ inside and outside the star is

$$\vec{E} \cdot \vec{B} = \begin{cases} 0 & \text{for } r < r_\star \,, \\ -\dfrac{\omega r_\star B_p^2}{c} \left(\dfrac{r_\star}{r}\right)^7 \cos^3\theta & \text{for } r \geq r_\star \,, \end{cases} \tag{2.13}$$

where θ is the polar angle between the distance from the star, $\vec{r}$, and its rotational axis. Thus the electrons on the star surface experience the electromagnetic force

$$F_{em} = eE_\parallel = \frac{e\omega r_\star B_p}{c} \cos^3\theta \,, \tag{2.14}$$

with $E_\parallel$ the component parallel to the magnetic field. By comparing this expression with that for the gravitational force at the star surface, and by substituting the characteristic values for a neutron star, we can obtain

$$\frac{F_{em}}{F_g} = \frac{eE_\parallel}{GM_\star m_e^2 / r_\star^2} \propto 8 \cdot 10^{11} \frac{B_p}{10^{12}\,\mathrm{G}} \frac{1\,\mathrm{s}}{P} \cos^3\theta \,. \tag{2.15}$$

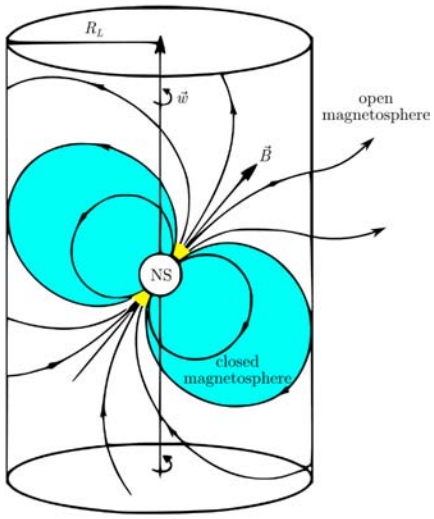

Figure 2.10: Magnetosphere of a pulsar. In light blue the closed magnetosphere, where le field lines are closed and magnetic field and plasma are in corotation with the star.

Thus, even if the neutron star was born in a vacuum, the electromagnetic forces at its surface would be so intense that suddenly its surroundings would be filled with electrons extracted from the star itself. Moreover this 'primary' particles initiate an electron-positron cascade, which populates the whole magnetosphere with a dense plasma.

Near to the pulsar the strength of the magnetic field is sufficient to ensure that the plasma corotates, as predicted by the Alfvèn theorem (Fig. 2.10). At some point near to the light cylinder, corotation must cease, field lines crossing the light cylinder are bent backward with respect to the direction of the rotation of the star, and the particles escape, carrying away magnetic flux and energy in the form of a magnetized and ultrarelativist wind. The light-cylinder simply represents the ideal surface at which the matter in corotation reaches the speed of light, $R_L \equiv c/\omega \sim 10^8$ cm.

By tracing the escaping (i.e. open) field lines back to the stellar surface, we can identify the regions from which particles are extracted, the 'polar caps' (Fig. 2.11).

In the polar cap regions primary particles (extracted from the star surface) emit photons via curvature radiation, which is a natural consequence of the interaction of charged particles with the strong magnetic field on the star surface. Particles in fields of $\sim (10^{10} \div 10^{11})$ G emit very rapidly the energy associated with their momentum component perpendicular to the magnetic field direction, and move along magnetic field lines, with very small gyration radii (Suvorov and Chugunov, 1973), in practice streaming on the field line. The properties of the curvature radiation are very similar to those of synchrotron radiation. Curvature radiation

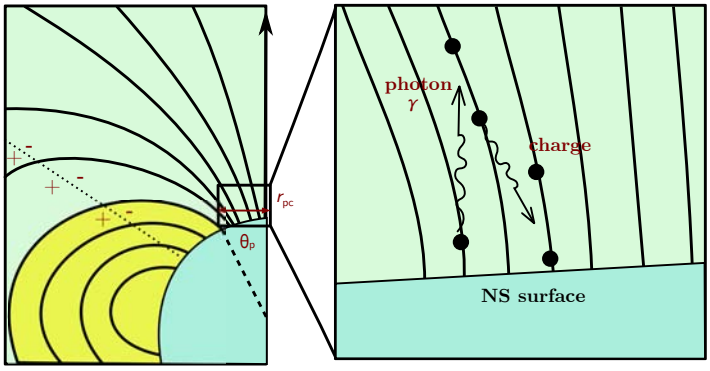

Figure 2.11: Close up of a polar cap, the region in which particle extraction from the star surface takes place. Outside of the polar cap, primary electrons/positrons interact with photons, giving rise to particle electromagnetic cascades, in which secondary particles are produced.

photons with energies greater than 50 MeV are then able to start electromagnetic cascades and the production of electron-positron couples via the reaction $\gamma + B \rightarrow e^- + e^+$ (Sturrock, 1970).

To maintain the stationarity of the plasma at the polar caps, plasma must be continuously generated on the open field lines in these polar regions. The plasma then flows along the field lines with relativistic velocity, eventually escaping from the light cylinder.

The number density of primary particles generated at the polar caps is expected to be well described by the Goldreich & Julian formula, which represents the density necessary to screen the induced electric field, namely

$$n_{GJ} \equiv \mid (\vec{\omega} \cdot \vec{B})/(2\pi ec) \mid \ . \tag{2.16}$$

In the case of an aligned rotator the cylindrical radius of the polar caps can be estimated as $r_{\rm pc} \simeq \sqrt{(r_\star^3/R_L)}$, but it is also a good approximation in the case of an oblique rotator. Assuming that particles leave a polar cap with relativistic velocity, the rate of particles ejected per unit time is

$$\dot{N} = \kappa \frac{\omega^2 B_{pc} r_\star^3}{ec} \simeq 2.7 \times 10^{30} \kappa \left(\frac{B_{pc}}{10^{12}\,\mathrm{G}}\right)\left(\frac{P}{1\,\mathrm{s}}\right)^{-2} \ \mathrm{s}^{-1} \ . \tag{2.17}$$

where B_{pc} is the magnetic field at the polar cap. This escaping rate is expressed in terms of the 'pair multiplicity' κ, which is defined as the number of pairs produced by a single primary particle that emerges from a polar cap. It is also connected to the energetic relevance of the ion component of the wind. Since ions are not produced in electromagnetic cascades, they can only be primary (i.e. extracted directly from the star, which happens when $\vec{\omega} \cdot \vec{B}_{pc} < 0$), thus they can be at most a fraction $\sim 1/\kappa$ of the total number of couples of the wind.

Up to now the value of this parameter is still uncertain. In the case of the Crab nebula, the first MHD models and high energy observations (Kennel and Coroniti, 1984b; Gaensler et al., 2002) suggested that $\kappa \sim 10^4$. In this case ions would be energetically dominant even if numerically lower in the wind. In this scenario, only particles responsible for the high energy emission are part of the pulsar outflow, while radio particles should be of different origin. On the contrary, if radio particles are considered as part of the pulsar wind, the expected pair multiplicity is much higher, $\kappa \sim 10^6$ (Bucciantini et al., 2011), and in that case the energy flux carried by ions in the wind would be completely irrelevant.

As we will see in the following, the value of κ has also important consequences in terms of constraining the acceleration process working at the wind termination shock (Sironi and Spitkovsky, 2011; Arons, 2012).

2.2.3 The wind of an aligned rotator

If pulsars were aligned magnetic dipoles rotating in a vacuum, they did not lose energy. But the argument of Goldreich & Julian has shown us that they are effectively not in a vacuum, but rather surrounded by a dense plasma.

Since the magnetic field is frozen into the plasma, as matter can not rotate with superluminal velocity, the magnetic field lines beyond the light cylinder are wrapped backwards with respect to the rotation of the star. As a result, even an aligned rotator loses its energy in the form of a wind. Since the magnetic field is parallel to the rotation axis of the star, the problem is axisymmetric. The rotation energy of the star is spent in the generation of a toroidal magnetic field component in the wind. Since the plasma conductivity is infinite, the electric field in the proper frame of the flow ($\vec{E}'$) vanishes, and thus

$$\vec{E} + \frac{\vec{v}}{c} \times \vec{B} = 0\,. \tag{2.18}$$

In a steady, axisymmetric solution, the displacement currents vanish and the toroidal magnetic field is generated by poloidal currents flowing into or out of the polar caps (depending on the sign of $\vec{\omega} \cdot \vec{B}_{pc}$). This current flows in a sheet along the boundary between the closed and the open magnetospheres up to the light cylinder, and extends as an equatorial current sheet further out. At the light cylinder the poloidal and toroidal components of the magnetic field are comparable. In the wind region the conservation of the magnetic flux in a diverging flow implies that the poloidal field ($\propto 1/r^2$, with r the cylindrical radius) decreases faster

than the toroidal one ($\propto r$). Taking this into account, the field in the far wind zone can be considered in good approximation as completely toroidal.

An important variable to describe the physical behavior of the wind is its magnetization, defined as the ratio of the magnetic to particle entalphy densities in the comoving frame

$$\sigma = \frac{B'^2}{4\pi\omega_h c^2}\,, \tag{2.19}$$

where ω_h is the plasma enthalpy density and $\vec{B}'$ the magnetic field in the comoving frame. Assuming that the plasma is cold (i.e. $P \ll \rho c^2$, with ρ the plasma mass density), the enthalpy is $\omega_h = nm_e c^2/\Gamma$, where n is the plasma number density in the observer frame and Γ the Lorentz factor of the wind. Since the velocity of the radial wind is perpendicular to $\vec{B}' = \vec{B}/\Gamma$, the magnetization is exactly the ratio between the energy carried by the Poynting flux and that carried by the particles (the ram pressure)

$$\sigma = \frac{B^2}{4\pi n m_e \Gamma^2 c^2}\,. \tag{2.20}$$

According to theories of pulsar's magnetospheres, the magnetization is expected to be very high near to the light cylinder, $\sigma \gg 1$, so that the wind is magnetically dominated.

Since the plasma is likely to emerge through the light cylinder with subsonic velocity, the inertia terms of the equation of motion are unimportant. Moreover, in the pulsar case, also the gravity and gas pressure are negligible and the dynamics simplifies significantly. This scenario is referred as the 'force-free' approximation, meaning that the Lorentz force is exactly cancelled by the electric one

$$\rho_e \vec{E} + \frac{\vec{j}}{c} \times \vec{B} = 0\,. \tag{2.21}$$

Integrating this equation in the Maxwell's equations, the dynamics is complete.

Under these assumptions the axisymmetric force-free MHD equations of the pulsar magnetosphere, in general strongly non linear, must be solved numerically (Contopoulos et al., 1999; Gruzinov, 2005).

The exact solution for the case of a magnetic monopole was solved many years before numerical solutions by Michel (1973), in the split monopole model. Here the magnetic field lines extend from the origin to infinity in the upper hemisphere and converge from infinity to the origin in the lower hemisphere. The two hemispheres are separated by a current sheet. The magnetic surfaces are coaxial cones, with vertices lying at the origin. The plasma flows radially from the origin to infinity. Of course in a realistic dipole magnetosphere the flow

lines can not be radial everywhere, at least they cannot be radial within the light cylinder, in the closed magnetosphere. But Michel (1974) showed that, independently of the field morphology near to the origin, the flow lines become asymptotically radial beyond the light cylinder in the force-free approximation. In fact the force-free condition (Eq. 2.2.3) states that the current flows along the magnetic surfaces, while the electric field is perpendicular to these surfaces, which are equipotentials. Taking all into account, we can easily find the asymptotic behavior of the basic physical quantities in the wind:

$$\begin{aligned} &B_\phi \propto R_L/r \qquad E \propto R_L/r \\ &B_r \propto R_L/r^2 \quad n \propto R_L^2/r^2 \ , \end{aligned} \tag{2.22}$$

with r the radius in spherical polar coordinates. Michel (1974) also showed that the differences between E and B decrease with the radius, and the flow accelerates with velocity approaching c. As the Lorentz factor of the flow increases, the plasma inertia becomes more important, as long as it is no longer negligible. It usually happens near to the fast magnetosonic point. Beyond this point the force-free approximation brakes down, and the full MHD equations must be solved (Kirk et al., 2009). However the flow remains approximately radial also in the full MHD regime, since the additional inertia forces tend to resist to collimation. If the flow is radial in the force-free region, it is also radial with good approximation further out.

The extension of the model to the full relativistic MHD regime was given by Komissarov (2006) and Bucciantini et al. (2006).

2.2.4 Striped winds from pulsars

Actually pulsars not only are immersed in a dense plasma rather than in a vacuum, but furthermore they are neither axisymmetric nor steady. They are in fact oblique rotators, with magnetic and rotational axes inclined by and angle ζ. As a result the wind structure is more complicated than in the aligned rotator case.

The global picture is shown in Fig. 2.12. As in the aligned rotator the current sheet is a single surface, separating magnetic field lines that are attached to opposite magnetic hemispheres on the star surface. But in the oblique case the emerging pattern is similar to that observed in the solar wind: the current sheet twists and tangles, cutting the equatorial plane along twin spirals, that separate stripes of magnetic field of opposite polarities. The oscillations take place within a region around the polar axis of angular extent equal to the inclination

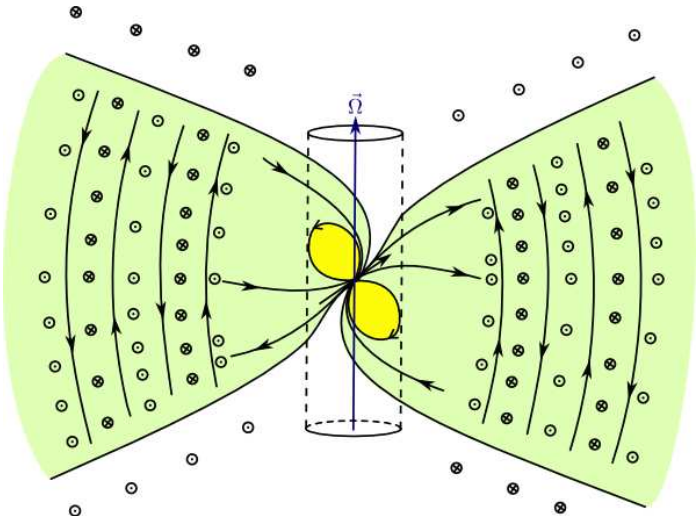

Figure 2.12: Scheme of the PW from the model by Coroniti (1990). Outside the light cylinder the 'striped' zone is clearly visible as alternating stripes of opposite field polarities.

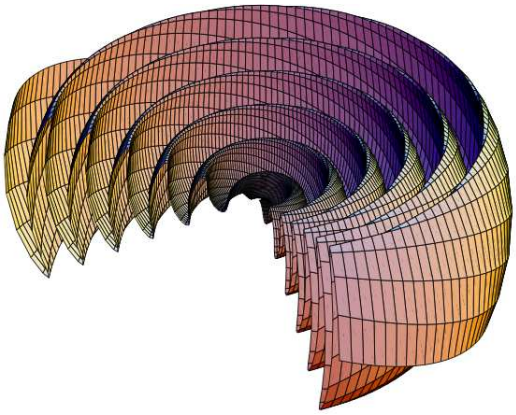

Figure 2.13: 3d picture of the striped PW. The oscillating current sheet gives rise to a structure similar to a ballerina skirt.

angle ζ. The appearance of this striped wind is similar to a ballerina skirt (Fig. 2.13). In the outer zone, far from the pulsar, the distance between successive corrugations is small compared with the radius of curvature of their surfaces, and the spiral in the equatorial plane becomes tightly wound. At high latitudes the magnetic field does not invert in polarity, and there is no current sheet embedded in the flow. Here magnetic oscillations can propagate outward, in the form of magnetosonic waves (Bogovalov and Tsinganos, 2001).

Neighboring stripes of opposite polarities offer the perfect location for magnetic dissipation to occur Coroniti (1990), and hence σ is likely to decrease with increasing distance from the pulsar in some range of latitudes around the equator.

Indeed, a long standing problem in PWN physics is the so called *σ-problem*. As we previously mentioned, close to the light cylinder the wind is expected to be magnetically dominated ($\sigma \gg 1$). However, effective deceleration of the flow at the TS is only possi-

ble if its magnetization is not too high. In particular, steady state 1D or 2D MHD models (Kennel and Coroniti, 1984a; Begelman and Li, 1992), pointed to $\sigma \sim v_N/c$ at the TS, with $v_N \approx 10^3 \mathrm{km}/s$ the expansion velocity of the nebula. This requirement has somewhat been revised and made less severe by later multi-D MHD simulations (Del Zanna et al., 2004; Porth et al., 2014), but considerable dissipation still appears to be required.

The split monopole wind structure and its use in multi-D MHD simulations provided a straightforward solution to another puzzle in PWN physics that we already mentioned, namely the jet-torus morphology of the high energy emission from these objects. The anisotropic distribution of the wind energy flux produces an oblate TS, more distant from the pulsar at the equator than along the polar axis, where cusps develop. Despite the polar jets appear to originate very close to the pulsar, they are actually generated at the TS polar cusps, in the post-shock flow. Here, as shown in many different simulations Komissarov (2004); Del Zanna et al. (2004, 2006), magnetic hoop stresses can lead to effective collimation. Even if $\sigma < 1$, compression of the toroidal magnetic field downstream of the TS can bring the field up to the equipartition value. When this happens, the magnetic tension diverts the flow towards the polar axis at intermediate latitudes, collimating the polar outflow into a jet. Of course this process only works if σ is sufficiently large: for the parameters appropriate to describe the crab Nebula, 2D simulations indicate $\sigma > 0.01$.

State of the art 3D simulations seem to indicate that in the Crab Nebula the wind magnetization might be $\sigma \sim$ a few, with considerable dissipation taking place downstream of the shock. These findings are however preliminary. 3D simulations only extend to few hundred years after the explosion and extrapolations of their results to the actual age of the nebula seem to indicate that the final strength of the nebular magnetic field might be too low and incompatible with the emission spectrum, suggesting that even higher values of the wind σ might be required. The pulsar wind magnetization must be likely much larger than 0.001 for most of the flow in order to explain the presence of a jet with the observed properties . As we will discuss later, this lower limit on σ is problematic from the point of view of understanding particle acceleration at the termination shock.

2.2.5 The PW Termination Shock

As the freely expanding relativistic outflow produced by the pulsar encounters the slowly expanding nebula, a termination shock forms. The TS is an inverse MHD shock, which

is generated for matching the boundary conditions imposed by the ambient material at the nebula radius. At a distance $R_{\rm TS}$ from the pulsar, the ram pressure of the wind and the PWN internal pressure must be balanced

$$R_{\rm TS} = \sqrt{\dot{E}/(4\pi\omega c P_{\rm PWN})}, \tag{2.23}$$

where ω is the equivalent filling factor for an isotropic wind, while $P_{\rm PWN}$ is the total pressure in the nebula. Upstream of the TS the wind is cold and particles do not radiate, but they flow with relativistic speeds along the magnetic field lines. At the shock front, particles are thermalized and re-accelerated, producing synchrotron emission in the downstream.

Assuming equipartition between particles and magnetic field it is possible to estimate the pressure, by integrating the spectrum of the PWN and by applying the standard formula for synchrotron emission. With the typical values obtained for $P_{\rm PWN}$ and $\dot{E}$, the termination shock radius results of the order of 0.1 pc. For the Crab Nebula the equipartition field is estimated to be BPWN $\simeq 300\mu$G (Trimble, 1982), and the pressure should reach equipartition at a distance of $\sim (5 \div 10)R_{\rm TS}$ (Kennel and Coroniti, 1984b). The typical value for spin-down luminosity is $\dot{E} = 5 \times 10^{38}$ erg s^{-1}, and leads to $R_{\rm TS} \simeq 4 \times 10^{17}$ cm, which is consistent with the observed location of the optical wisps and the dimensions of the inner X-ray ring.

With the same procedure, as expected, a weaker equipartition field of $B_{\rm PWN} \sim 80\mu$G is obtained in the case of 3C 58 (Green and Scheuer, 1992). With the weaker value for the spin-down luminosity it leads to a position of the TS similar to the Crab one $R_{\rm TS} \simeq 6 \times 10^{17}$ cm.

2.2.6 1D models

The most famous 1d model of the Crab nebula was proposed by Kennel and Coroniti (1984a) and Kennel and Coroniti (1984b) (K&C hereafter), as a re-elaboration of the hydrodynamical model by Rees and Gunn (1974). They solved the full set of relativistic MHD equations assuming the problem as stationary and having a spherical symmetry. Despite that strong assumptions, this was the first model able to successfully predict the values of the wind magnetization σ and Lorentz factor Γ and to reproduce the entire synchrotron spectrum of the nebula.

K&C divide the Crab nebula into six spherical concentric regions, shown in Fig. 2.14, and consider a constant expansion velocity without interaction with the thermal filaments. Since

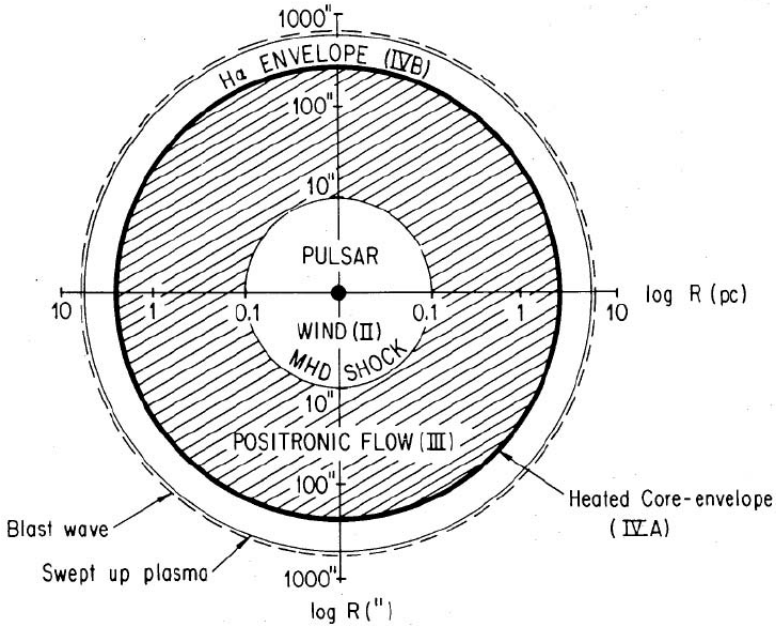

Figure 2.14: The schematic representation of the Crab nebula PWN, as presented in Kennel and Coroniti (1984a).

the wind velocity must be decreased to match the slow expansion of the nebula boundaries, they argue that the wind must be terminated by a strong shock, the TS. The properties of this shock are found matching the pressure and four-velocity of the wind with those of the supernova remnant, which is expanding with $v \simeq 2000$ km s^{-1}. In the inner zone (region (II) of Fig. 2.14), the highly relativistic, magnetized and cold wind expands from the pulsar light cylinder towards the TS, located at ~ 0.1 pc from the pulsar. At the shock the kinetic energy of the wind is partially converted into internal energy of the fluid, partially in magnetic energy and partially used to accelerate particles. Now in the downstream region, wind particles are thermalized and emit via synchrotron radiation in the ambient magnetic field (region (III)). The flow velocity in region (III) is $\sim c/3$ at the inner boundary, and matches the nebula expansion velocity at the outer boundary. The nebula extends from the TS up to ~ 2 pc, and it is made up of a radial flux of positrons and electrons and a toroidal magnetic field, perpendicular to the rotational axis of the pulsar. Region (IV) consist of the expanding supernova ejecta. Finally, region (V) and (VI) consist of the shocked and un-shocked ISM, in which the forward shock of the PWN is expanding.

In the K&C model the key parameter is the wind magnetization, as defined in Eq. 2.20. Authors argue that shocks with opposite limits of the magnetization would lead to very different physical behaviors.

Highly magnetized shock ($\sigma \gg 1$) are relatively week and the magnetic field in the downstream remains large. That means that particles in the downstream are not sufficiently randomized in their pitch angles, giving very poor synchrotron emission, that would also be characterized by very short synchrotron life-times, due to the high magnetic field. Moreover, from the balance of the wind ram pressure and magnetic flux upstream and downstream of the shock, it is difficult to match the observed (estimated from the inner ring) position of the TS and the one inferred by the model.

On the contrary, low magnetized models ($\sigma \lesssim 1$) predict very strong shocks. Here the conversion of the wind energy in thermal energy and particle acceleration is very efficient and leads to sufficiently low magnetic field in the nebula to allow the particles to generate the observed synchrotron luminosity.

K&C found that the Crab emission is best reproduced by the magnetization $\sigma = 0.003$. For this value the TS position in estimated to be at $r \simeq 3 \times 10^{17}$ cm, or 0.1 pc, in perfect agreement with *Chandra* observations of the inner ring. The computed synchrotron emission also matches observations, considering an efficiency in converting the pulsar spin-down energy of $\sim 20\%$.

In de Jager et al. (1996) the IC emission is computed on the basis of the K&C findings. They found that an average magnetic field of $B \sim 300\,\mu$G must be considered in the nebula to account for the observed IC emission.

The stronger problem raised by these 1D models is the already discussed $\sigma-$problem. Since they require a very low magnetization in the nebula to account for the observed synchrotron emission, while pulsar theories predict very strong magnetization at the light cylinder, there must be a point at which the magnetization lowers from $\sim 10^4$ to $\ll 1$.

2.2.7 2D models

The first to develop a 2D model of the Crab nebula were Begelman and Li (1992), taking into account that the toroidal magnetic field should produce stresses in the nebula, leading to a prolate shape.

The interest in multi-D models of PWNe rose after *Chandra* arrival, when became clear that simple 1D models cannot account for the complex and variable inner structure of the Crab nebula, which is neither spherically symmetric nor stationary.

As we already discussed in Sec. 2.1 the complex axisymmetric X-ray morphology first

observed in the Crab nebula, the so called jet-torus morphology, was then observed in many other PWNe, and there is a general agreement that it should be a fundamental characteristic of young systems. Theoretical models of the PW show that at the typical distance of the TS, the wind luminosity and magnetization are not uniform, but they can be described by the split-monopole solution (see Sec.2.2.4 and references therein). Here the most of the energy is concentrated at equatorial latitudes and the shock assumes a prolate shape, with polar cusps. Lyubarsky (2002) then suggested that jets could be collimated in the body of the nebula by magnetic hoop-stresses, and launched at the TS polar cusps. This was then largely confirmed by numerical 2D models (Del Zanna et al., 2004; Komissarov, 2004; Bogovalov et al., 2005; Volpi et al., 2008).

Moreover 2D numerical simulations were able to reproduce many details of the Crab nebula, down to very small scales. High energy emission was reproduced with great details by Del Zanna et al. (2006), as long as polarization (Bucciantini et al., 2005b) and the whole spectrum (Volpi et al., 2008). 2D models have reached a sufficient accuracy to reproduce also the time variability at different wavelengths, showing that wisps can be reproduced in terms of timescales, morphological patterns and velocities (Camus et al., 2009; Olmi et al., 2014).

2D models agree with the fact that the magnetization required to explain the observed morphology of the Crab nebula is about 1 order of magnitude greater than that predicted by 1D models, since the new degree of freedom allows to accomodate more magnetized winds.

2.2.8 3D models

From Begelman (1998) it is largely known that purely toroidal magnetic field configurations are strongly subjected to current driven instabilities (kink-like instabilities), that are also observed in PWNe (Mori et al., 2004b; Pavlov et al., 2003). To account for this kind of instabilities a full 3D modelization is needed, since in 2D kink modes are artificially suppressed.

A preliminary study of a 3D numerical model of the Crab nebula was recently presented by Porth et al. (2014). Unfortunately the computational cost of this heavy numerical model only allow the authors to reproduce 70 years of the Crab evolution, which are not sufficient to obtain definitive informations on the emission properties. Nevertheless it is sufficient to confirm qualitative expectations that the inner region close to the TS is still dominated by a

toroidal field, preserving the axisymmetric structure of 2D simulations. Moreover 3D models can accomodate wind with σ of the order of unity, apparently solving the $\sigma-$problem that seems only an artifact of low dimensions models.

2.3 Evolution of a system PWN/SNR

The evolution of the PWN in its parent SNR govern its observational properties (see Gaensler and Slane (2006) and references therein).

2.3.1 Expansion into the un-shocked ejecta

When the PWN is born, it is surrounded by the expanding debris of the parent supernova explosion, the ejecta. At early times the pulsar is almost located in the center of the remnant, which expands with the typical velocity of the freely expanding SN blast wave ($v \gtrsim (5 \div 10) \times 10^3$ km s^{-1}). Since the pulsar wind is over-pressured with respect to its environment, the PWN expands rapidly in the ejecta, moving supersonically and driving a shock into the remnant. The PWN evolution in the spherically symmetric case is (Chevalier, 1977)

$$R_{\rm PWN} \simeq 1.1 \text{ pc} \times \left(\frac{\dot{E}_0}{10^{38} \text{ erg s}^{-1}}\right)^{1/5} \times \left(\frac{E_{SN}}{10^{51} \text{ erg}}\right)^{3/10} \times \left(\frac{M_{\rm ej}}{10 M_\odot}\right)^{-1/2} \times \left(\frac{t}{10^3 \text{ yr}}\right)^{6/5}, \tag{2.24}$$

with $\dot{E}_0$ the initial spin-down luminosity of the pulsar, $R_{\rm PWN}$ the PWN radius at the time t, $E_{\rm SN}$ the kinetic energy of the ejecta and $M_{\rm ej}$ their mass. Since the PWN forward shock, identified by $R_{\rm PWN}$, is accelerating as $t \propto t^{6/5}$, while the sound speed in the nebula is $\sim c/3$, the PWN remains centered on the pulsar during its evolution. The dynamics in the nebula is particle dominated and the equipartition magnetic field is reached at large radii. Thus we expect to observe rapidly expanding SNR, with reasonably symmetric PWN at their center, with a young pulsar inside the PWN itself.

The most famous example of PWN in this evolutionary phase is the Crab Nebula, or also the PWN G21.5-09 (Fig. 2.15), estimated to be $\sim$ 1000 yr old.

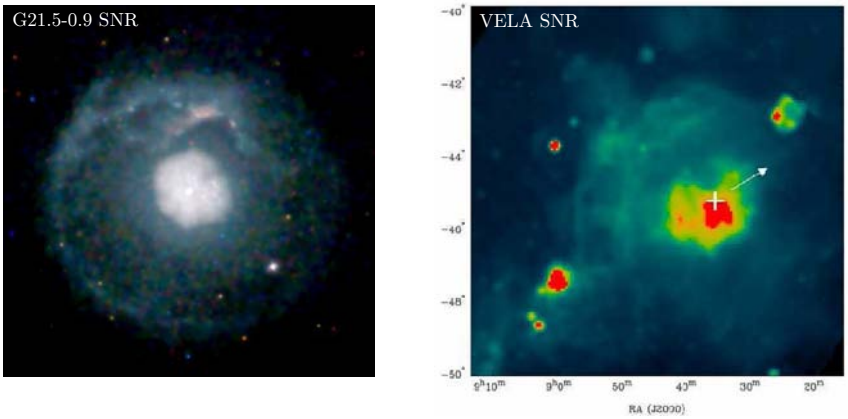

Figure 2.15: *Left panel*: the G21.5-0.9 SNR in a composite Chandra image. The central position of the pulsar together with the symmetric appearance of the PWN probably indicate the fact that the remnant is only modestly evolved. *Right panel*: the Vela SNR in a 2.4 GHz map (Parkes). The cross indicates the position of the pulsar and the arrow its direction of motion (Dodson et al., 2003). The fact that the pulsar is not located in the center of the remnant, and that it is not moving away from it, indicates that the system had already passed through the reverberation phase.

2.3.2 The reverberation phase: interaction with the SNR reverse shock

When the expanding remnant has swept up a significant fraction of the mass of the surrounding ISM, it begins to evolve in the Sedov-Taylor phase., in which the total energy is conserved and it is equally distributed between kinetic and thermal contributions (as discussed in Chap. 1). Now the interface between the SNR and its ambient medium is more complex: a forward shock compresses and heats the surrounding gas, a reverse shock decelerates the ejecta. This two shocks are separated by a contact discontinuity (CD), where instabilities can grow. After an initial phase during which the reverse shock expands outward behind the forward shock, it starts to move inward. Without considering the central PWN, and assuming that the SNR is expanding in a constant density medium, the reverse shock is supposed to reach the center of the SNR in a time (Reynolds and Chevalier, 1984)

$$t_{\rm Sedov} \simeq 7 \left(\frac{M_{\rm ej}}{10\,M_\odot}\right)^{5/6} \left(\frac{E_{SN}}{10^{51}\,{\rm erg}}\right)^{-1/2} \left(\frac{n_0}{1\,{\rm cm}^{-3}}\right)^{-1/3} \times 10^3\,{\rm yr}\,, \tag{2.25}$$

where n_0 is the number density of the ambient gas.

When $t \gtrsim t_{\rm Sedov}$ the SNR interior is totally filled with the shocked ejecta, the SNR reaches a self-similar state which can be fully described with simple analytical model (see Cox (1972)). During this phase the forward shock radius evolves as $R_{\rm PWN} \propto t^{2/5}$.

Obviously when a PWN is present in the center of the SNR the evolution is different and complex even in the simplest case of a stationary pulsar, an isotropic wind and a spherical SNR. The inward moving reverse shock collides with the outward moving forward shock of

the PWN on a time scale of the order of few thousand years ($\lesssim t_{\rm Sedov}$) (van der Swaluw et al., 2001). The reverse shock compresses the PWN by a large factor, and it responds with an increase in pressure and a sudden expansion. The system 'reverberates' several times, resulting in oscillations of the nebula during a period of few thousand years. The nebular magnetic field increases and burns off the highest energy electrons (Reynolds and Chevalier, 1984; van der Swaluw et al., 2001; Bucciantini et al., 2003). This phase is usually associated with the appearance of strong Rayleigh-Taylor instabilities, which produce chaotic and filamentary structures, mixing thermal and non-thermal material within the PWN (Chevalier, 1998; Blondin et al., 2001).

In the reality the situation is even more complicated by the system characteristic velocities and asymmetries. The reverse shock then expands asymmetrically, moving faster in certain directions rather than in others. This results in a complicated 3d interaction, during and after which the PWN can reach highly distorted morphologies and can be significantly displaced from the remnant center, as in the case of Vela (Fig. 2.15).

2.3.3 Evolution of the PWN inside a Sedov SNR

Once the reverberation phase end, the PWN steadily expands with subsonic speed into the hot and shocked ejecta. In the case of a spherically symmetric expansion the evolution of $R_{\rm PWN}$ is expected to be $R_{\rm PWN} \propto t^{11/15}$ or $R_{\rm PWN} \propto t^{3/10}$, depending on the evolutionary stage with respect to the initial spin-down properties of the pulsar (van der Swaluw et al., 2001; Reynolds and Chevalier, 1984). The distance traveled by the pulsar from its birthing place can be greater enough to exceed the PWN outer radius. The pulsar thus escapes from its own wind bubble, leaving behind a sort of relic PWN and generating a new nebula around its current position (van der Swaluw et al., 2004). Observationally this is seen as a central, possibly distorted, radio PWN, with possibly only a much smaller X-ray emission, and the pulsar located at one edge, or even ouside, of the old PWN. The pulsar is usually connected with a sort of bridge of radio and X-ray emission to the parent PWN. One example of such a system is the PWN in SNR G327.1-1.1 (right panel of Fig. 2.16).

The sound speed in the ejecta decreases, and since the pulsar motion can possibly become supersonic, it can drive a bow-shock nebula (Chevalier, 1998; Van Der Swaluw et al., 1998), which appears as a comet at X-ray and radio observations (one example is the PSR B1853+01 in the SNR W44 shown in Fig. 2.16, left panel).

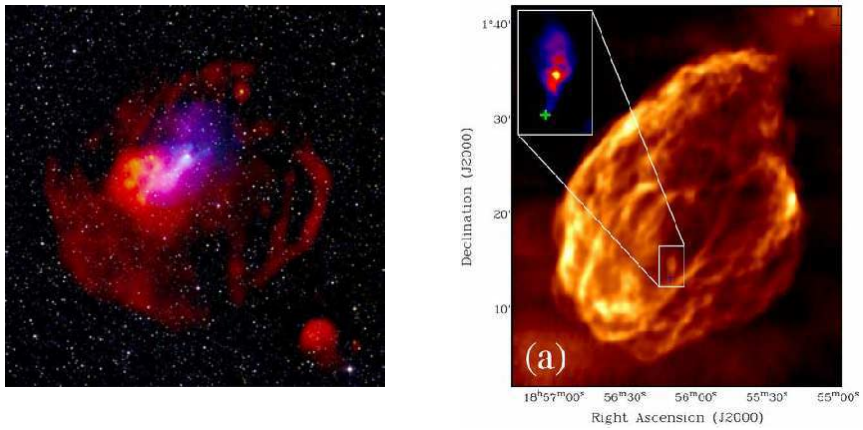

Figure 2.16: *Left panel*: A combined radio (red/yellow), X-ray (blue), infrared (white) image of the supernova remnant G327.1-1.1 (credits NASA/Chandra). The offset between the X-ray and radio emissions indicates that the radio nebula is a relic PWN. The pulsar is probably still moving subsonically inside the SNR, generating a new PWN. *Right panel*: The SNR W44 and the nebula surrounding the pulsar B1853+01 in the inset (marked by the cross), in a VLA image (Giacani et al., 1997; Frail et al., 1996).The pulsar is near to the PWN edge, and it is now driving a small bow-shock nebula as a result of its supersonic motion.

The time scale for a pulsar to cross its SNR outer shell is of about 40 000 years. Eventually the injection of energy from the star crossing the shell may re-energize and brighten the SNR (Shull et al., 1989; van der Swaluw et al., 2002).

2.3.4 Evolution of a pulsar in the ISM

When finally the pulsar is escaped from its parent SNR, its motion is often highly supersonic in the ISM and it gives rise to a complete bow-shock nebula. As discussed in Chap. 1, if the ambient medium is a neutral gas, the forward shock is visible as H_α emission produced by shock excitation and charge exchange. The shocked wind also emits in the form of synchrotron emission, visible at both radio and X-ray wavelengths, and with a cometary morphology, with a bright head and a tail.

Since the pulsar is now moving in the Galaxy, its luminosity drops down, and its motion carries it far from the Galactic plane, where the density is higher. Some pulsars can eventually end up as low spin-down stars in low density regions, where their motion cannot be longer supersonic and their emission is too low to allow an observer to identify them as synchrotron nebulae. During the final stages the pulsar is surrounded by a slowly expanding cavity of relativistic material with dimensions $\gg$ 1 pc and confined by the thermal pressure of the ISM (Blandford et al., 1973; Arons, 1983). Few examples of pulsars in this final stage of their evolution are the 'Guitar Nebula' (B2224+65 Cordes et al. (1993)), the 'Mouse Neb-

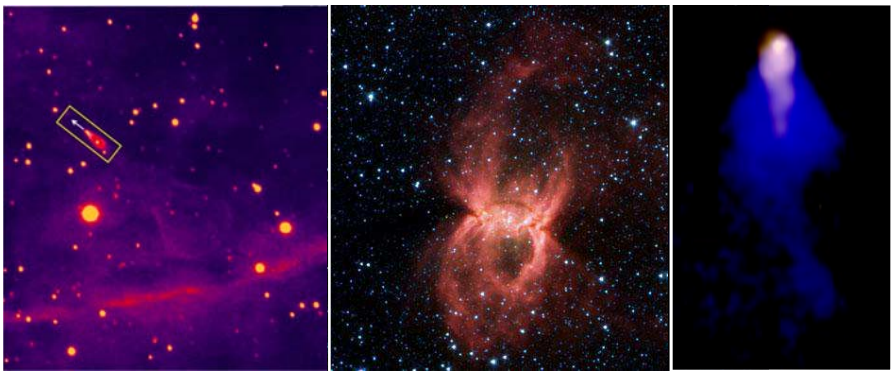

Figure 2.17: *Left panel*: the Guitar Nebula in an optical image from the Palomar Observatory. *Middle panel*: the Black Widow in a Spitzer image. *Right panel*: the Mouse nebula in a composite radio (blue) and X-ray (gold) close up image from NRAO and Chandra.

ula' (G359.23-0.82 Gaensler et al. (2004)) and the 'Black Widow Nebula' (see Fig. 2.17).

Chapter 3

The numerical model

Many of the open questions in PWN and pulsar physics appear to be strongly connected with the physical properties of the pulsar wind. Since the wind is cold at its basis (i.e. the particle kinetic energy is much larger than the thermal energy), no radiation is observed to come from the upstream region, that appears to the observer as an under luminous area surrounding the pulsar. As a consequence we do not have the possibility to inspect it directly.

What we can do is to use the PWN emission as a diagnostics of the PW properties. To this aim a powerful tool is provided by relativistic MHD simulations coupled with non-thermal radiation modelling. One can simulate the nebular dynamics arising from different assumptions on the wind and then compute synthetic emission maps to compare with observations. Thanks to the quantity and quality of the available data, the Crab Nebula is in this sense the perfect object to compare with. Our simulations are thus optimized for reproducing the Crab nebula.

Since relativistic MHD (RMHD) equations, in the multi-D case, have no analytical solutions, the numerical approach is mandatory. The numerical tool we use is the shock-capturing code for relativistic magnetohydrodynamic *ECHO*, developed by Del Zanna and Bucciantini (2002) and Del Zanna et al. (2003). The code solves the RMHD ideal equations in conservative form plus equations for particles tracers (see Sec. 3.3). Effects of synchrotron radiative losses on the fluid total energy evolution are not taken into account, since the radiated power is of the order of $\sim 20\%$ of the instantaneous pulsar input. The set of RMHD equations, that are at the basis of our model, is an hyperbolic system of partial differential equations and will be presented in Sec. 3.1.

To assure the axisimmetry of the model, the magnetic field is enforced to be in the az-

imuthal direction alone, thus always perpendicular to the velocity vector. In this case the condition $\nabla \cdot \vec{B} = 0$ is automatically ensured by the chosen geometry and thus $\vec{B}$ may be evolved as an ordinary fluid variable. Note that under these settings only five of the eight RMHD variables need to be evolved in time, namely: the fluid mass density ρ, the fluid poloidal velocity (v_r, v_θ), the pressure p, and the toroidal component of the magnetic field B_ϕ.

Physical quantities are defined at cell centered, which never coincides with the axis of symmetry $\theta = 0$ and $\theta = \pi$, where singularities may occur.

The scheme is particularly simple since complex Reimann solvers are avoided in favor of central-type component-wise techniques: the solver is defined by the two fastest local magneto sonic speeds and spatial reconstruction at cell boundaries is achieved by using ENO-type interpolating polynomials. Since the required time-steps are very small, and due to the high Lorentz factor the problem needs, third order reconstruction is avoided and a simpler second order limited reconstruction is employed. Time integration is achieved using a two-stage Runge-Kutta TVD algorithm, with a CFL of 0.5.

The physical domain is defined in spherical coordinates (r, θ, ϕ) with radius ranging from $r_{\min} = 0.05$ ly to $r_{\max} = 10$ ly, with logarithmic stretching ($dr \propto r$) imposed to better resolve the innermost region. The angular domain ranges from 0 to π, with reflection conditions at the polar axis.

Depending on the problem one is approaching, the grid resolution can be varied, in order to obtain a faster evolution or greater detail on the smallest structures. Typical resolutions are for example 512 cells in the radial direction and 256 in the polar direction, with a computational cost of about 1 week on the 64 CPUs cluster at the Arcetri INAF observatory (Florence).

3.1 The ideal RMHD equations

MHD couples Maxwell's equations with hydrodynamics to describe the macroscopic behavior in highly conducing plasmas. It is a long-wavelength approximation, actually meaning that

1. typical length scales L must be greater than the Debye length λ_D [1] and the electron/ion gyroradii;

2. the shortest time scales of interest must be long compared with the inverse of the plasma frequency [2] and the electron/ion cyclotron frequencies.

The first requirement also allows to assume quasi-neutrality of the plasma, since the plasma density is high enough.

RMHD is the relativistic extension of non-relativistic MHD equations, and it consist in a set of hyperbolic and differential equations: four equations of conservation (of mass, momentum, energy and magnetic flux) plus the Ohm equation.

MHD and RMHD are one-fluid approximations, traditionally used to describe macroscopic force balance and the dynamics of many astrophysical plasmas, since the previous approximations are reasonably good. In many cases MHD equations can be even simplified by the *ideal* approximation, that can be applied when resistivity and viscosity due to collisions are so small to be neglected. This is the case of PWN plasmas.

In the ideal approximation the electric and magnetic fields are easily connected by the ideal Ohm equation:

$$\vec{E} = -\frac{1}{c}\left(\vec{v} \wedge \vec{B}\right), \tag{3.3}$$

which means that the energy in the fluid comoving frame vanishes, and thus the fluid has infinite conductivity.

The relativistic continuity equation for mass density ρ in the observer reference frame is

$$\frac{\partial}{\partial t}(\rho\gamma) + \vec{\nabla} \cdot (\rho\gamma\vec{v}) = 0\,, \tag{3.4}$$

[1] The Debye length for plasmas is defined as

$$\lambda_D = \sqrt{\frac{kT_e}{4\pi n_e}e^2} = 7.43 \times 10^2 \sqrt{T_e/n_e}\ \mathrm{cm}\,, \tag{3.1}$$

where T_e and n_e are the electron temperature and number density respectively, while k is the Boltzmann constant.

[2] The plasma frequency is defined, for electrons and ions respectively, as follows

$$\omega_{\mathrm{pe}} = \sqrt{\frac{4\pi n_{\mathrm{e}} e^2}{m_e}}\,, \quad \omega_{\mathrm{pi}} = \sqrt{\frac{4\pi n_{\mathrm{i}} (Ze)^2}{m_i}}\,. \tag{3.2}$$

with γ the bulk Lorentz factor of the wind and $\vec{v}$ the fluid velocity. The equation for momentum conservation is

$$\frac{\partial}{\partial t}\left(\frac{w}{c^2}\gamma^2\vec{v}+\frac{1}{c}(\vec{E}\wedge\vec{B})\right)+\vec{\nabla}\cdot[\frac{w}{c^2}\vec{v}\vec{v}-\vec{E}\,\vec{E}-\vec{B}\,\vec{B}+ \\ +\left(p+\frac{E^2+B^2}{2}\right)\overleftrightarrow{I}]=0\,, \tag{3.5}$$

where $w=\rho c^2+\Gamma p/(\Gamma-1)$ is the relativistic enthalpy density for an ideal gas EoS, with p the thermal pressure and Γ the adiabatic index (whose value is 4/3 in the relativistic case), and $I_{ij}=\delta_{ij}$ is the identity tensor. The conservation of the energy density is finally

$$\frac{\partial}{\partial t}\left[w\gamma^2-p+\frac{E^2+B^2}{2}\right]+\vec{\nabla}\cdot\left[w\gamma^2\vec{v}+c(\vec{E}\wedge\vec{B})\right]=0\,. \tag{3.6}$$

In order to close the system of equations, the last expression to be considered is the Faraday's induction formula, connecting the time variation of the magnetic field with the space variation of the electric field

$$\frac{1}{c}\frac{\partial\vec{B}}{\partial t}+\vec{\nabla}\wedge\vec{E}=0\,. \tag{3.7}$$

3.2 Initializing the simulation

As initial conditions the simulation box is divided into four different regions. From outside in: the standard ISM, the supernova remnant (SNR), a primordial PWN which suddenly merge with the evolving PWN for $t>0$ yr and finally the ultra-relativistic, magnetized and cold PW.

Stationary injection of all the quantities is imposed at $r_{\rm min}$, where the super-Alfvènic wind is blowing from, while zeroth order extrapolation is assumed at the box outer boundary.

The initial values of the physical quantities are chosen such to better provide an overall evolution compatible with that of the Crab nebula.

3.2.1 The ISM

The outer zone of the simulation is the standard interstellar medium. We treat it as a static ($\vec{v}=0$), not magnetized ($\vec{B}=0$) and fully ionized medium, with a number density of 1 particle for cm^3 and a temperature of $T=10^4$ K.

3.2.2 The supernova ejecta

During the supernova explosion an enormous amount of energy is released (about 10^{53} erg). About 99% of this energy is supposed to be carried away by neutrinos produced in the first phases of the neutron star birth. The remaining 1% gives rise to a shock wave which sweeps up the outer layers of the progenitor star (the ejecta). Ejecta become thus a dense, cold ($P \ll \rho_e c^2$), unmagnetized and not relativistic shell in spherical expansion through the ISM. Their are treated following the hydrodynamical model by van der Swaluw et al. (2001), with $P_{ej} = 0$ and $\vec{B}_{ej} = 0$. Consistently with the spherical expansion, their radial velocity is linearly increasing

$$v_r = v_{ej} \frac{r}{r_{ej}}, \tag{3.8}$$

where r_{ej} is the initial outer radius of the ejecta shell (that we fixed at $r_{ej} = 1.5$ ly). The velocity v_{ej} is evaluated under the assumption that 1% of the total energy released in the supernova explosion is totally converted into kinetic energy

$$E_{ej} = \int_0^{r_{ej}} \frac{4\pi r^2}{2} \rho_{ej} v^2 dr, \tag{3.9}$$

with $E_{ej} \sim 10^{51}$ erg. The value of the density ρ_{ej} is obtained from the equation

$$M_{ej} = \int_0^{r_{ej}} 4\pi r^2 \rho_{ej} dr, \tag{3.10}$$

with $M_{ej} = 6 M_\odot$ is the total mass of the ejected material.

In the case of the Crab nebula, the energy released by the PWN from the birth of the pulsar is estimated to be $\sim 10^{49} \div 10^{50}$ erg. As a consequence the PWN should not affect at all the ejecta dynamics, which can be treated separately (Bucciantini et al., 2003).

3.2.3 The primordial PWN bubble

In order to optimize the numerical stability, we define a sort of 'primordial' PWN for the purpose to avoiding numerical diffusion at the contact discontinuity between the PW and the ejecta. This hot bubble is modeled following Kennel and Coroniti (1984b), in the case of low magnetization, and it will suddenly merge with the real PWN during the first stages of the evolution.

The density is thus expressed as

$$\rho = 3\rho_0 \left(\frac{r_0}{r_w} \right)^2 \gamma_0, \tag{3.11}$$

with r_w the initial radius of the PW region and γ_0 the initial wind Lorentz factor. Hereafter all the quantities labeled with the 0 index will be referred to the reference radius $r_0 \equiv 1$ ly. The magnetic field is modeled as

$$B_\phi = 3B_0 \left(\frac{r_0}{r_w}\right)^2 , \tag{3.12}$$

and the pressure

$$P = \frac{2}{3}\rho_0 \left(\frac{r_0}{r_w}\right)^2 \gamma_0^2 . \tag{3.13}$$

Finally the expansion velocity is imposed to be 0, to avoid numerical diffusion problems with the particle tracers that will be introduced in the following.

3.2.4 The Pulsar Wind

The cold, magnetized pulsar wind expands with a relativistic Lorentz factor $\gamma_0 = 100$ and it is continuously injected from the inner boundary at r_{min}. The used value of γ_0 is much lower than what expected to be appropriate for the Crab pulsar wind (e.g. Kennel and Coroniti, 1984a), but still high enough to guarantee that the flow is highly relativistic, in which case the post-shock dynamics is independent on the exact value of the Lorentz factor.

The structure of the pulsar wind is crucial in determining the shape of the PWN. We assume an energy flux that roughly depends on space as predicted by split monopole models of the pulsar magnetosphere (Michel, 1973), namely $F(r,\theta) = c(nm_e c^2\gamma_0^2 + B^2/4\pi) \propto r^{-2}\sin^2\theta$, where $B \equiv B_\phi$ is the embedded toroidal magnetic field and n is the number density of the outflow, but we remark that recent 3D models seem to indicate a different behavior for oblique rotators ($\sim \sin^4\theta$) (Spitkovsky, 2006; Tchekhovskoy et al., 2013).

The precise spatial dependence of the energy flux is taken as

$$F(r,\theta) = \frac{L_0}{4\pi r^2}\mathcal{F}(\theta) . \tag{3.14}$$

Its angular dependence is expressed by the function $\mathcal{F}$ as

$$\mathcal{F}(\theta) = \frac{\alpha + (1-\alpha)\sin^2\theta}{1-(1-\alpha)/3} , \tag{3.15}$$

where $L_0 = 5 \times 10^{38}$ erg s^{-1} is the pulsar spin-down luminosity, which we take as constant in time, and α is the *anisotropy parameter*, which controls the ratio between polar and equatorial energy flux. This must be such that $F(r,\pi/2) \gg F(r,0)$, and thus $\alpha \ll 1$.

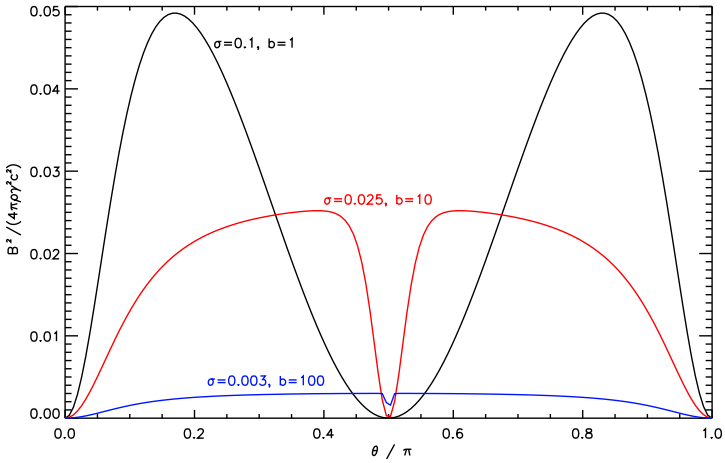

Figure 3.1: Plot of the wind magnetization as a function of the polar angle θ, for different choices of the two parameters σ_0 and b. The blue curve represents the limit case of the Kennel & Coroniti model ($\sigma = 0.003$, $b \to \infty$).

The magnetic field is assumed as

$$B(r,\theta) = \sqrt{\frac{\sigma_0 L_0}{c}} \frac{\mathcal{G}(\theta)}{r}\,, \tag{3.16}$$

where σ_0, which defines the magnitude of B, is the initial magnetization in the equatorial plane. The function $\mathcal{G}(\theta)$ is chosen having in mind the split-monopole dependence on latitude, but also the fact that the wind is expected to be striped (Coroniti, 1990) and dissipation is likely to take place between the stripes within a belt around the pulsar rotational equator

$$\mathcal{G}(\theta) = \sin\theta \tanh\left[b\left(\frac{\pi}{2} - \theta\right)\right]\,. \tag{3.17}$$

The parameter b relates to the width of this belt: for large values of b the pure split-monopole is recovered, while for $b \sim 1$ dissipation modulates the field strength at all latitudes (Del Zanna et al., 2004).

The wind magnetization is defined as

$$\sigma = B^2/(4\pi n m_e \gamma_0^2 c^2) = \sigma_0\, \mathcal{G}^2/(\mathcal{F} - \sigma_0 \mathcal{G}^2)\,, \tag{3.18}$$

and depends on θ alone. As shown in Fig. 3.1, the shape of the magnetization varies significantly when changing the values of the two parameters σ_0 and b, and consequently also varies the magnetic field morphology.

Finally, from Eqs. 3.14 and 3.16 the number density is

$$n(r,\theta) = \frac{L_0}{4\pi c^3 m_e \gamma_0^2} \frac{1}{r^2} \left[\mathcal{F}(\theta) - \sigma_0\, \mathcal{G}^2(\theta)\right]. \tag{3.19}$$

Summarizing the three parameters (α, b, σ_0) represent the set of free parameters of the PW model, that must be fixed comparing the computed emission properties with observations.

3.3 Numerical particle tracers

To compute the emission properties of the PWN, it is necessary to have a direct information about the emitting particles, in particular their number density and energy at a given location inside the nebula.

The evolution of a single particle energy density (ϵ) in the post-shock region is ruled by adiabatic and synchrotron losses

$$\frac{d}{dt'}\ln\epsilon = \frac{d}{dt'}\ln n^{1/3} + \frac{1}{\epsilon}\left(\frac{d\epsilon}{dt'}\right)_{\rm sync}\,, \tag{3.20}$$

in which we have defined

$$\left(\frac{d\epsilon}{dt'}\right)_{\rm sync} \equiv -\frac{4e^4}{9m_e^3c^5}B'^2\epsilon^2 \tag{3.21}$$

and where $d/dt' \equiv \gamma(\partial/\partial t + \vec{v}\cdot\vec{\nabla})$ is the total time derivative with respect to time in the comoving reference system (apexed quantities).

The conservative expression of Eq. 3.20 can be achieved by combining it with the continuity equation for the density $\partial(\gamma\rho)/\partial t + \vec{\nabla}\cdot(v\vec{\gamma}\rho) = 0$ and defining the conserved variable $\mathcal{E} \equiv \epsilon_\infty\rho^{-1/3}$ (Del Zanna et al., 2006)

$$\frac{\partial(\gamma\rho\mathcal{E})}{\partial t} + \vec{\nabla}\cdot(\gamma\rho\mathcal{E}\vec{v}) = \frac{\mathcal{E}\rho}{\epsilon_\infty}\left(\frac{d\epsilon_\infty}{dt'}\right)_{\rm sync}\,, \tag{3.22}$$

with ϵ_∞ being the local maximum energy attainable, namely the energy at a given location that corresponds to an infinite injection energy.

The expansion of an element of the nebula volume is proportional to the ratio n/n_0, with n_0 the particle density immediately beyond the termination shock. In order to obtain the emission properties with great accuracy in the whole PWN, this ratio must be known with precision. This makes necessary to define two more tracers, which follow the number density n and its value downstream of the shock n_0 respectively. Following Camus et al. (2009), we thus add two more equations to the numerical model. The conservation of the number density is described by the equation

$$\frac{\partial(n\gamma)}{\partial t} + \vec{\nabla}\cdot(n\gamma\vec{v}) = 0\,. \tag{3.23}$$

Downstream to the TS, the particle number density n_0 must satisfy the transport equation

$$\frac{\partial(n_0 n\gamma)}{\partial t} + \vec{\nabla} \cdot (n_0 n\gamma \vec{v}) = 0\,, \tag{3.24}$$

meaning that the Lagrangian derivative of n_0 must be vanishing, thus n_0 remains constant along each fluid line beyond the TS. Until it reaches the shock front, n_0 is imposed to be equal to n, evolving as in Eq. 3.23, while it starts to evolve as in Eq. 3.24 at the density jump.

3.4 Synthetic emission recipes

The broadband Crab Nebula's spectrum can be reproduced only if the contribution of two families of emitting electrons is considered: one responsible for the low energy emission (radio particles) and one for the high energy emission (optical/X-ray particles). We continuously inject particles at the TS with broken power law spectra in energy (Amato et al., 2000). In the following we assume that the particles responsible for the optical/X-ray emission are, in all cases, constantly accelerated at the shock, while the radio emitting particles can have different origins: being part of the pulsar outflow and constantly accelerated at the shock, or uniformly distributed in the nebula (as will be largely discussed in Chap. 4).

The general form of the distribution function of newly injected particles in the nebula is given as

$$f_{0s}(\epsilon_0) = (p_s - 1)\,\frac{K_s}{\epsilon_s^{\min}}\left(\frac{\epsilon_0}{\epsilon_s^{\min}}\right)^{-p_s}, \quad \epsilon_s^{\min} \le \epsilon_0 \le \epsilon_s^{\max}\,, \tag{3.25}$$

where ϵ is the particle Lorentz factor, K_s a normalization factor, and the extremes of the distribution and the power-law index will be different, depending on whether radio or optical/X-ray emitting particles are considered, and determined from comparison with the data. The different specie of the injected particles (radio or optical/X-rays) is represented by the subscript s.

The local distribution function of wind particles at any place in the PWN is determined by the conservation of particle number along the streamlines, taking into account adiabatic and synchrotron losses

$$f_s(\epsilon) = \left(\frac{n}{n_0}\right)^{4/3}\left(\frac{\epsilon_0}{\epsilon}\right)^2 f_{0s}(\epsilon_0)\,, \tag{3.26}$$

where the injection energy is

$$\epsilon_0 = \left(\frac{n_0}{n}\right)^{1/3} \frac{\epsilon}{1-\epsilon/\epsilon_\infty}\,. \tag{3.27}$$

As already mentioned, factors n/n_0 take into account the changes in volume of the fluid element, and are computed by means of the aforementioned particle numerical tracers.

Given the local spectrum of the emitting particles, the synchrotron emissivity at all frequencies, surface brightness maps, and the integrated spectrum are computed through standard formulas. The synchrotron emissivity is established by the expression presented in Del Zanna et al. (2006). The synchrotron spectral power is calculated as

$$\mathcal{P}(\nu',\epsilon) = \frac{2e^4}{3m_e^2c^3} {B'_\perp}^2 \epsilon^2 \mathcal{S}(\nu',\nu'_c)\,, \tag{3.28}$$

where the apexed quantities are again referred to the comoving reference frame of the emitting particles. $B'_\perp$ is the magnetic field component normal to the particle's velocity whereas $\mathcal{S}(\nu',\nu'_c)$ is the spectral density, defined as

$$\mathcal{S}(\nu',\nu'_c) = \frac{9\sqrt{3}}{8\pi\nu'_c} F\left(\frac{\nu'}{\nu'_c}\right)\,. \tag{3.29}$$

The function $F(x)$ is such that the emission peaks around the critical frequency (a comprehensive discussion is given in Rybicki and Lightman (1979)) is

$$\nu'_c(\epsilon) = \frac{3e}{4\pi m_e c} B'_\perp \epsilon^2\,. \tag{3.30}$$

The local emission coefficient for a given observation frequency ν' and direction $\vec{n}'$ is thus given by

$$j'_\nu(\nu',\vec{n}') = \int \mathcal{P}(\nu',\epsilon) f(\epsilon) d\epsilon\,, \tag{3.31}$$

where the integral is extended to the whole energy range defined for the particle distribution function.

The emissivity in the observer's fixed reference frame can be obtained taking into account relativistic corrections. Both the frequency and the emission coefficient transform via the Doppler boosting factor

$$D = \frac{1}{\gamma\left(1-\vec{\beta}\cdot\vec{n}\right)}\,, \tag{3.32}$$

as $j_\nu = D^2 j'_\nu$ and $\nu = D\nu'$, where $\vec{\beta}$ is the normalized velocity of the fluid (respect to c). The connection between the observer direction versor $\vec{n}$ and the direction of emission

in the comoving frame $\vec{n}'$ can be obtained by applying the composition rules for relativistic velocities, giving

$$\vec{n}' = D\left[\vec{n} + \left(\frac{\gamma^2}{\gamma+1}\vec{\beta}\cdot\vec{n} - \gamma\right)\vec{\beta}\right]. \tag{3.33}$$

The Lorentz transformations of Maxwell's equations in the ideal MHD case also give

$$\vec{B}' = \frac{1}{\gamma}\left[\vec{B} + \frac{\gamma^2}{\gamma+1}(\vec{\beta}\cdot\vec{B})\vec{\beta}\right]. \tag{3.34}$$

After some algebraic manipulations, the required quantities can be written as

$$B' = \frac{1}{\gamma}\sqrt{B^2 + \gamma^2(\vec{\beta}\cdot\vec{B})^2}\,, \tag{3.35}$$

and

$$|\vec{B}'\times\vec{n}'| = \frac{1}{\gamma}\sqrt{B^2 - D^2(\vec{B}\cdot\vec{n})^2 + 2\gamma D(\vec{B}\cdot\vec{n})(\vec{\beta}\cdot\vec{B})}\,. \tag{3.36}$$

The last quantity is effectively $B'_\perp$: since radiation from ultra-relativistic sources is strongly beamed in their instantaneous direction of motion, within a cone of angle $1/\epsilon \ll 1$, only those particles with pitch angles coinciding with the angle between $\vec{B}'$ and $\vec{n}'$ contribute to the emission along the line of sight.

Finally, once the emissivity is known at any point in the nebula, surface brightness maps and total luminosity per unit frequency (basically the Spectral Energy Distribution) are calculated assuming the plasma to be optically thin, as appropriate for the tenuous plasma of PWNe. We have, respectively

$$I_\nu(x,y) = \int j_\nu(\nu,x,y,z)\mathrm{d}z\,, \qquad L_\nu = \iint I_\nu(x,y,z)\mathrm{d}x\mathrm{d}y\,, \tag{3.37}$$

where (x,y,z) is a Cartesian coordinates system in the observer frame and z defines the line of sight ($\vec{n}$), while (x,y) is the plane of the sky. Integrals are computed over the nebula dimensions.

Although in the present work we have been focused on the synchrotron emission only, the IC emission can be also computed on top of the simulated data. A complete analysis of the IC evaluation and results is presented in Volpi et al. (2008).

3.5 Simulated dynamics: shock structure and jets

The flow structure in cartesian coordinates is shown in Fig. 3.2, with a closeup of the TS in the left panel. The x and y labels represent the distance in ly from the central pulsar

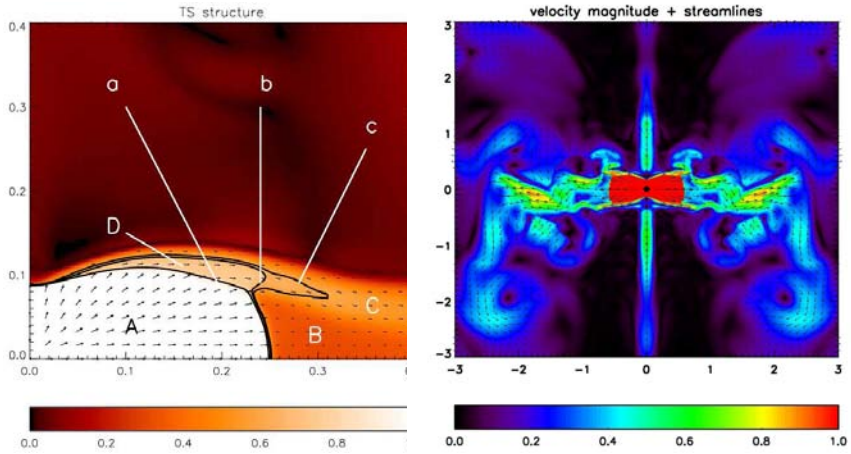

Figure 3.2: Plot of the flow velocity magnitude, with arrows indicating velocity streamlines. *Left panel:* closeup of the flow structures around the TS (from Del Zanna et al. (2004)). Capital labels refer to: A) the ultra-relativistic wind region; B) the subsonic equatorial outflow; C) the equatorial supersonic funnel; D) the super-fastmagnetosonic shocked outflow. Small letters refer to: a) the termination shock front; b) the rim shock; c) the fastonic surface. *Right panel:* closeup of the inner nebula, within a radius of 3 ly.

while the intensity of the velocity magnitude (c units) is expressed by the color scale on the bottom. Arrows indicate streamlines of the velocity field. As expected the TS shows an oblate shape due to the anisotropy of the wind energy flux, with a major extension in the equatorial direction, where the energy is maximum.

In the right panel many structures can be recognized around the TS surface (labelled with the small letter (a)): in region (A) the flow is radial and highly relativistic ($v \sim c$), with direction perpendicular to the shock front only at low latitudes (near to the equator), due to the obliquity of the TS. Region (B) is characterized by the equatorial subsonic flow, with $v \lesssim 0.6c$. In region (D) the flow speed remains super-magnetosonic, with $0.8c \lesssim v \lesssim 0.9c$, until it crosses the *rim shock* (b) (Komissarov and Lyubarsky, 2003). In region (C) the flow is slowed down to sub-magnetosonic but still supersonic speeds (with $0.6c \lesssim v \lesssim 0.8c$).

An MHD shock is able to convert efficiently the flow velocity from relativistic to sub-relativistic speeds only where the streamlines are perpendicular to the shock front. Thus the only region in which the conversion to a non-relativistic regime happens directly is the equatorial one, where the shock is highly oblique. In all the other regions a series of shock are needed to decelerate efficiently the flow. The rim shock (b) regulates a discontinuity, thus implies a change in the tangential flow velocity at crossing its surface. Small letter (c) identifies the fastmagnetosonic surface.

In Del Zanna et al. (2004) the evolution with time of the TS structure is discussed, and

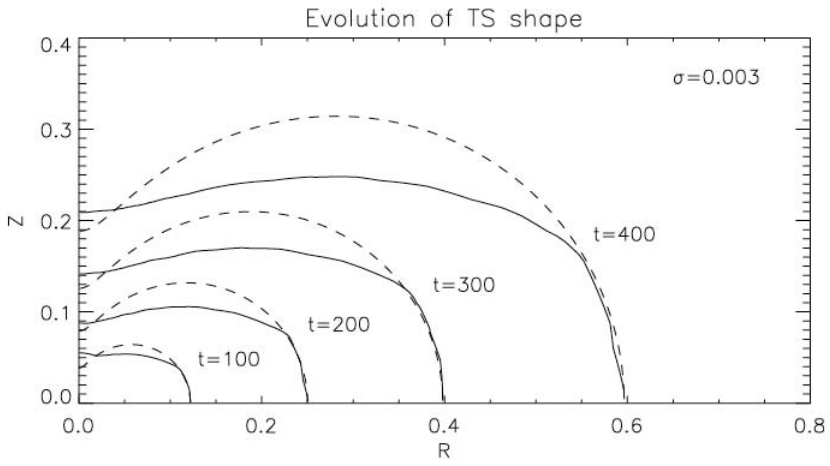

Figure 3.3: The evolution with time of the TS radius, for $\sigma = 0.003$ and in cylindrical coordinates (r, z). Dashed curves represent theoretical expectations for the shock position, as discussed in Del Zanna et al. (2004).

can be see here in Fig. 3.3 . Considering the downstream pressure to be constant, the TS shock profile at a given time would be simply defined by the condition

$$F(r, \theta) \cos 2\delta = \text{const.}\,, \tag{3.38}$$

where δ is the angle between the shock normal and the radius r. The resulting shapes of the shock at different times are shown as dashed lines in Fig. 3.3. With an anisotropy parameter of $\alpha = 0.1$, the approximation of constant pressure is reasonable only within an angle of $\sim 20°$ around the equator, thus deviations from the predicted shape at intermediate latitudes are due to pressure variations in the post-shock flow. The most important thing to notice is that the shock appears to evolve in a self-similar way. The same result is still valid in different σ regimes, as long as the PWN remains in the free expansion phase.

The presence of polar jets seems to be strongly connected to the post-shock flow pattern. As can be easily see in the right panel of Fig. 3.2, small and large scale vortexes appear to form in the post-shock equatorial flow or to detach from the edge of the oblique region of the shock. Due to the oblate shape of the TS, narrow stripes of supersonic post-shock flow form at the shock surface, converging to the equatorial plane, where they merge with the high speed flux. This flow tends then to run toward the outer boundaries of the nebula, but it is not able to reach the contact discontinuity. In fact, at a certain radius from the pulsar, equipartition between magnetic and thermal pressure is reached (Kennel and Coroniti, 1984a). Ensuring that the magnetization is high enough ($\sigma \gtrsim 0.01$), the equipartition is obtained very near to the shock front. There magnetic hoop stresses, amplified down-stream of the TS, become

sufficiently strong to divert the flow toward the polar axis, generating small scales vortexes and inhibiting the flow to reach the outer nebula. When the so generated back flow reaches the polar axis, it is in part collimated along the axis, forming the jet, in part redirected back to the equatorial plane and in part reaches the polar cusps of the TS, heating the plasma locally and driving again a polar outflow (Lyubarsky, 2002; Komissarov and Lyubarsky, 2003; Del Zanna et al., 2004).

The effect of these complex dynamics is the suppression of the equatorial flow at a few TS radii and the launching of a polar jet with high speed ($v \approx 0.7c$). When polar jets impact on the CD at the outer boundary of the nebula, the flow is suddenly diverted along the CD itself and pushed back to the equatorial region. Here it goes again toward the center, eventually dragging with it dense and cold material from the ejecta, crushing the inner part of the nebula.

Recently 3D simulations of the Crab jets are produced by Mignone et al. (2013). They found that highly magnetized flows ($1 \lesssim \sigma \lesssim 10$) lead to prominent deformations of the jet beam from the polar axis, due to kink instabilities, on time-scales comparable with observations ($\approx$ years). They also conclude that the dynamical behavior of the observed jet is better reproduced by low Lorentz factors ($\lesssim 2$) and moderately to high magnetized flow.

3.6 Synthetic high energy emission and integrated spectrum

Synthetic emitting properties are obtained from the simulated data following equations of Sec. 3.4. In order to obtain synchrotron emission and spectrum, power-law indices must be fixed. As already discussed, in the case of the Crab nebula more than a power law at injection is needed in order to account for the observed spectrum from radio to X-ray frequencies.

Assuming that optical and X-ray emissions come from the same particle family, in Del Zanna et al. (2006) high energy emission maps are produced, with a spectral index of $\alpha = 0.6$, as inferred from optical spectral index maps (Veron-Cetty and Woltjer, 1993). They computed X-ray maps for a typical value in the range of both Chandra and XMM-Newton, $h\nu = 1$ keV, while optical images are calculated for $\lambda = 5364$ Å, one of the wavelengths selected by Veron-Cetty and Woltjer (1993) as the less affected by thermal filaments emission. For a direct comparison with observed maps, synthetic images are rotated by 48° with respect to the North, and the nebula symmetry axis is inclined by 30° with respect to the plane of the sky (Weisskopf et al., 2000).

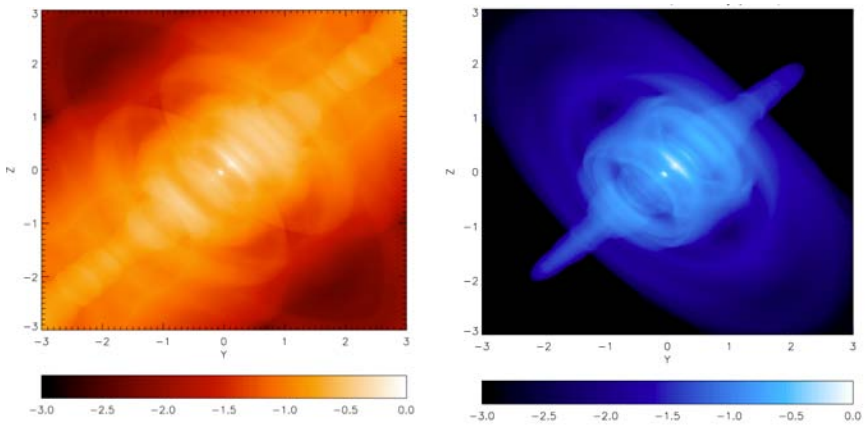

Figure 3.4: Optical (left panel) and X-ray (right panel) synthetic surface brightness maps from Del Zanna et al. (2006). Maps are reported in logarithmic scale and normalized to the maximum value of the intensity I_ν. Images are shown on a scale of (6×6) ly, with 1 ly $\simeq 32''$ for the Crab distance of $\simeq 2$ kpc.

Results for the best-fit case (with $\sigma = 0.025\,, \alpha = 0.1\,, b = 10$) are shown in Fig. 3.4. As expected optical emission is more diffuse than X-ray one, as the result of the synchrotron burn-off effect. On the other hand the two images are rather similar in the inner zone of the nebula, where bright ring, arc-like features and knots are clearly recognizable.

As shown in Komissarov (2004), these bright features are the effect of Doppler boosted emission coming from relativistic material moving toward the observer. As can be easily seen in Fig. 3.2, regions with the higher velocities are those around the TS front. Bright arcs and rings are then produced by external vortexes of material diverted by hoop stresses, and the knot is produced by the plasma escaping from the polar cusp of the TS and moving toward the observer.

In Camus et al. (2009) optical wisps are reproduced by subtracting two synthetic optical maps separated by an interval of ≈ 105 days, which is the observed variation timescale for optical wisps (Hester et al., 2002). The result is shown in Fig. 3.5, where moving wisps are visible as a sequence of black and white arcs. The authors argue that wisps are produced as a consequence of the highly dynamical behavior of the flow around the TS, which is highly turbulent and perhaps subjected to SASI [3]. This leads to great variations of the magnetic field and velocity with time, which are the reason for the wisps appearance.

strong variation and inhomogeneities in the magnetic field, which lead to strong varia-

[3]The Spherical Accretion Shock Instability, or SASI, is a hydrodynamic instability discovered by Blondin et al. (2003) in their numerical study of the stalled accretion shock in core-collapse supernovae. In 2D axisymmetry this instability drives an initially spherical accretion shock into a 'sloshing' mode in which it oscillates up and down the symmetry axis. This phenomenon has subsequently been seen in a variety of supernova simulations by numerous authors.

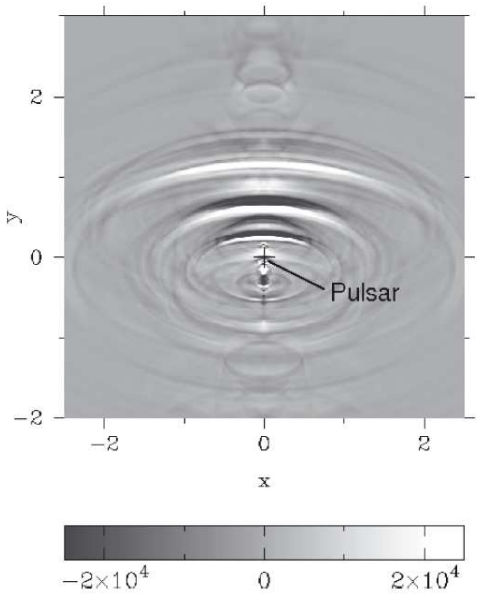

Figure 3.5: Optical wisps produced ad subtraction of optical surface brightness maps separated by a time interval of ∼ 105 days, taken from Camus et al. (2009).

tions in the synchrotron emissivity.

The Crab nebula integrated spectrum on top of a 2D axysimmetric RMHD simulation was first computed by Volpi et al. (2008). Here the inverse Compton (IC) emission is also evaluated using the Klein-Nishina differential cross-section (Blumenthal and Gould, 1970), and different photon targets for relativistic particles, namely: synchrotron emitted photons, photons from the dust thermal emission and photons from the cosmic microwave background (CMB).

Emission is again computed considering two different families of emitting particles, one responsible for the low energy emission (radio particles) and one for the high energy emission (optical/X-ray particles). Following Atoyan and Aharonian (1996) radio particles are considered as a sort of relic population, uniformly distributed in the nebula. On the other hand, high energy particles are continuously injected at the TS and evolved in the nebula. The authors find that the spectral break between the infrared (IR) and optical arises as a natural consequence of the superposition of the two distribution functions for the emitting particles. On the contrary the second spectral break (UV wavelengths) corresponds to the strong synchrotron burn-off effect.

In Fig. 3.6 the integrated spectrum from the cited work is shown. As can be easily see, X-ray emission is strongly overestimated with the standard value of the optical/X-ray spectral index of ∼ 0.6. This is caused by the compression of the magnetic field around the polar axis

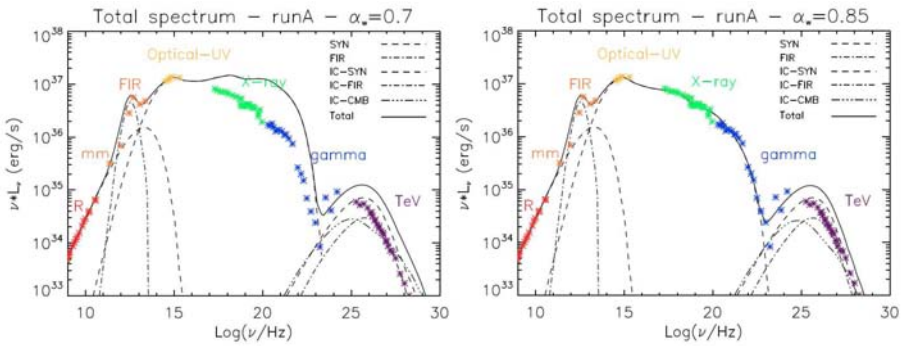

Figure 3.6: The integrated spectrum of the Crab nebula from Volpi et al. (2008), with the observational data on top of it. In the left panel the spectrum is computed with the expected value for the optical spectral index (from observation $\alpha_w \sim 0.6 \div 0.7$). In the right panel the spectral index is raised to $\alpha_w = 0.85$ in order to fit the X-ray component of the spectrum.

and close to the TS, which leads to a volume-averaged value of the field which is smaller by a factor of $2 \div 3$ with respect to the predicted value ($\sim 200\,\mu$G). This is probably an effect of the dimensionality of the simulation, as we will discuss in Chap.4. As the averaged field is lower, electrons are affected by lower synchrotron losses and thus a steeper spectral index is require to fit the high energy spectrum.

The calculation of the IC spectral component indicates that this also leads to a large number of emitting electrons, which cause the overestimation of the gamma-ray emission as well.

The authors conclude that in order to reproduce correctly the whole spectrum of the Crab nebula, a larger, and more diffuse, magnetic field is absolutely essential. As we will discuss in the following, the problem of the magnetic field morphology will be hopefully resolved moving to 3D models, since it seems to be an intrinsic feature of axisymmetric 2D simulations.

Chapter 4

The Crab nebula radio emission

In recent years, it has become a well-established paradigm that many aspects of the physics of PWNe can be fully accounted for within a relativistic MHD description. Numerical simulations have proven extremely successful in reproducing the X-ray morphology of the Crab nebula, down to very fine detail. Radio emission, instead, is currently one of the most obscure aspects of the physics of these objects, and one that holds important information about pulsar properties and their role as antimatter factories.

In Olmi et al. (2014) we address the question of radio emission morphology and integrated spectrum from the Crab nebula, by using for the first time an axisymmetric dynamical model with parameters chosen to best reproduce its X-ray morphology.

In this Chapter we will discuss our findings and the constraints on the origin of the radio emitting particles that can be deduced from our analysis.

4.1 Introduction

As already mentioned, PWNe are a privileged location to look for answers to old and new questions in pulsar physics, since they collect most of the rotational energy lost by the parent pulsars. While pulsars are thought to be the primary leptonic antimatter factories in the Galaxy, a big open question concerns the exact amount of pair production in their magnetospheres, the so-called pair multiplicity κ. In this time of new observational and theoretical developments on the subject, modeling of PWNe is likely to provide the most solid constraints (Bucciantini et al., 2011).

In the last few years the axisymmetric relativistic MHD models of PWNe (Komissarov and Lyubarsky,

2004; Del Zanna et al., 2004, 2006) have proven extremely successful at accounting for the properties of these objects as observed in the optical/X-ray band. These models identify in the anisotropy of the pulsar outflow, more energetic in the equatorial plane of the pulsar rotation than along the polar axis, the origin of the jet-torus morphology revealed by Chandra in many of these nebulae (Weisskopf et al., 2000; Gaensler and Slane, 2006). In addition they provide a simple explanation for the time variability observed in the inner region of the Crab nebula (Volpi et al., 2008; Camus et al., 2009) and for much of the finer scale structure of the emission.

So far, MHD modeling of PWN radiation has focused on high energy photons, while completely ignoring the low frequencies, in spite of the fact that the correct interpretation of PWN radio emission is of fundamental importance for understanding many aspects of PWN and pulsar physics. The big question to assess is whether the radio emitting particles are continuously injected in the nebula as part of the pulsar wind and accelerated at the termination shock, or they can rather have a different origin and acceleration site. Indeed, if the radio emitting particles are continuously injected in the nebula together with the optical/X-ray emitting ones, then the inferred pulsar multiplicities are typically larger than current pulsar theories are able to explain (Hibschman and Arons, 2001). For example, in the case of the Crab nebula, including low energy particles in the pulsar outflow one finds the pulsar multiplicity $\kappa \sim 10^6$ and a wind Lorentz factor, averaged over solid angle, $\gamma \sim 10^4$ (Bucciantini et al., 2011). If radio emission comes from particles of a different origin, then, from higher frequency observations one deduces $\gamma \sim 10^6$ and $\kappa \sim 10^4$ (e.g. Kennel and Coroniti, 1984a; Gaensler et al., 2002). The value of these two parameters has also important consequences in terms of constraining the acceleration process at work at the wind termination shock (Sironi and Spitkovsky, 2011; Arons, 2012).

The radio emitting particles, with their large number and long life-times against synchrotron losses, could also be relics of earlier times, when the pulsar wind was different from now (Atoyan and Aharonian, 1996). Or they could come from somewhere else than the pulsar wind, with a possible source being the thermal filaments penetrating the relativistic bubble (e.g. Komissarov, 2013). In the latter case the electrons would have to be accelerated locally to relativistic energies. A possible mechanism to this purpose relies on scattering off local turbulence (Fermi II type process), providing, at the same time, acceleration and spatial diffusion, so as to guarantee a smooth distribution of the radio emission throughout

the nebula, despite the presence of enhanced emission associated with the filaments. In the presence of efficient scattering by local turbulence, a rather uniform distribution of particles would also be expected in the case in which the particles are re-accelerated relics, namely they were injected at the termination shock only for a short time during the PWN lifetime, but then re-energized by the interaction with turbulence.

In this Chapter we investigate the problem of the origin of radio emitting particles. For the first time we compute radio emission maps based on the flow structure that arises from the 2D axisymmetric MHD simulation that best reproduces the Crab nebula X-ray emission. We compare the emission morphology under three different hypotheses: A) assuming that radio particles have always been accelerated at the termination shock; B) taking their distribution as uniform in the nebula, as could be possibly expected if after being injected, at the shock or by the filaments, they were (re-)accelerated by ambient turbulence; C) assuming that they were only injected at the termination shock in the nebula for a relatively short time after the supernova explosion and with no further re-acceleration.

One piece of information that seems to point towards a common origin of the radio emitting and higher energy particles is the observed continuity of the integrated emission spectrum of the Crab nebula, from which continuity of the spectrum of the emitting particles has traditionally been inferred. For other PWNe, the data are just not good enough to allow to assess this issue, also due to the scarcity of observations of these objects in the IR and optical band, which is where the transition between different spectral slopes usually occurs. In the presence of a uniform magnetic field strength, as assumed by 1-zone models, a smoothly joined emission spectrum between radio and optical implies a smooth spectral distribution of the emitting particles. In the presence of a spatially inhomogeneous field, this is not a straightforward inference, since the volume occupied by particles of different energies is different (larger at lower energies) and so is in principle the field strength. We investigate the paradigm of continuity and smoothness of the particle spectrum in the Crab nebula and show that the IR bump of thermal emission associated to dust could easily hide a possible gap between radio and optical emitting particles.

This chapter is organized as follows: in Sec. 4.2 we recapitulate briefly the the adopted pulsar wind model and the assumptions on the particle spectrum; in Sec. 4.3 we present our results and discuss the implications of different models, and we conclude in Sec. 4.4.

4.2 Pulsar wind model and particle emission

The initialization and set up of our 2D numerical simulation was already described in 3. In order to have a very fine representation of the whole nebula, especially in the inner zone, we use here a very high spatial resolution. The physical domain, $0.05\,\mathrm{ly} \leq r \leq 10$ ly and $\theta \in [0, \pi]$, has 800 cells in the radial direction and 400 cells in the polar angle θ.

The PW is modeled following the prescriptions discussed in 3.4, with the set of the free parameters is the one which best account for the high energy properties of the Crab nebula, as discussed in the next section.

As already mentioned, we always assume that the particles responsible for the optical/X-ray emission are, in all cases, constantly accelerated at the shock, while the radio emitting particles can have different origins: be part of the pulsar outflow and constantly accelerated at the shock (Case *A*); uniformly distributed in the nebula (Case *B*); resulting from a burst of acceleration at the shock, only lasting for a limited time (of order 10% of the nebular age), and then advected in the nebula, with no spatial diffusion or further re-acceleration (Case *C*).

We would like to point out, right from the beginning, that Case *C* corresponds to a model of relic particles that were injected in the nebula at some early time, when the pulsar was spinning down in a different way, either in terms of overall L_0 or in terms of producing a different multiplicity. This pure relic model, in which the particles are not re-accelerated in the nebula after their initial early injection, is only considered to the purpose of illustrating how the emission morphology would change under this extreme assumption. Indeed, a model of relics that does not conflict with any energetic requirement is likely to give rise to a particle distribution close to that assumed in Case *B*. Here the underlying physical picture is that of particles being scattered and accelerated by turbulence in the nebular volume. No matter whether they are extracted from the thermal bath of the filaments or whether they were injected at the shock at early time, the interaction with turbulence that ensures (re)acceleration also smoothes out all the spatial gradients.

Since both model *A* and *B* give results in reasonable agreement with the data, in the following we discuss them in parallel, while treating Case *C* separately.

The general form of the particle distribution functions is again described in 3, with special reference to Eq. 3.25 and Eq. 3.26. Here the value of n_0 is used to normalize the distribution function of particles that are of wind origin (Case *A*): for these we take $K_s = \xi_s n_0$ and determine ξ_s from fitting the data. When we consider Case *B*, the spatially homogeneous (and

Radio		optical/X-ray	
Parameter	Value	Parameter	Value
p_R	1.6	p_X	2.9
$\epsilon_R^{\min}$	1.0×10^3	$\epsilon_X^{\min}$	7.0×10^5
$\epsilon_R^{\max}$	2.0×10^5	$\epsilon_X^{\max}$	4.0×10^9
ξ_R	1.7×10^{-2}	ξ_X	2.2×10^{-4}

Table 4.1: Spectral fit parameters for the two families $f_R(\epsilon_0)$ and $f_X(\epsilon_0)$.

constant in time) distribution function of radio particles is simply given as $f_R(\epsilon) = f_{0R}(\epsilon_0)$, with $\epsilon_0 \equiv \epsilon$ and $K_R = n_R = \text{const}$ in Eq. 3.25. With the local spectrum of the emitting particles, all the emission properties are then computed my means of the synchrotron formulas in 3.4.

4.3 Simulation results

This section is devoted to comparison of the radio emission morphology resulting from the different assumptions on low-energy particle acceleration illustrated above. We have performed several numerical simulations aimed at determining what values of the dynamical parameters lead to emission maps that most closely reproduce the Crab nebula morphology at high energy. With respect to previous work on the subject (see Del Zanna et al., 2006; Volpi et al., 2008), we have explored a much wider portion of parameter space, including values of σ_0 larger than unity, and also varying, for the first time to our knowledge, the wind anisotropy parameter α. Detailed results of these simulations will be presented elsewhere, while for the current purpose what is important is the identification of the flow parameters that provide the best description of the Crab nebula X-ray morphology. Even if we employ a different simulation set up, the best set of values for the free parameters is still that found by Del Zanna et al. (2006): $\alpha = 0.1$, $\sigma_0 = 0.025$, $b = 10$. The parameters describing the particle spectrum at the basis of the emission are reported in Table 4.1, and will be discussed later on.

In Fig. 4.1 we show the (toroidal) magnetic field at $t = 950$ yr of evolution. The size of the termination shock ($\simeq 0.7$ ly at the equator) and that of the contact discontinuity with the expanding ejecta ($\simeq 7$ ly) are approximately as observed. The field changes polarity around the equator and eddies cause the current sheet to twist and tangle in the downstream, creating a strong mixing of the field (*islands* of opposite polarity can also be seen) and consequent

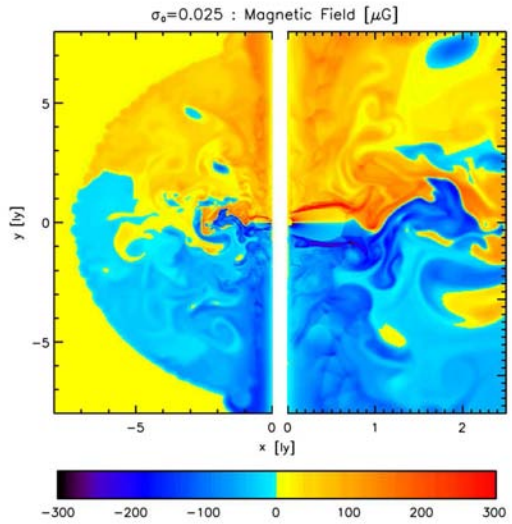

Figure 4.1: The magnetic field distribution in the simulated nebula.

dissipation (Bucciantini and Del Zanna, 2013). The field is lower than expected basically everywhere: well below 10^{-4} G in the external regions and $\simeq 2 \times 10^{-4}$ G just downstream of the termination shock and within a cylindrical region of radius $\sim$ 1 ly around the polar axis (where a jet is present due to magnetic hoop stresses).

4.3.1 Shock versus distributed particle acceleration

In this subsection we compare the radio emission morphology resulting from assumptions *A* and *B*, namely ongoing acceleration of the low energy particles at the termination shock, followed by advection with the flow (in perfect analogy with optical/X-ray emitting particles, Case *A*), or uniform distribution in the whole nebular volume (Case *B*).

The radio emission maps, which are here computed for the first time on top of MHD simulations, directly reflect the magnetic field structure, and, at some level, the structure of the velocity field (due to Doppler boosting). In the top row of Fig. 4.2 we show the results of Case *A*, whereas the lower row pertains to Case *B*.

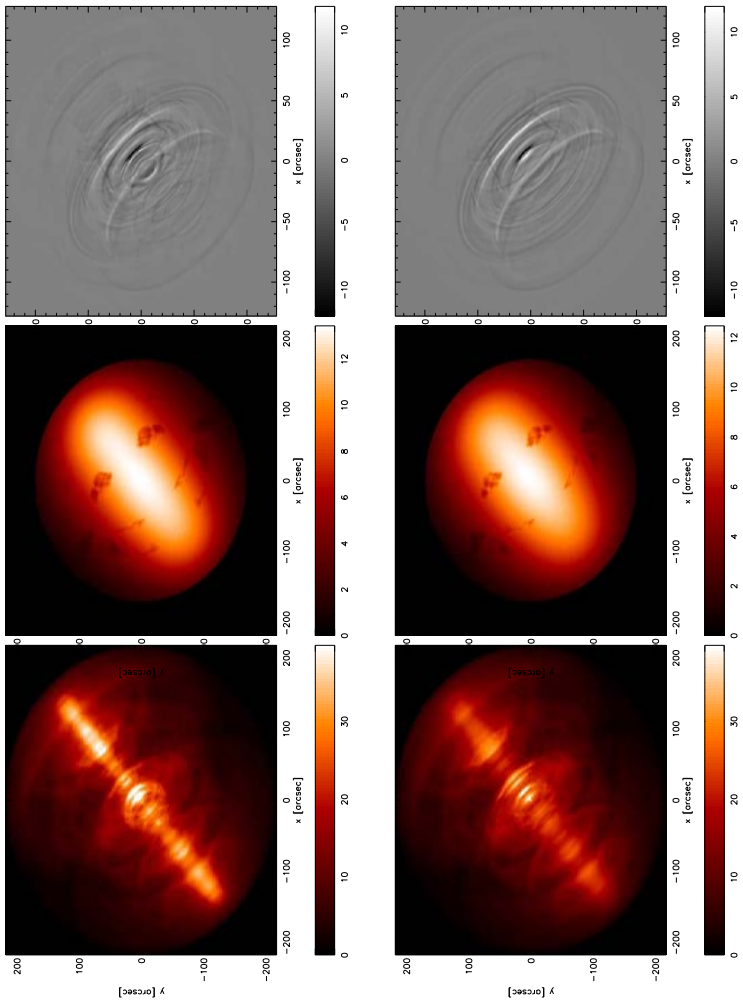

Figure 4.2: Simulated maps of radio emission and wisps at 1.4 GHz, expressed in mJy/arcsec^2. *Left panels*: surface brightness maps; *middle panels*: surface brightness maps with subtraction of small scales; *right panels*: wisps obtained by subtracting two surface brightness maps with a time separation of two months. The upper row refers to Case *A* and the lower one to Case *B*, for which $n_R = 1.4 \times 10^{-6}\mathrm{cm}^{-3}$.

In the left panels we report the surface brightness maps at 1.4 GHz. The maps computed under the two different assumptions on the origin and distribution of radio emitting particles are basically identical. Ring-like structures, very similar to those observed in the optical and X-rays are clearly seen at these long wavelengths too. Their appearance is in fact only due to local enhancements in the magnetic field and Doppler boost associated with the local velocity field. In the right panels we show images obtained by subtracting two maps computed for epochs that are two months apart: wisp-like motion is clearly seen also at radio wavelengths, in perfect agreement with what observed by Bietenholz et al. (2004). Again, no substantial difference between the two cases *A* and *B* can be noticed, the only discrepancy being due to the central slightly brighter features. Our conclusion is that the appearance of radio wisps does not bear any implication on the injection site of the emitting particles, but only on the underlying flow structure.

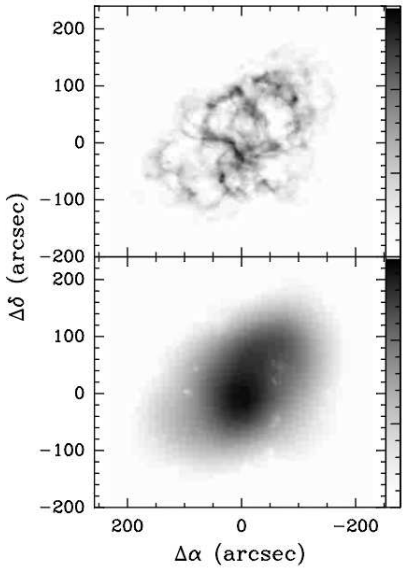

Figure 4.3: 1.4 GHz surface brightness map from Bandiera et al. (2002). In the upper panel the filamentary structures, subtracted in the bottom figure, are shown. The intensity is expressed in mJy/arcsec^2.

On the other hand, the emission structure we find appears to be too strongly concentrated in the axial direction in comparison with observations: this is again independent on the assumed spatial distribution of particles in the nebula. One could argue that such an effect is actually present in the real data but masked by the presence of thermal filaments, which give a non-negligible contribution in this band. We compared our results with the map at 1.4 GHz published by Bandiera et al. (2002), where subtraction of the filaments was performed (reported in Fig. 4.3). In the central panels of Fig. 4.2 we show our emission maps smoothed

with the same technique and using the same units of mJy/arcsec^2 as in the cited work for direct comparison. This smoothed maps appear to be very similar to the one based on observations from both a qualitative and quantitative point of view. The computed emission shows a strong cylindrical symmetry, somewhat at odds with the ellipsoidal structure in the data. Once more, results for Case *A* and *B* are nearly undistinguishable.

The reason for the latter discrepancy is likely related to the fact that axisymmetric simulations do not provide a good description of the magnetic field on large scale. Kink-type instabilities that are likely to be at work in these nebulae (Begelman, 1998), are artificially suppressed in 2D. This might reflect in a simulated magnetic field that has a much higher degree of order than in reality: the discrepancy will become more apparent in the emission the further one moves from the central pulsar, so that the instabilities have time to grow. This fact makes the radio emission the most sensitive probe of such an effect, and at the same time it explains why with axisymmetric simulations we are able anyway to reproduce the high energy morphology: the short lifetimes of optical/X-ray emitting particles keeps them confined within a region where a perfectly toroidal magnetic field is still not such a bad approximation. An additional hint to such an effect comes from the observation that in order to reproduce the observed brightness contrast between the inner ring and torus at X-ray frequencies the emission must be computed assuming that the underlying magnetic field progressively becomes isotropic with increasing distance from the termination shock: the ring is otherwise too bright.

The artificially high degree of order of the magnetic field is obviously accompanied by important dynamical consequences. The associated hoop stresses are also larger than in reality and might be forcing us to adopt an artificially small value of the magnetization in our simulations. Strong suggestions that this is the case also come from Fig. 4.4, where we plot the integrated emission spectrum of the Crab nebula as computed based on our simulation, and we compare it with multi-wavelength observations. The particle distribution functions adopted are as described in Sec. 3.4 with the parameters given in Table 4.1. In spite of the good fit of the synchrotron part of the spectrum, the exceedingly low magnetic field strength in the nebula is revealed by a careful inspection of the fit parameters: the spectrum of optical/X-ray emitting particles that is required to reproduce the observations is very steep (see Table 4.1), with a slope of $p_X = 2.9$, to be compared with the value $p_X = 2.2$ that is deduced from observations of the inner nebula (Veron-Cetty and Woltjer, 1993; Mori et al.,

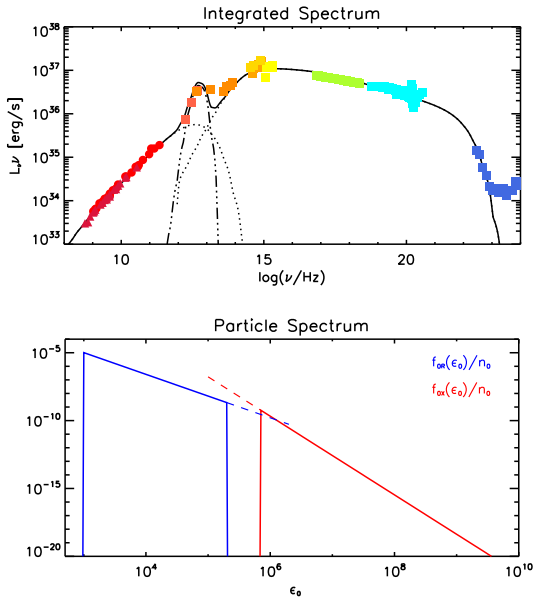

Figure 4.4: The Crab nebula integrated synchrotron spectrum. Data are taken from Meyer et al. (2010). Dotted lines indicate the contributions from the two families of emitting particles, whereas the solid one represents the total spectrum. The injection spectra are shown in the bottom panel for the case of radio particles of wind origin (Case *A*). The left (radio particles) and right curve (optical/X-ray) correspond to the parameters in Table 4.1.

2004a).

This is due to the fact that synchrotron losses are too weak in our simulation and do not provide sufficient softening of the injected particle distribution, so that we are forced to assume a steep injection spectrum in order to reproduce the high energy observations. However, this becomes even more apparent from the gamma-ray flux due to the IC contribution, which, when calculated self-consistently by integrating over the whole nebular volume, is higher by a factor $\sim$ 3 compared to observations. This is precisely the discrepancy we have in the average magnetic field value: in order to reproduce the synchrotron spectrum we are forced to inject more particles in the PWN, leading to a higher IC flux. This was already found and described in details by Volpi et al. (2008): very similar findings apply to the simulations with the present settings.

Finally, let us comment on the properties of the particle distribution function underlying the emission, focusing on Case *A*. This case corresponds to the spectrum described in Table 4.1 and Fig. 4.4 (top panel). First thing to notice is that the spectrum of emitting particles we adopt has a gap between the radio and the X-rays. The size of the gap is not well established from our fit: anything between no discontinuity ($\epsilon_r^{\max} = \epsilon_X^{\min}$) and a discontinuity extending to an energy a factor of 3-4 lower than $\epsilon_X^{\min}$ works well (the ratio for our best fit

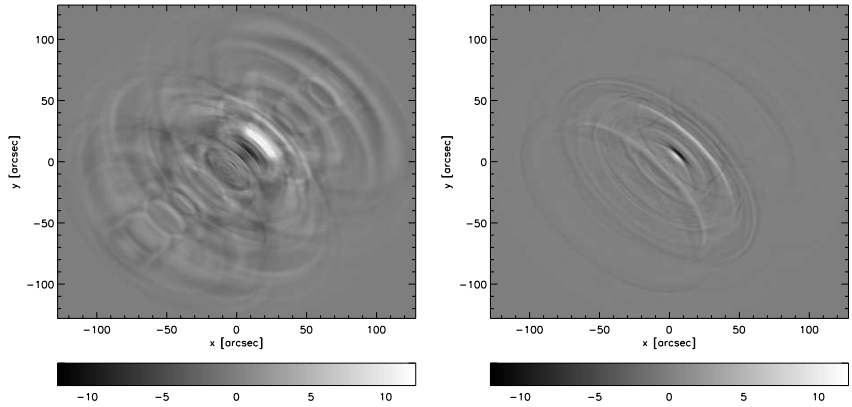

Figure 4.5: Changes occurring in the nebula on a 3 yr time-scale (*left panel*) and on $\sim$ 2 months (*right panel*), at 5 Ghz. Moving ripples and arc-like structures are well visible in both images. On the x an y axes the distance from the central pulsar in arcsec is reported. The two maps are expressed in mJy/arcsec^2.

is 3.5). This result is obtained with sharp cut-offs in the particle spectra both at high and low energy; while with exponential cut-offs larger gaps would be allowed. In addition, our best fit corresponds to a discontinuous distribution at injection, in the sense that the two curves do not match in the gap region and that extrapolation of the low energy spectrum to $\epsilon_X^{\rm min}$ would give half of the particles that are actually required at this energy. However, this discrepancy should not be trusted because, as already discussed, inference of the particle spectrum depends on the magnetic field strength and profile and we know that in reality this will be different than in our current axisymmetric simulations. Indeed, the spectra described in Table 4.1 correspond to conversion into accelerated particles of a fraction larger than one of the pulsar spin-down luminosity.

4.3.2 On the variability of radio "wisps"

We have seen in the previous subsection that radio wisps are easily reproduced by our relativistic MHD model. Here we investigate their variability properties following the analysis by Bietenholz et al. (2004). These authors studied long-term variability of the radio emission component through observations during a $\sim$ 3 yr period, together with much shorter-term variations (time-scale of a few months) in the innermost region of the nebula. For direct comparison with this analysis of time-variability, we use maps that are computed at 5 GHz, instead of the previously used frequency of 1.4 GHz. As above, the difference images are obtained by subtraction. We only discuss maps corresponding to Case B, since those for

Case *A* are very similar.

In Fig. 4.5 the radio emission difference maps at 5 GHz are shown: the long-term is shown in the left panel, short-term in the right one. As one can expect, the right panel corresponds to the radio wisp-like structures in the inner region of the nebula, just as in the maps at 1.4 GHz already shown (images on the right in Fig. 4.2). As far as the long-term map is concerned, the first thing to notice is that a significant component of the variability has a time-scale longer than that of the wisps. The region that shows long term variability extends for $\sim$ 3 ly around the pulsar, namely it is twice as large in linear size as the region showing short-term variability. Additional remarkable features in the image on the left of Fig. 4.5 are: elliptical arcs, found in the central zone and characterized by an outward motion, similar to the optical/X-ray wisps; arc-shaped features that are visible in the body of the nebula, are not centered on the pulsar position and move outward more slowly than the former (Weisskopf et al., 2012; Schweizer et al., 2013). The inferred projected speed for the inner wisps is $\sim 0.4c$ while for the outer moving features is $\sim 0.002c$, as expected from the data analysis.

All these features were found in the data analysis by Bietenholz et al. (2004) and are well reproduced by our axisymmetric model both in shape and associated velocity. We stress again the conclusion that the appearance of wisps simply reflects the underlying structure of magnetic and velocity field (due to Doppler boosting). The result is not much affected by the different spatial distribution of the particles in the 2 cases *A* and *B*: indeed, even in the case of acceleration at the shock and following advection (*A*), thanks to their long lifetimes, the radio particles are everywhere in the nebula and strong gradients are absent.

4.3.3 Pure "relic" particles: no re-acceleration

In this section we discuss what we had defined as our Case *C*. We consider a model in which radio emitting particles are pure relics: they are injected at the termination shock (as the optical/X-ray emitting one) but only at early times after the SN explosion. The injection of low energy particles is then halted after a certain time $t_{\rm b} \ll t_{\rm act} \simeq 950$ yr, while continuing for the the higher energy ones. After injection all particles evolve due to synchrotron and adiabatic losses, while advected with the flow. This time-dependent injection model is meant to represent a sort of primordial *burst*, possibly associated to a different *behavior* of the pulsar in its early stages, when the spin-down luminosity was almost an order of magnitude greater

than the current one (Atoyan, 1999): what we have in mind is in fact a higher multiplicity at early times. Our attention is then focused on the final spatial distribution of the radio particles and on the resulting emission map.

Also for the present Case *C* the simulation set-up is the same as before, except for the particle tracers that are now defined only for the radio population, with the new value of the maximum local energy set as $\epsilon_\infty = 10^6$.

This value is chosen in order to guarantee a proper representation of the radio emission spectrum. In Sec. 4.3 we found that the radio spectrum is currently produced by particles with energy up to a cut-off $\epsilon_b \simeq 2 \times 10^5$. The most recent radio particles were injected in the nebula at the time t_b corresponding to the end of the burst. Since then they have been losing energy due to adiabatic, and, initially, also synchrotron losses: at early times the average magnetic field in the nebula was larger than its current value making synchrotron losses important also for 100 GeV particles. This fact actually constrains the burst duration: if we want the current spectrum of radio emitting particles to still extend up to the value of ϵ_b mentioned above, we require that the burst must have lasted at least for a time:

$$\left(\frac{B_{\rm act}}{50\mu G}\right) \text{yr} \,, \tag{4.1}$$

where we have used standard synchrotron formulae and approximated the time evolution of the average magnetic field strength as $B(t) \propto t^{-1}$ (Pacini and Salvati, 1973). Since the average magnetic field in our simulation at the current age of the Crab nebula is $B_{\rm act} \sim 50\mu G$, we take $t_b = 100$ yr.

We would like to point out however, that if the magnetic field in our simulation were closer to more realistic values (values in agreement with high energy spectral modeling), and hence a factor 2-5 larger, the lower limit on the burst duration would have been proportionally larger. Therefore, in reality, the highest energy radio emitting particles must have been injected in the nebula no earlier than $\sim$ 500 yr ago, which makes one wonder what might have caused a sudden change in the pulsar multiplicity or spin-down properties long after birth.

In Fig. 4.6 we show the density tracer at different times (left and middle panels) and the radio surface brightness map at $t = 1000$ yr (right panel). In the image on the left, the density of radio particles is shown at the final stage of injection ($t = t_b$), and its spatial distribution appears almost uniform in the nebula. The middle panel refers to the final stage of evolution, $t \simeq 1000$ yr, and two main differences are evident compared to the first map: the mean

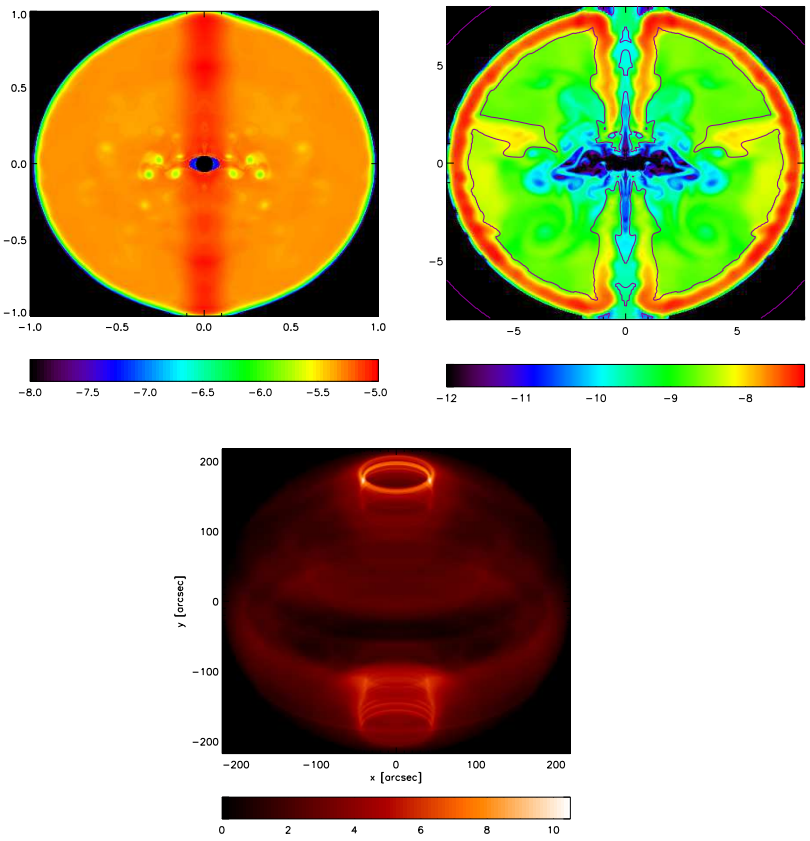

Figure 4.6: Radio particle density maps at $t = t_b = 100$ yr (*left panel*) and at $t = 1000$ yr (*middle panel*); both maps are in logarithmic scale and on the x and y axes the radial distance from the pulsar is reported in ly. The line contour in the second map traces the high density region in the dynamic density map at the same stage of evolution, connected to the high density region in the tracer map: see text for more details. *Right panel*: surface brightness map at 1.4 GHz, in linear scale and normalized at the maximum value.

value is decreased by about three orders of magnitude and its distribution is not uniform anymore.The lower value of the density results from the adiabatic expansion of the nebular volume.

Furthermore, notice that a sort of higher density shell is visible at the outer edge of the nebula. This is caused by the accumulation of part of the dynamical mass density in that region in the early stages of evolution. Then vortices develop in the nebular flow pattern that confine the circulation in the body of the nebula, preventing new material from reaching the outer shell. As a consequence, the material that settled down there at the beginning does not get mixed anymore. The density of radio particles behaves exactly as mass density and this is the reason for the pattern that we observe in the figure. The same mechanism is at the base of the high density *fingers* in the NW and NE regions of the nebula.

The line contour in the middle panel of Fig. 4.6 identifies the region of high mass density concentration. The radio surface brightness map in the right panel of Fig. 4.6 is computed with that region subtracted. In order to allow for direct comparison with the spatial distribution of particles, the emission map is not rotated in the plane of the sky, while is inclined with respect to the line of sight, so as to correctly take into account Doppler boosting. Despite having removed most of the spurious effects of numerical origin, the emission morphology is clearly discrepant with respect to observations. The emission is diffuse, but the central region is much darker than observed. While the ring-like structures in the outer region of the nebula are likely related to residual spurious features near the impact regions of the jet, the absence of "wisp-like", Doppler boosted structures in the inner region is a real difference between this map and the ones shown in the left panel of Fig. 4.2. This difference arises from the fact that there are no radio emitting particles left at the current time in the innermost region of the nebula, where the field strength is highest and the flow is most dynamic and with the fastest speed.

We have also tried different durations of the burst, while with shorter durations the emission spectrum does not extend to sufficiently high energies, a factor 2-3 longer duration leads to qualitatively similar results. What we learn from this simple model, then, is that the radio particles cannot be described as a relic population of pulsar origin without including a local re-acceleration mechanism in the nebula.

4.4 Summary and comments

Up to the present 2D MHD axisymmetric simulations are regarded as very successful in reproducing the high energy morphology of the Crab nebula, but the properties of the low energy emission are usually not considered at all. The novelty of the work presented in this chapter resides in the first attempt ever at a detailed study of the low energy emission within the framework of 2D MHD.

What we conclude here is that a radio emission morphology appears to be roughly insensitive to the spatial distribution of the particles in the two scenarios we considered: advected with the flow from the pulsar wind termination shock, or uniformly distributed in the nebula. The computed surface brightness maps are basically identical, but furthermore moving wisps at radio frequencies appear in both cases, and actually both the innermost fast moving features and the larger scale slower ones, in agreement with the observations by Bietenholz et al. (2004). In terms of variability, we compared the results of our simulations with the cited observations. The fact that the variable structures are well reproduced in our simulations independently of the spatial distribution of the particles points toward the conclusion that these details cannot really prove the origin of the radio emitting particles.

The only scenario that can be excluded is one in which the low energy particles are "pure relics", injected at early times after the SN explosion and then evolved in the absence of further acceleration and spatial diffusion. We were able to directly prove that this scenario does not work in the case of particle injection for less than 400 yr during the history of the nebula. In reality, the requirement on the last episode of acceleration of radio emitting particles would be even more stringent (closer in time episode) if the magnetic field in the simulated nebula were higher. In summary, radio emitting particles could only be fossil in terms of their injection in the nebula, but not in terms of their acceleration history.

As far as acceleration mechanisms are concerned, apart from shock acceleration, the low energy particles could, in principle, be re-accelerated (if coming from the shock, or accelerated if coming from the thermal filaments) by distributed turbulence in the nebula, either of kinetic origin, injected by the higher energy population of particles, or of MHD origin. Two main sources can be envisioned for the latter: the highly dynamical behavior of the shock front and nearby eddies where small-scale flows easily form and have been even invoked as sources of the gamma-ray flaring activity (Komissarov and Lyutikov, 2011), or the growth of local Kelvin-Helmoltz MHD instabilities at the shear layers of neighboring

wisps (Bucciantini and Del Zanna, 2006). Another possibility, actually supported by the results of Porth et al. (2013a) is that effective magnetic reconnection in the body of the nebula might also provide particle acceleration: this hypothesis is particularly attractive also because this mechanism naturally seems to provide flat energy spectra, just as generally inferred for young PWNe.

The possibility of explaining radio observations without requiring that the radio emitting particles must be part of the pulsar wind relaxes somewhat the strong requirements on the multiplicity of the Crab pulsar found by Bucciantini et al. (2011). However, explaining the very large number of these particles is still problematic and deserves further investigation. If they are of pulsar origin, then the pulsar multiplicity must have been high at some point in time, and then have possibly decreased to accommodate for current observations of X-ray emitting particles. On the other hand, the radio emitters could also be produced elsewhere in the nebula, for example in the thermal filaments due to Rayleigh-Taylor instabilities (Bucciantini et al., 2004), in which case they would only be electrons rather than pairs. In this case, contrary to recent claims (Blasi and Amato, 2011), PWNe could not be responsible for the *positron excess* recently detected (PAMELA coll., 2009; AMS-02 coll., 2013), (for a review see also Serpico, 2012). This explanation is not very appealing, especially because very similar radio spectra are observed in bow-shock PWNe (e.g. Ng et al., 2012), and in these sources the particles are extremely unlikely to come from anywhere else than the pulsar.

Chapter 5

Constraints on particle acceleration sites in the Crab nebula

The Crab nebula is one of the most efficient accelerators in the Galaxy and the only galactic source showing direct evidence of PeV particles. In spite of this, the physical process behind such effective acceleration is still a deep mystery. While particle acceleration, at least at the highest energies, is commonly thought to occur at the pulsar wind termination shock, the properties of the upstream flow are thought to be non-uniform along the shock surface, and important constraints on the mechanism at work come from exact knowledge of where along this surface particles are being accelerated.

In Olmi et al. (2015) we use axisymmetric relativistic MHD simulations to obtain constraints on the acceleration site(s) of particles of different energies in the Crab nebula. Various scenarios are considered for the injection of particles responsible for synchrotron radiation in the different frequency bands, radio, optical and X-rays. The resulting emission properties are compared with available data on the multi wavelength time variability of the inner nebula.

Based on this analysis we discuss here the constraints on the region of acceleration of particles of different energies and the possible implications on the nature of the acceleration mechanism(s) at work at the TS.

5.1 Introduction

Pulsars and their relativistic outflows are the most powerful galactic particle accelerators, and non-thermal emission from PWNe is the best available source of information about the physics of these compact objects, including their role as antimatter factories.

The study of PWNe, and of the Crab nebula in particular, is crucial for many fundamental aspects of high-energy astrophysics, like neutron stars physics, cosmic ray production, and the physics of highly relativistic, collisionless shocks (for a recent review see Amato, 2014). The observed extremely efficient acceleration of the wind particles at the TS is in contrast with shock acceleration theories, given that ultra-relativistic, transverse shocks (the magnetic field in the wind is believed to be mainly toroidal at large distances from the pulsar) are the worst possible configuration for Fermi-type processes to operate effectively (Arons, 2012; Sironi et al., 2013).

Detailed modelling of the Crab nebula dynamics and emission, with a special attention to its inner region and careful comparison with observations, may help clarify the situation. The inner region of the Crab nebula has been known to be highly variable at optical wavelengths since the late '60s, when the so-called *wisps* were first observed by Scargle (1969). These arc-shaped bright features are periodically produced where the TS is expected to be located, the first bright ring surrounding the central dark zone. These bright arcs of emission then move radially outwards at mildly relativistic velocities, as expected for a post-shock hydrodynamic flow. Due to their apparent connection with the particle acceleration site, it is clear how a precise modelling of such features can provide clues on the physical mechanisms at work.

In the last decade, thanks to the unprecedented imaging power of *Chandra*, high resolution observations of the inner region of the Crab nebula have become available also in the X-ray band, revealing a striking *jet-torus* structure, knots and rings (Weisskopf et al., 2000), previously just barely inferred (Brinkmann et al., 1985; Hester, 1995). These observations prompted a theoretical effort at modelling PWNe, and the Crab nebula in particular, within the framework of time-dependent multi-D MHD. Axisymmetric relativistic MHD simulations of the interaction of the pulsar wind with the supernova ejecta have proven to be an excellent tool to investigate the physics of PWNe: not only the overall jet-torus structure, but even very fine details as X-ray knot and rings have been successfully reproduced (Komissarov, 2004; Del Zanna et al., 2004, 2006).

MHD simulations also provided an explanation for the Crab nebula moving wisps. After optical discovery, the latter have been studied with increasingly high accuracy at several wavelengths, from radio to X-rays (Tanvir et al., 1997; Bietenholz et al., 2001; Hester et al., 2002; Bietenholz et al., 2004; Hester, 2008; Schweizer et al., 2013). A few different interpretations have been proposed in the literature for their phenomenology. Gallant and Arons (1994) and Spitkovsky and Arons (2004) proposed their association with ion-cyclotron waves produced by the presence of relativistic ions in the pulsar wind, while Begelman (1999) proposed to interpret them as Kelvin-Helmoltz instabilities of shear flows around the TS, though Bucciantini et al. (2006) later showed that in the magnetized case this process is unlikely to play a role. In reality, the wisps find a very natural interpretation in terms of the properties of the MHD flow around the termination shock (Volpi et al., 2008; Camus et al., 2009): the periodical ($P \sim 1 - 3$ years) creation of fluid vortices around the TS, due to magnetosonic oscillations occurring on about a light-crossing time of the shock, is seen to well reproduce outward moving wisps with the observed velocities of $0.3 - 0.5\ c$. The wisps would then simply be Doppler boosted features in a turbulent and highly magnetized environment. This scenario has not basically changed in the aftermath of the first full three-dimensional MHD simulation of the Crab nebula (Porth et al., 2014), where wisps are seen to survive an even more complex flow structure, at least within the stringent limits on both resolution and length of these first simulations, imposed by the much more severe computational costs.

In spite of the successes obtained by MHD models, some questions are still unanswered. One of these, for instance, is the origin of the electrons and positrons responsible for the Crab nebula synchrotron radio emission (*radio particles* hereafter). These might have been injected in the nebula at very early stages, and then reaccelerated by local turbulence (see Chap. 4), rather than being continuously injected at the TS, as is instead the case for the higher energy pairs (*X-ray particles*). The overall synthetic spectrum from one-zone models of the Crab nebula is in fact best reproduced if two distinct particle populations are assumed, with a spectral break around the infrared band (Atoyan and Aharonian, 1996; Meyer et al., 2010). From a theoretical point of view the two scenarios are very different: if radio particles are injected as part of the outflow we expect a much higher pair multiplicity κ, and a lower wind Lorentz factor γ, (Bucciantini et al., 2011) than magnetospheric models are able to predict (Hibschman and Arons, 2001; Harding and Muslimov, 2011; Timokhin and Arons, 2013), while the most commonly accepted values of $\kappa \sim 10^4$

and $\gamma \sim 10^6$ (Kennel and Coroniti, 1984a) are those pertaining two models in which the radio electrons are a relic population of early evolutionary stages.

In order to definitely rule out one of these contrasting hypotheses, in Olmi et al. (2014) we addressed the question of radio emission morphology and integrated spectrum of the Crab nebula, for the first time by means of (two-dimensional) MHD simulations, as discussed in 4. Using the model parameters that were known to best match the Crab nebula morphology, dynamics, and emission, we tested three scenarios for the radio particles. However, due to their long cooling time, we were not able to discriminate between a steady and uniform distribution or a continuous injection as for the X-ray particles: surface brightness radio maps and characterisation of wisps motion both well agree with observations (Bandiera et al., 2002; Bietenholz et al., 2004), but the two cases are undistinguishable one from the other. The only option we could exclude is that of a relic population of low energy particles which are injected at early times ($\sim$ 100 years) and then just advected by the nebular flow. In this case the radio emission does not match the observations at all and we then concluded that, if particles are not injected as part of the wind population, some form of particle re-acceleration (by the turbulent flow or distributed reconnection events) must be continuously at work.

Another important issue to be addressed is the precise location of the acceleration of relativistic particles around the TS. An answer to this question would be particularly important in discriminating sites where shock acceleration can be more efficient. The two mechanisms that are most commonly invoked as the origin of particle acceleration at the Crab nebula TS are the first order Fermi process (the most commonly invoked acceleration mechanism in astrophysics) and driven magnetic reconnection of the striped wind, presently the best candidate to explain the particle acceleration needed to reproduce the Crab γ-ray flares above 100 MeV (Cerutti et al., 2014). Both processes require special conditions to be at work, which are not realised everywhere along the shock surface. In order for Fermi mechanism to be operative, the flow magnetisation, parametrised by the ratio of Poynting flux to particle kinetic energy flux in the wind, σ, must satisfy: $\sigma < 0.001$ (Spitkovsky, 2008; Sironi and Spitkovsky, 2011). MHD simulations taught us that, if the emission from Crab is to be reproduced, this condition can only be realised in a thin latitude strip around the pulsar equator or in the vicinities of the polar axis, while at intermediate latitudes the flow magnetisation must be substantially larger than this, and likely σ of order a few (Komissarov, 2013). As far as magnetic reconnection is concerned, this can only operate in regions where the wind

is striped (Coroniti, 1990; Lyubarsky and Kirk, 2001; Kirk, 2004; Sironi and Spitkovsky, 2011), or where there is an O-point dissipation: again these conditions are only realised around the equator and close to the polar axis respectively. In addiction for magnetic reconnection to give as broad a spectrum as observed, the pulsar multiplicity must be extremely high, much higher than theory can account for, and even so high that the wind would reconnect before the TS (Lyubarsky, 2003). The two mechanisms are also very different in terms of the particle spectrum they produce, with Fermi mechanism leading to $N(E) \propto E^{-p}$ with $p \approx 2$, appropriate to account for the energy distribution of the highest energy particles, and magnetic reconnection leading to $1 \lesssim p \lesssim 1.5$, appropriate to account for the radio particle spectrum.

One way to test the different scenarios is by comparison with observations of the variability they entail in the inner nebula at various frequencies: since the wisps are seen to start so close to the termination shock (or the location where it is supposed to be), at least at optical and X-ray frequencies, where radiative losses are important, they trace freshly injected particles, and in the simulated maps, their appearance and motion depends on the location at which the emitting particles are injected in the nebula.

In the present work we use axisymmetric MHD numerical models of the Crab nebula to infer constraints on the acceleration site(s) of the emitting particles. We consider different scenarios for the injection of particles of different energies and compare the resulting simulated wisps with available data at radio, optical and X-ray frequencies.

The motivation for using these features as probes for the particle acceleration site comes from the fact that wisps observed at various wavelengths, namely in radio, optical, and X-rays, are not coincident features and are seen to propagate at different speeds (Bietenholz et al., 2004; Schweizer et al., 2013). While the observed discrepancies between radio and optical wisps led Bietenholz et al. (2004) to conclude that the two populations must have a different acceleration mechanism and/or site, in Chap. 4 we showed that wisps are well reproduced without invoking *ad hoc* mechanisms, with the bulk flow acting as the main driver for the observed wisps appearance and motions. However, the issue of the different behaviour at various wavelengths was not addressed in detail and this is the main goal of the present work. Assuming the emitting particles are all accelerated at the TS, including the radio component (thus with a common mechanism), the discrepancies can only be explained by choosing different acceleration regions along the TS for distinct distributions. If particles with different

Wind	$L_0 = 5 \cdot 10^{38}$ erg s^{-1}	$\gamma_0 = 100$	$\alpha = 0.1$	$\sigma_0 = 0.025$
Ejecta	$M_{ej} = 6M_\odot$	$E_{ej} = 10^{51}$ erg	$v \propto r$	
ISM	$n = 1$ cm^{-3}	$T = 10^4$ K		

Table 5.1: Values of the parameters used in the simulations.

energies are injected at different angles, the paths induced by the post-shock flow structures, and the adiabatic and synchrotron losses, will be also different, thus we do not expect to see identical moving features at all frequencies, as observed.

This Chapter is structured as follows. In Sec. 5.2 we briefly recall the used configuration of the pulsar wind and the basic methods for obtaining synchrotron emission properties from MHD simulations. In Sec. 5.3 the details of synthetic data analysis of the simulated wisps are provided. Sec. 5.4 is devoted to the results in the different scenarios, and section 5.5 to the characterisation of wisps. In Sec. 5.6 the conclusions are drawn.

5.2 Simulation Details

The numerical setup is that described in Chap. 3. Here the resolution of the simulation is lowered with respect to the one presented in Chap. 4, in order to balance the computational costs and a sufficient resolution in the inner zone of the nebula. The computational box is made up of 512 cells in the radial direction and 256 cells in the angular direction.

The initial conditions are again those described in Chap. 3. We again choose values of the free parameters that best match the observations, both in terms of nebular morphology and spectral properties (Del Zanna et al., 2006; Olmi et al., 2014), recalled and summarised in Tab. 5.1.

5.2.1 Calculation of the synchrotron emission

As in our previous analyses (Volpi et al., 2008; Olmi et al., 2014), we consider two distinct families of emitting particles: those responsible for the radio emission and those emitting in the X-rays. Usually optical emitting particles are taken as part of the same population to which X-ray emitting ones belong. However, multifrequency campaigns have shown that wisps not only are different at radio and optical wavelengths (Bietenholz et al., 2004), but they also differ at optical and X-ray frequencies (Schweizer et al., 2013). As we will see in the following, this observation can only be accounted for if the injection sites of optical

and X-ray emitting particles are not perfectly coincident. A natural assumption, to have wisps that are not coincident in any two of the three observational wavebands, seems that of having radio and X-ray emitting particles injected in different sites and the optical emission produced as the sum of the contribution of radio and X-ray emitting particles.

The spectral shape that we adopt in this work is slightly more complex than that described in Chap. 3, and used in Chap. 4, with the introduction of a high energy exponential cut-off for both power-laws. Exponential cut-offs were already used by Volpi et al. (2008) and had been replaced by sharper falls of the distribution function in our previous work (Olmi et al., 2014) for the sake of simplicity. We are now forced to reintroduce them in an attempt at interpreting the optical emission as partly contributed by the low energy (radio emitting) particles. In fact, a shallower (only exponential) cut-off is crucial if one wants a substantial contribution at optical frequencies of both families of particles without overproducing the infrared emission.

The radio and X-ray emitting particles are injected with spectra respectively given by:

$$f_{0\mathrm{R}}(\epsilon_0) \propto \begin{cases} 0 & \text{if} \quad \epsilon_0 < \epsilon_{\mathrm{minR}}, \\ \epsilon_0^{-p_\mathrm{R}} \exp(-\epsilon_0/\epsilon_\mathrm{R}^*) & \text{if} \quad \epsilon_0 > \epsilon_{\mathrm{minR}}, \end{cases} \tag{5.1}$$

$$f_{0\mathrm{X}}(\epsilon_0) \propto \begin{cases} 0 & \text{if} \quad \epsilon_0 < \epsilon_{\mathrm{minX}}, \\ \epsilon_0^{-p_\mathrm{X}} \exp(-\epsilon_0/\epsilon_\mathrm{X}^*) & \text{if} \quad \epsilon_0 > \epsilon_{\mathrm{minX}}, \end{cases} \tag{5.2}$$

where ϵ_0 is the Lorentz factor of the particle at the injection site, defined in Eq. 3.27. The parameters that appear in this description, namely power-law indices and cut-off energies, are all determined based on comparison of the simulated emission with the data, and in such a way that two requirements are satisfied: 1) the integrated emission spectrum is correctly reproduced; 2) the optical emission is partly contributed by the low and high energy particle populations. The values of the parameters on which the results we discuss in the following are based are: $p_\mathrm{R} = 1.6$, $\epsilon_{\mathrm{minR}} = 10^3$, $\epsilon_\mathrm{R}^* = 2\times10^6$, $p_\mathrm{X} = 2.8$, $\epsilon_{\mathrm{minX}} = 1.5\times10^6$ and $\epsilon_\mathrm{X}^* = 10^{10}$.

As the in the case already discussed in 3, the evolved distribution functions, for both species s, at any place in the nebula and at any time, are determined by the conservation of particle number along the streamlines and by the adiabatic and synchrotron losses that particles undergo in their bulk motion. We use the expression

$$f_s(\epsilon) = \left(\frac{n}{n_0}\right)^{4/3} \left(\frac{\epsilon_0}{\epsilon}\right)^2 f_{0s}(\epsilon_0)\,. \tag{5.3}$$

Finally, the emissivity at any point in the nebula, and consequently the surface brightness maps and the total luminosity, are calculated as described in Sec. 3.4

5.3 Synthetic data analysis

We have considered several different scenarios, with particles of different energies being injected uniformly along the shock front, mainly around the polar axis, or mainly around the equatorial plane of the pulsar rotation. Various angular amplitudes of the polar and equatorial regions have also been considered.

We list below the different injection geometries. Angular extents are expressed in the upper hemisphere, but symmetry around the equator is implicit. The cases we consider are:

(1). uniform injection: particles are injected at all the angles in the nebula between 0° and 90°;

(2). wide equatorial region: polar region defined by $\theta \in [0°, 20°]$ and equatorial one by $\theta \in [20°, 90°]$;

(3). narrow equatorial region: polar region defined by $\theta \in [0°, 70°]$ and equatorial one by $\theta \in [70°, 90°]$.

A few comments on these choices are in order. Case (2) mimics a scenario in which acceleration is associated with the low-magnetization region close to the polar axis, thanks to the Fermi mechanism, or with O-point dissipation. Case (3) has been defined in order to roughly match the narrow striped wind region in our reference case with $b = 10$ (and $\sigma_0 = 0.025$). In Fig. 5.1 we show the boundaries of the injection regions for these cases, over-plotted on the flow structure around the TS.

All the choices listed above are considered for all three ranges of particle energies (radio, optical and X-ray emitting particles), namely, particles in each of those energy ranges can be injected in five different regions: wide or narrow polar cap, wide or narrow equatorial belt, and along the entire shock surface.

As far as the analysis of wisps is concerned, data are produced as a monthly output at the end of the full simulation of the Crab nebula evolution, over a period of 10 years between 950 and 960 years. Using the expressions given in Sec. 3.4, we first calculate the integrated spectra for $t = 950$ yr, in order to compute the correct normalisation of the particles spectra for each of the five injection scenarios. Once the normalisations are found, we compute the surface brightness maps, for each case and for all output times, at radio (5 GHz), optical (1 eV) and X-ray (1 keV) frequencies.

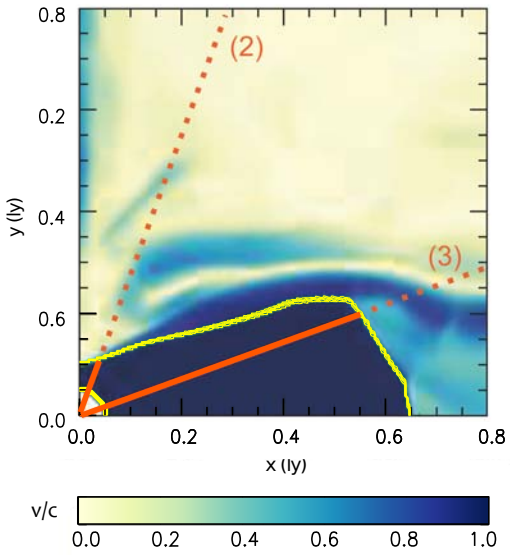

Figure 5.1: Map of the flow structure, with the inner boundary and the TS highlighted by the yellow solid line. The colours indicate the velocity magnitude in terms of c. The two orange solid-dotted lines identify the injection angular regions for case (2) and case (3).

As an example, we show in Fig. 5.2 a surface brightness map at X-ray frequencies. The emitting particles are assumed to be injected in a narrow equatorial belt (case 3). As pointed out in the introduction, the wisps appearance in our simulations is totally due to the combined effects of the locally enhanced magnetic field, just downstream of the TS, and Doppler boosting (channels with significant v/c form along the oblique sectors of the shock surface). In particular, Doppler boosting is responsible for the angular profile of wisps, as well as for the enhanced brightness of the front side of the nebula with respect to the back side, that appears very faint. The intensity contrast between distinct wisps is, on the contrary, strongly connected to the local magnetic field strength. The latter is also responsible for the suppression of most of the torus emission (again, we recall that in our axisymmetric simulations the magnetic field in the torus is quite low, $B < 10^{-4}$ G). Concluding, the brightest features are not necessarily the most boosted ones, but surely are those that highlight the magnetic field enhancements in the nebula.

For the analysis of our simulation data, we follow a similar procedure as that applied by Schweizer et al. (2013) in analysing the observations. The intensity map is cut within a 32″ radius from the pulsar and we consider a slice of width 3″ in the upper hemisphere, centred on the nebula polar axis (as shown in Fig. 5.2). For ease of comparison with real data, the intensity is convolved with the appropriate instrumental PSF and only intensity peaks

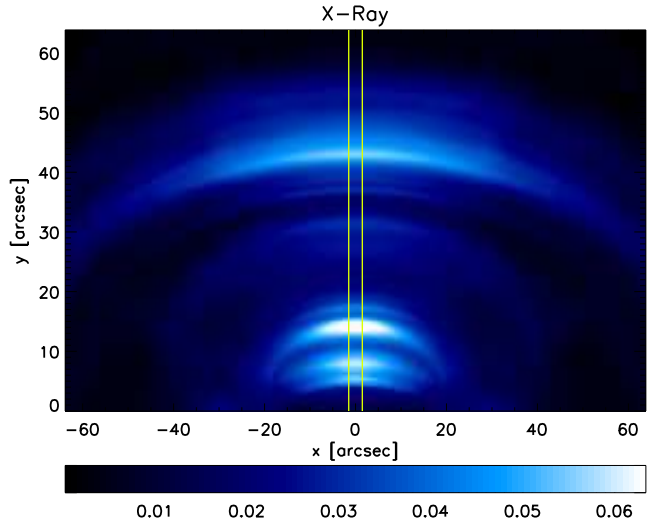

Figure 5.2: The upper emisphere of the X-ray surface brightness map (1 keV) at $t = 950$ yr, in linear scale and in mJy/arcsec^2 units. The vertical lines identify the slice used for extraction of the radial profiles.

with $I \geq I_{\max}/3$ are taken into account, where $I_{\max}$ is the maximum value of the intensity in each map. This cut is applied in order to remove the background of weaker variations, that are not useful for the comparison with the data. The PSFs employed are those of the instruments used for the observations considered for comparison in each frequency band: in particular we refer to the data analysed in Schweizer et al. (2013), Hester et al. (2002) and Bietenholz et al. (2004). The relevant observations were obtained with Chandra for the X-rays (with a FWHM=0.5″), Nord Optical Telescope (NOT) for the optical (FWHM=0.75″, as determined based on the average seeing of the period of reference), and VLA for the radio frequencies (with a FWHM=1.8″). By using this procedure we can obtain radial profiles for the maximum intensity at every time.

In the following we show two types of plots to illustrate our results: the radial distance of intensity peaks from the pulsar as a function of time, and, in order to provide information on the relative significance of the different peaks, stack plots of (properly rescaled) brightness profiles, superimposed to the corresponding positions of local maxima. A comparison of the different features, for the various options of injection, can then be achieved and it will be discussed below.

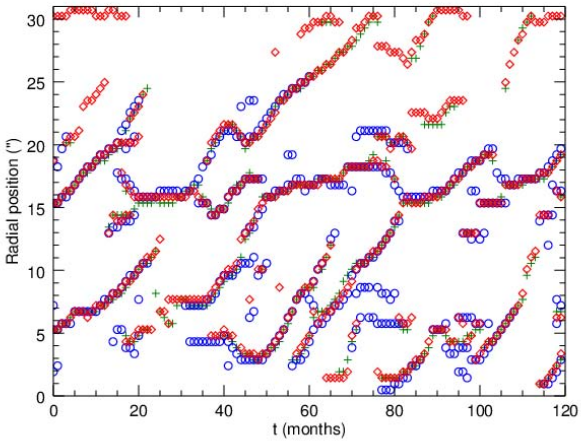

Figure 5.3: Radial position of local intensity maxima (in arcseconds) as a function of time (in months) referring to case (1) (i.e. uniform injection). Red diamonds are for radio emission, green crosses for optical and blue circles for the X-rays.

5.4 Appearance of wisps in the different scenarios and multi-band analysis

5.4.1 Radio and X-ray wisps

Let us start our analysis from the scenario in which particle injection is uniform along the shock front [case (1)]. This is the simplest assumption, though probably not the best physically motivated one, and it is also the assumption that has always been adopted so far in the modelling of the Crab nebula emission (see, however Porth et al., 2014). The natural expectation in this case is that the wisps are largely coincident at all frequencies, with differences only due to the effects of radiation losses. These might lead to the suppression, at high energies, of features that are observed at lower energy at large distance from the shock along the streamlines. Therefore differences are expected to become more apparent in the outer part of the nebula, being longer the path taken by particles to get there.

In Fig. 5.3 we show the radio, optical, and X-ray wisps positions in case (1). In agreement with expectations, the emission peaks are mostly coincident at all frequencies and at all times, with the main differences appearing at distances larger than 20" from the pulsar, where one can still see the outward motion of bright features at radio and optical frequencies, but nothing in the X-rays: this is a clear sign that losses have reduced the density of high energy particles at these places so strongly that their emission has fallen below the imposed cut-

off. In general the brightness maxima show a motion that is mostly directed outward and has a periodicity between 1 and 2 years: this is somewhat longer, on average, than seen in real data. We checked that the discrepancy is reduced when increasing the resolution of our simulations, and chose a resolution that would lead to a wisp frequency in reasonable agreement with observations, while still keeping the computational cost tolerable. Fig. 5.3 makes it clear that, in order for wisps in the inner region not to be coincident at the different wavelengths, particles responsible for the emission in different bands must be accelerated in different sites.

A short comment on the behaviour of wisps at radio wavelengths is in order. The emission map behind the profiles in Fig. 5.3 is obtained by assuming radio particles being part of the pulsar outflow and injected uniformly along the shock surface. However, in Olmi et al. (2014) we showed that there are no apparent differences between maps computed in a scenario where radio particles are part of the outflow or one in which they are taken as homogeneously distributed throughout the nebula at all times. We confirm that uniform injection limited to the shock surface and uniform injection in the whole nebula lead to the same wisp behaviour.

Here we have considered both scenarios once again and confirm our previous findings.

In Fig. 5.4 we show how the appearance of wisps changes at radio and X-ray frequencies when different injection sites are considered.

First thing that is apparent from the figure is the expected behaviour that variability at radio wavelengths always extends to larger distances from the pulsar than in the X-rays: this is simply an effect of synchrotron burn-off.

The most noticeable feature which comes out from both upper panels is the fact that for particle injection within a narrow cone around the polar axis there are basically no wisps, both at radio and at X-ray frequencies. The brightest features are more or less stationary, and the outward motion typical of wisps is rarely observed. On the contrary, when injection in a wide equatorial belt is considered, wisps appear, and they are found to be identical to those seen in the case of uniform injection (Fig. 5.3).

When the particles are injected according to the scenario named as case (3), the properties of observed wisps are qualitatively reproduced within both injection modes. The main difference between the polar and equatorial injection is now in the lack, in the latter scenario, of structures at distances from the pulsar shorter than about 6”.

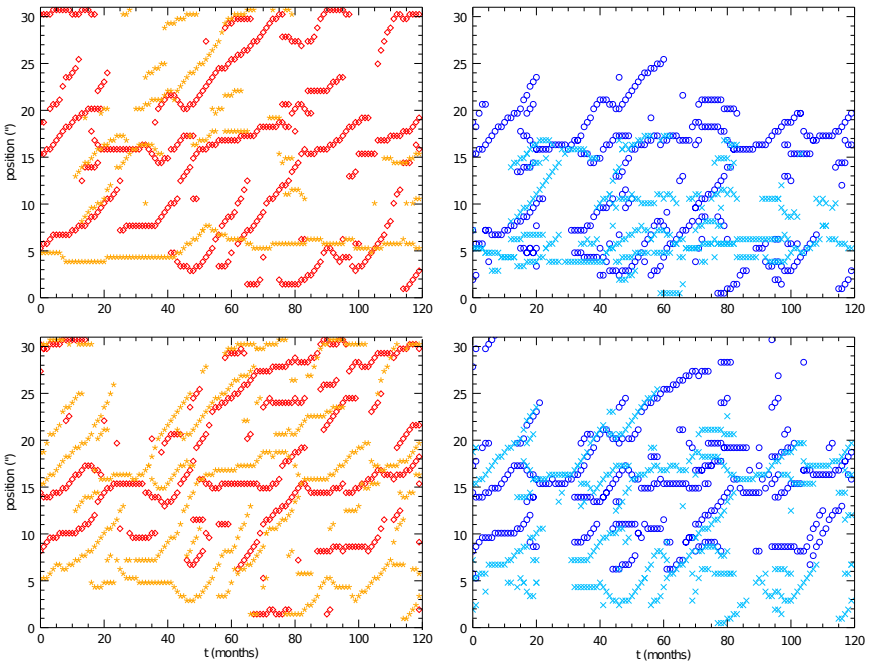

Figure 5.4: Position of the brightest features as a function of time at radio and X-ray wavelengths for different injection scenarios. Radio emission is on the left and X-ray emission on the right. The top row assumes a narrow polar cone [case (2)], while the bottom one is for a narrow equatorial belt [case(3)]. Injection at complementary angles is also shown in each panel. Top left panel: red diamonds are for radio emitting particles injected within an angle $\theta \in [20°, 90°]$, while orange asterisks are for injection in the complementary angular sector $\theta \in [0°, 20°]$. Bottom left panel: red diamonds are for injection of radio particles within $\theta \in [70°, 90°]$, orange asterisks for $\theta \in [0°, 70°]$. Top right panel: blue circles are for X-ray emitting particles injected within $\theta \in [20°, 90°]$, while light blue crosses are for injection in the complementary angular sector $\theta \in [0°, 20°]$. Bottom right panel: blue circles are for injection of X-ray particles within $\theta \in [70°, 90°]$, light blue crosses for $\theta \in [0°, 70°]$.

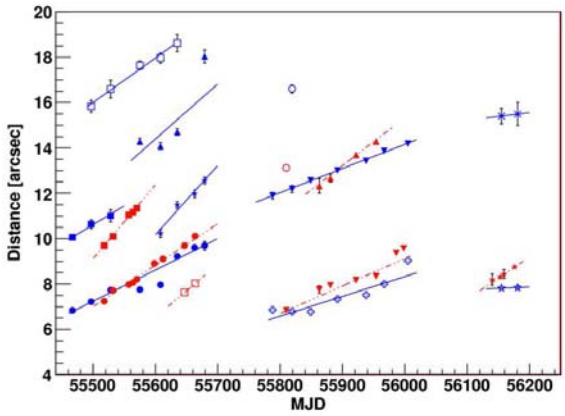

Figure 5.5: Plot of the measured optical (red) and X-ray (blue) wisp radial positions (in arc seconds) as a function of time (in days), during a period of about 2 years, as presented in Schweizer et al. (2013). As one could easily see, optical and X-ray wisps are not coincident, and no wisp-like structures are observed in the region within $\sim 6''$ from the pulsar.

From comparison between the top and bottom panels it appears that many short distance features are associated with particles accelerated at intermediate latitudes along the shock front. This appears as an important point when trying to discriminate between different acceleration scenarios. In fact, in the work by Schweizer et al. (2013) the region between 4" and 6" is found to be rather featureless, as can be easily seen in Fig. 5.5. Within the scenarios we have considered, the only one in which prominent X-ray peaks are not seen in that range of distances is one in which X-ray emitting particles are injected in a narrow equatorial belt, that is case (3), shown in the bottom right panel of Fig. 5.4.

5.4.2 Optical wisps

For the reason just discussed, in the following we focus on a scenario in which X-ray emitting particles are injected in the equatorial belt of case (3), and try to put constraints on the injection of optical emitting particles. As mentioned above, in order for optical wisps not to be coincident with X-ray ones, optical emission has to be associated with particles that have a different injection site. This condition can be satisfied if optical emission is contributed by particles that only partly belong to the high energy population, with the rest being contributed by the low-energy (radio emitting) population: in this case, differences between the X-ray and optical wisps will arise as soon as a distinct injection site for the low energy population is assumed.

Granted that the high energy particles are injected in a narrow belt around the equator, there are three obvious choices for the injection of lower energy particles within the scenar-

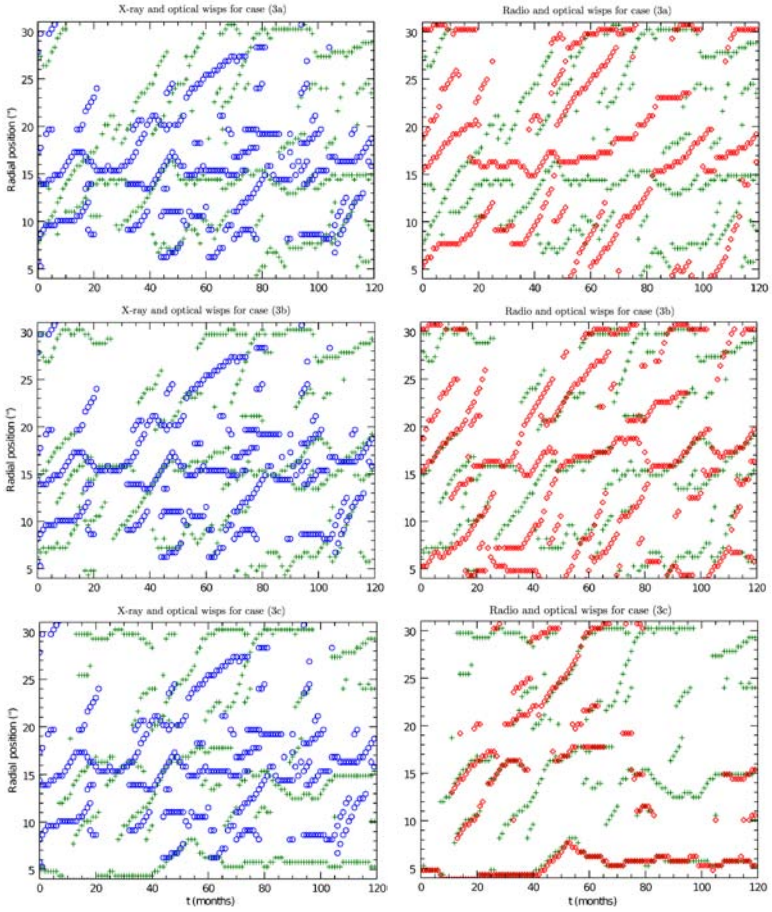

Figure 5.6: Radial distance from the pulsar of intensity peaks, as a function of time. On the left panels optical (green crosses) and X-ray (blu circles) emission profiles are compared, whereas the case of optical (green crosses) and radio (red diamonds) emission is displayed on the right panels. Here we only consider case (3) with X-ray particles injected in a narrow region around the equator $\theta \in [70°, 90°]$, while radio particles are either injected uniformly (top row), in the complementary angular sector $\theta \in [0°, 70°]$ (middle row), or in a narrow polar cone $\theta \in [0°, 20°]$ (bottom row). Radial distances are displayed for values beyond $4''$for ease comparison with Schweizer et al. (2013).

ios we have considered: (a) uniform injection; (b) injection in the complementary angular sector; (c) injection in a narrow polar cone. We show the wisps motion resulting from these three different models in the various panels of Fig. 5.6, where panels on the left refer to the comparison between optical and X-ray emission, while panels on the right side show the optical and radio cases.

We can clearly see that in all cases optical wisps are neither coincident with X-ray ones most of the time, nor to radio ones, for all our different models of injection. They typically appear at distances closer to the pulsar than the X-ray ones and extend further out. They can either lead or follow the X-ray ones. Intersections such as those observed by Schweizer et al. (2013), in spite of the limited period of observation, seem more rare in all cases. The cases with uniform injection of the radio emitting particles or injection in a wide polar cone, lead to results that are basically undistinguishable. While a noticeable difference in the case of injection in a narrow polar cone is the appearance of a stationary bright feature at a distance of about 5 ″from the pulsar, seen in optical but not in the X-rays.

A similar behaviour is found when comparing optical and radio emission. As for the case of optical and X-ray emission, we find that the kind of variability resulting from a scenario in which low energy particles are injected uniformly or within a wide polar cone is very similar. In the case of injection with a narrow polar cone, low energy particles give rise to the same bright quasi-steady feature discussed above, both at radio and optical frequencies.

5.5 Characterisation of wisps

Moving from qualitative to quantitative comparison with observations, the simplest analysis to be done is concerned with the velocity of the wisps in different wavebands. This was estimated by Schweizer et al. (2013) based on their data, and is easy to evaluate from our simulations. To this aim, in Fig. 5.7 we plot the radial emissivity profiles at radio, optical and X-ray frequencies as a function of time. The aim of this figure is that of highlighting the relative importance of the various brightness peaks. Indeed, for the velocity determination we only use the most prominent peaks. In each plot it is possible to follow the time and spatial evolution of a wisp by identifying what appears to be the same peak at a different time and position.

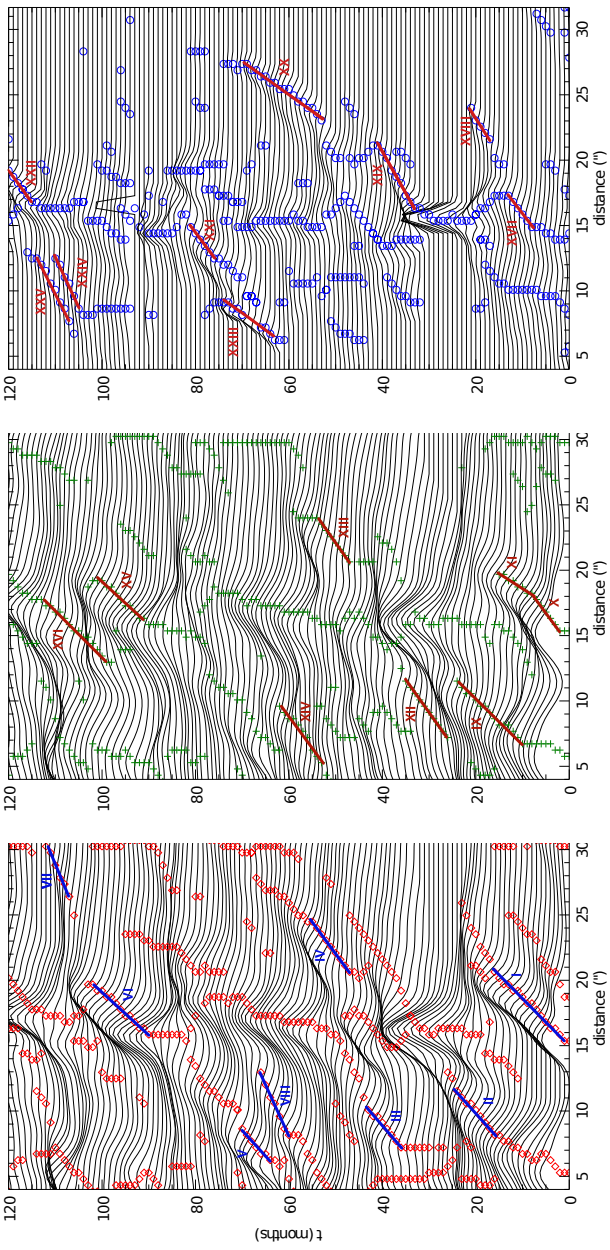

Figure 5.7: Stack plots with radial profiles of intensity radiation in the radio band (left panel), optical band (middle panel) and X-ray band (right panel). The results refer to case (3b), with injection of X-ray particles in the narrow equatorial belt $\theta \in [70°, 90°]$ and of radio particles in the complementary wide polar region $\theta \in [0°, 70°]$. Optical emission is contributed by both populations as discussed in the text. Lines and Roman numerals are used to highlight the prominent structures, and are recalled in the following for the wisp velocity evaluation (see Tab. 5.2).

Radio				Optical				X-ray			
Wisp #	$v_{\rm app}$ ($''$/d)	$v_{\rm app}/c$	v/c	Wisp #	$v_{\rm app}$ ($''$/d)	$v_{\rm app}/c$	v/c	Wisp #	$v_{\rm app}$ ($''$/d)	$v_{\rm app}/c$	v/c
I	0.012	0.14	0.16	IX	0.011	0.13	0.15	XVII	0.016	0.18	0.21
II	0.014	0.16	0.18	X	0.016	0.18	0.21	XVIII	0.018	0.21	0.24
III	0.016	0.18	0.21	XI	0.007	0.08	0.09	XIX	0.020	0.23	0.27
IV	0.015	0.17	0.20	XII	0.016	0.18	0.21	XX	0.009	0.10	0.12
V	0.013	0.15	0.17	XIII	0.015	0.17	0.20	XXI	0.013	0.15	0.17
VI	0.010	0.11	0.13	XIV	0.016	0.18	0.21	XXII	0.018	0.21	0.24
VII	0.027	0.31	0.36	XV	0.011	0.13	0.15	XXIII	0.009	0.10	0.12
VIII	0.029	0.33	0.38	XVI	0.011	0.13	0.15	XXIV	0.026	0.30	0.35
								XXV	0.023	0.26	0.30

Table 5.2: Measured apparent velocity $v_{\rm app}$ (in $''$/d) and inferred real velocity v/c for case (3), in the radio, optical and X-ray bands. Roman numerals refer to the prominent wisps shown in Fig. 5.7.

By connecting all the peaks related to a given wisp, one obtains a line that traces the evolution of that wisp (as reported in Fig. 5.7). The apparent velocity is then given by the slope of that line, and can be directly compared to that inferred from real observations of wisps. Obviously the derived velocities $v_{\rm app}$ are those on the plane of the sky, the real ones v can then be obtained by deprojection, making use of the known Crab nebula distance ($\simeq$ 2 kpc) and its inclination angle ($\simeq$ 60°) (see Weisskopf et al., 2012). Here we focus only on case (3), that is the one that better reproduces, at least qualitatively, the observed properties of the X-ray wisps. The inferred velocities $v_{\rm app}$ and v are given in Tab. 5.2.

The resulting velocities show almost the same mean values for the three families: $v_{\rm app,R} = (0.017 \pm 0.006)''$/d, $v_{\rm app,O} = (0.013 \pm 0.003)''$/d and $v_{\rm app,X} = (0.017 \pm 0.007)''$/d, that deprojected and in units of c become $v_{\rm R} \simeq v_{\rm X} \simeq 0.2c$, $v_{\rm O} \simeq 0.15c$. The deprojected velocities range is $0.08c$ to $0.38c$, and it is in good agreement with those extrapolated by the observed data: in the work by Schweizer et al. (2013) optical and X-ray wisps appear to have the same outward speeds, ranging from $0.16c$ to $0.44c$.

The projected speed of optical wisps was also estimated by Bietenholz et al. (2004), who found it to be $\lesssim 0.3c$. Based on the comparison of the optical and radio images, the authors also argue that radio wisps appear to have a somewhat lower speed than the optical ones. One could expect that the same differences should be found between X-ray and radio wisps. Unfortunately the very small differences in speed that we find in our analysis do not allow us to draw any firm conclusions on this trend.

Moreover Bietenholz et al. (2004) find that radio wisps cover a larger area of the nebula, compared to the optical ones, and typical velocities decrease with the distance from the pulsar. As expected, the simulated X-ray wisps vanish beyond 30″ (1 ly). On the contrary, many radio wisps are still visible up to 60″. A slight decrease in velocity appears around 50″, where the wisps show speeds compatible with the lower ones in Tab. 5.2.

Finally we focus on the azimuthal profile of wisps, again following the analysis by Schweizer et al. (2013). They find an angular size of the intensity profiles for the observed wisps of $\sim 35°$ in the X-rays and of $\sim 15°$ in the optical band. In our analysis we set up the same cutoff in intensity as described previously in Sec. 5.3, and contour lines are drawn for $0.5I_{\rm max}$ and $0.8I_{\rm max}$ (two examples are shown in Fig. 5.8). In order to compare our results with real data, only those structures nearest to the pulsar are considered, in the upper hemisphere. Each wisp is deprojected from the plane of the sky and then fitted with a suitable

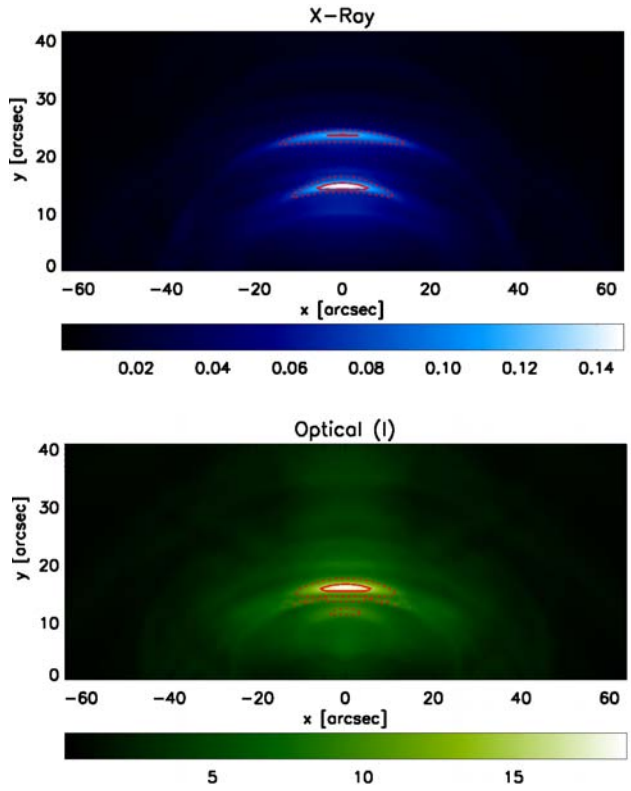

Figure 5.8: Wisps in the inner nebula with contour lines at $0.5I_{\rm max}$ (dashed) and $0.8I_{\rm max}$ (solid). X-ray in the top panel and optical in the bottom one, both in mJy/arcsec^2.

ellipse, and the angular extent is determined as the opening angle of the ellipse arc coincident with the wisp. This analysis is repeated on each one of our maps. For direct comparison with Schweizer et al. (2013) we then average all of our results obtaining $(39 \pm 12)^\circ$ for the size of the X-ray wisps and $(47 \pm 16)^\circ$ for the optical ones. The X-ray value is in perfect agreement with observations, while the optical one is overestimated.

This was already pointed out and discussed by Schweizer et al. (2013) using a toy model.

5.6 Summary and comments

In this Chapter we have tried to put constraints on the sites of particle acceleration in the Crab nebula. Our aim was to use the information deriving from studies of the nebular variability at different frequencies. The motivation for this work came from observations of the nebula at various times and at different frequencies, which have shown that wisps, namely the brightest moving features, are not coincident at the different wavelengths: wisps are distinct in radio, in optical and in X-rays. In a MHD description of the flow, where wisps only arise as a result of Doppler boosting and magnetic field enhancement, this cannot be explained, unless par-

ticles responsible for emission at different frequencies have different acceleration sites. We studied this possibility, by performing MHD simulations that assumed particle acceleration at the shock to be non-uniform. In particular we divided the shock front in complementary regions: an equatorial band and a polar cone, of varying angular extent.

We found that the properties of X-ray wisps are best reproduced if injection in a narrow equatorial band is considered. The most important piece of evidence pointing towards this conclusion is the absence of bright X-ray features very close to the pulsar. The observations by Schweizer et al. (2013) show that X-ray brightness peaks are never observed at distances from the pulsar shorter than $\sim 6''$. In our simulations we find that the lack of X-ray peaks very close to the pulsar is only obtained when injection of the particles responsible for the emission is confined to a narrow angular sector around the equator. This is easily understood by looking at the flow structure shown in Fig. 5.1. While it is clear that in the equatorial region there are no vortices and the flow is everywhere directed outwards, in the region between the lines marked as (2) and (3) vortices are seen almost at all times, though varying in position, and these are the structures responsible for the innermost brightness enhancements.

That X-ray emitting particles are most likely injected only in the vicinities of the equator was also suggested by the work of Porth et al. (2014). These authors considered two different models of injection of the X-ray emitting particles within their 3D MHD simulations: uniform throughout the shock front and equatorial only injection. Due to the modest spatial resolution of their simulation, enforced by the full 3D setup, they could only see two wisps, but were still able to conclude that equatorial injection works better at high energies, based on comparison, in the two cases, of the brightness contrast of prominent X-ray features as the jet and the anvil.

One might wonder whether and how the X-ray knot fits in this scheme, since this especially bright feature has usually been associated with the flow at relatively high latitude. While we focus here on the wrong hemisphere as far as the knot is concerned, and we would not be able to see it in any case, the question is certainly relevant. No knot is in fact obtained if X-ray emitting particles are only accelerated in a narrow equatorial sector. On the other hand, uniform injection of high energy particles along the shock front leads to a simulated knot much brighter than observed. A possibility is that some high energy particles are also accelerated at higher latitudes but with much lower efficiency, similar to what happens in the model by Porth et al. (2014), who indeed find a knot with a reasonable luminosity contrast.

The fact that different simulations, with different dimensionality, criticalities, and a focus on various observed properties, reach the same conclusion is reassuring, and might suggest that we are really pinning down the acceleration site of the highest energy particles in Crab.

Moreover we also looked at the spectral properties of the optical wisps, by computing their spectral index as in Del Zanna et al. (2006), using the specific intensities at $\nu_{\rm I} = 3.75 \times 10^{14}$ Hz (I band) and $\nu_{\rm R} = 4.6 \times 10^{14}$ Hz (R band). We measured the spectral index for each injection scenario, focusing on the most prominent wisp structures. We found that when X-ray particles are injected into the equatorial belt the spectral index is roughly uniform and its value is $\sim 0.5 \div 0.6$, in good agreement with observations (Veron-Cetty and Woltjer, 1993), regardless of the modality for radio particles injection. On the contrary, when X-ray particles are injected in the polar zone, the spectral index behaviour is not compatible with observations.

Moving to a quantitative comparison of our results with observations, one thing that is confirmed by this study is that almost all the properties of the wisps can be explained purely as a result of the MHD flow structure.

Our model reproduces the observed velocities at both optical and X-ray frequencies. In the radio band, the only available measurement to our knowledge is that by Bietenholz et al. (2004), who measure velocities of the radio wisps of order 0.3 c (see also Bietenholz et al. (2015) and Lobanov et al. (2011) for the time variability of the wisps): this is also in excellent agreement with our findings.

In our analysis we do not find any features moving with $v \sim c$: this fact, while compatible with observations, might seem somewhat surprising. In our simulations, the bulk Lorentz factor beyond the termination shock is generally below 2, but this might represent an underestimate of real velocities in the nebula, because the highest Lorentz factors are expected to be found in the polar region which in reality will be much more variable than in our axisymmetric simulations. On the other hand, the lack of observational evidence for such fast motion could be due to effective deboosting of the emitting features.

Finally, we have compared our simulation results with observations of the angular profiles of emissivity of the wisps. We found excellent agreement at X-ray frequencies, but could not account for optical observations. This problem and possible solutions to it were already discussed by Schweizer et al. (2013).

Moving to lower energies, putting constraints on particle injection based on radio emis-

sion is much more complicated, as we already partly discussed in Chap. 4. The only scenario that radio observations directly disfavour is one in which the corresponding particles are injected in a narrow polar cone: in this case variability at radio wavelengths is much reduced, radio wisps are rare and the brightness peak in this waveband is constantly found at a distance from the pulsar of order 6″.

Uniform injection and injection in a wide equatorial or polar sector lead to qualitatively very similar results from the point of view of radio emission, as can be seen from comparison of the red diamonds in Fig. 5.3 with the red diamonds in the top left panel of Fig. 5.4 and the orange asterisks in the lower left panel of the same figure. The main observed properties in this waveband are well reproduced in all these cases and even assuming a uniform distribution of emitting particles throughout the nebula.

However optical emission can be used to put additional constraints. When optical emission is compared in the different scenarios, a slight preference for uniform injection of radio particles is suggested by the fact that this leads to brightness peaks in the optical that are in general at distances from the pulsar larger than 5″, in agreement with the findings of Schweizer et al. (2013). It is also worth remarking that even at optical frequencies, we find it difficult to distinguish the emission computed in the case when radio particles are uniformly distributed through the nebula and that in which they are accelerated at the termination shock (uniformly along its surface) and advected with the flow.

On the other hand, from a more theoretical point of view, the lack of a real discontinuity in the nebular emission spectrum between the radio and X-rays suggests that the acceleration of lower and higher energy particles cannot be due to completely uncorrelated phenomena. It is natural, in a sense, to think that less extreme conditions are required to accelerate particles to the energies required for radio emission, than to bring them to the ones need to emit synchrotron X-rays. In this view, one might expect that radio particles are accelerated in a wide region, while higher energies are reached only within a portion of this region. The flat spectrum of radio emitting particles suggests that their acceleration is connected with magnetic reconnection, which is expected to occur in a region around the equator with angular width corresponding to the inclination between the pulsar magnetic and rotation axis. A possibility is that X-ray energies are then reached only in a smaller region, when field dissipation is such that the magnetization drops to low enough values to allow Fermi acceleration to occur, which would also agree with the steeper spectrum of higher energy particles. However, what

is making the acceleration of lower energy particles still stays as a very deep mystery.

Chapter 6

Beyond 2D: 3D simulations of the Crab nebula

In the last decade, numerical MHD modeling of PWNe has been extremely efficient at describing many features of these objects, down to very fine details. 2D axisymmetric simulations have been in particular optimized for describing the class prototype, the Crab nebula. Some of the most intriguing features of the Crab have been thus reproduced and explained, such as its high energy jet-torus morphology and the presence of many variable and bright features. Nevertheless many open questions still remain, as the origin of radio particles, the nature of the particle acceleration mechanism(s) working at the wind termination shock, or a correct representation of the nebular magnetic field. As previously mentioned the magnetic field morphology in 2D simulations is strongly affected by the dimensionality of the system. The lack of the third degree of freedom artificially suppresses the kink instability, which is probably essential in describing the real morphology of the field. We actually expect that the re-introduction of this third degree of freedom may lead to a more uniformly distributed field in the nebula and to a stronger magnetic diffusion, with the consequence that higher values of the wind magnetization can be considered. Cartesian The first attempt to extend 2D simulations of the Crab nebula to a 3D model was recently made by Porth et al. (2013a, 2014). The simulation is performed in Cartesian coordinates and by means of adaptive mesh refinement (AMR) in order to increase numerical resolution where it is needed to solve correctly the equations, usually in the vicinity of the origin. The numerical cost of this simulation is very heavy, and the authors are forced to reproduce only a small part of the whole evolution. Starting with a ~200 years old PWN, they let the system evolve for ~ 70 years. By inspect-

ing the overall dynamics of the simulated nebula, it appears that the expansion self-similar phase has not been reached yet, thus most of the physical informations inferred from this simulation must be handled with care.

As expected the introduction of the third degree of freedom allow the authors to rise the wind magnetization from the standard value used in 2D simulation of $\sigma \sim 10^{-2}$ to values beyond unity.

They found that the innermost structure of the nebula is perfectly comparable with those obtained with 2D axisymmetric models, meaning that MHD models are absolutely robust in describing the jet-torus morphology of PWNe. Jets are again obtained in the downstream region of the termination shock as flow collimation by the magnetic hoop stresses. The loss of axisymmetry reflects in a complex structure of the field in the 3D simulated PWN: the high ordered field no longer survives in the nebula, but it becomes more or less randomized. The toroidal component of the field is still dominant near to the TS, while near to the nebula boundaries and close to jets the polidal component becomes important.

Despite important innovations introduced by this work, some problems are still unresolved. The very short evolution time of this simulation does not allow the authors to obtain realistic emission properties from the simulated nebula. Moreover emitting properties can not be efficiently extrapolated to the actual age of the Crab ($\sim$ 1000 years), since there is no way to conveniently extrapolate the energy losses experienced by particles during their evolution. On the other hand the magnetic field can be extrapolated to $t \sim 1000$ years, but it appears to be well below the observational estimations of $\sim 200\,\mu$G (Porth private communication).

At present time it appears almost clear that 3D simulations are probably the only tool to reach a comprehensive description of PWNe in all their aspects, but more steps have to be done on that way, running longer simulations in order to reach the phase of self-similar expansion of the nebula.

6.1 A step forward

Compared with this first attempt to model in 3D the Crab nebula, our intention is to make progresses according to the following points:

1. simulate the entire Crab nebula's lifetime of $\sim$ 1000 years, in order to have a reli-

able dynamic of the system and thus independently confirm and expand the results by Porth et al. (2014).

2. compute for the first time on top of 3D simulations the entire spectrum of the Crab nebula, from synchrotron to IC emission, at the real age of the Crab, with the evolved energy pattern and magnetic field structure.

The numerical tool we decide to use is the PLUTO code, which will be introduced in the next section.

The numerical model at the basis of our 3D simulations is the one described in Chap. 3. Here we integrate the same set of RMHD equations plus the equation for the maximum energy of emitting particles (Eq. 3.3), which is the minimal requirement to infer the non-thermal emission from the nebula, since it accounts for adiabatic and synchroton losses experience by electrons. The two remaining particle tracers (Eq. 3.23 and 3.24) will be introduced later, since they are not strictly necessary in order to compute emission properties (see Del Zanna et al. (2006) or Volpi et al. (2008)) and they require a strong shock identifier to be properly normalized.

We define a cubic numerical grid of $[-10\,\mathrm{ly},\ +10\,\mathrm{ly}]^3$, with the pulsar wind injected at $t = 0$ years up to a certain r_{wind}. From inside to outside we define all the relevant physical regions as described in Sec. 3.2, with the exception of the 'primordial' PWN, which appears to be no more necessary. The radii defining the limits of the different zones are then chosen as in Porth et al. (2014), in order to optimize the comparison with their results. Namely we initialize the wind within $r_{\mathrm{wind}} = 1$ ly, the ejecta up to $r_{\mathrm{ej}} = 5$ ly and the ISM up to the box boundaries.

AMR will be used to guarantee the required refinement near to the center of the domain, where the pulsar wind is injected, while it will decrease with the distance from the pulsar dynamically, preserving an higher resolution at the wind TS and in the inner part of the nebula, more or less in the region in which the jet-torus morphology develops. Since the wind termination shock is not static but its position changes with time, we cannot use a static decomposition of the domain, and AMR is a necessary requirement. All the specific aspects connected to the used AMR levels and grid dimensions will be exhaustively discussed in the next few sections.

As in the 2D case, the wind impacts on the high density ejecta and creates the hot PWN bubble. The TS initially recedes and after a while it starts to grow, eventually reaching at

some time a self-similar expansion phase. During the whole evolution, again as in our 2D models, the wind is continuously injected following prescriptions discussed in Sec. 3.2 with a 'reset' radius of $r_{\rm reset} \sim 10^{-2}$ ly, where the finest resolution (i.e. the finest AMR level) is required. Boundary conditions at simulation edges are open, since the simulation is expected to end before the PWN reaches the boundaries.

6.1.1 The numerical code PLUTO

PLUTO is a shock-capturing, finite volume numerical code for the solution of mixed hyperbolic and parabolic system of partial differential equations, and it is probably the most widely used for classic and relativistic astrophysical MHD numerical modeling worldwide. The code was developed at the Physics Department of Università di Torino in collaboration with INAF (Osservatorio Astronomico di Torino) and the SCAI Department of CINECA [1]. The PLUTO code is freely available at http://plutocode.ph.unito.it/.

It is designed with a modular and flexible structure: different physical modules and algorithms are supplied, which may be independently combined depending on the user's necessity (Mignone et al., 2007; Mignone et al., 2012). PLUTO supports both static and adaptively refined grids. It can run on sigle workstations up to several thousand CPUs thanks to the Message Passing Interface library (MPI).

The AMR interface is supported thanks to the Chombo library [2], which provides a set of tools for implementing finite difference methods for the solution of partial differential equations on block-structured adaptively refined rectangular grids. PLUTO-Chombo is written in C and C++ and it has been extensively tested on various CINECA platforms, including the cluster FERMI[3], to achieve highly scalable performances.

As for the ECHO code, the algorithms in PLUTO follow a three-step sequence consisting of a piecewise polynomial reconstruction inside each cell, a Riemann solver between discontinuous states at zone interfaces followed by a final update where averaged conserved variables are evolved to the next time level.

[1] CINECA is the most powerful supercomputing centre for scientific research in Italy, established in 1969 in Casalecchio di Reno, Bologna.

[2] Chombo, which means 'tool' or 'container' in Swahilii language, is a software for adaptive solutions of partial differential equations. Chombo library provide a set of tools for implementing volume methods for the solution of these equations on block-structured adaptively refined grids. This library is developed by the Applied Numerical Algorithms Group, part of LBNL, an it is available at: https://commons.lbl.gov/display/chombo

[3] The supercomputing system FERMI (IBM BlueGene/P clusters) was ranked at the 7th position of the most powerful supercomputers in the world in 2012.

6.1.2 Numerical setup for 3D runs

Treating a radially propagating high-Lorentz factor wind in a 3D Cartesian grid requires very high resolutions, and it is a long term challenging problem for relativistic codes. Moreover, since the TS changes its position with time, a non-static domain decomposition is required, and the use of AMR is indispensable.

Our highest resolution has a corse grid of $[-10\,,+10]^3$ ly with 128 cells in each direction at the base level, with uniform spacing. 7 AMR refinement levels have been defined, with the last 2 levels used to rise the resolution in the innermost region of the nebula. In particular level 7 is totally devoted to resolve the region within $r_{\rm reset}$, with 0.01 ly corresponding to 16384 cells. Level 6 resolve the region within 0.1 ly, the one in which we expect the TS to evolve during the entire simulation, with 1 ly corresponding to more than 400 cells. From level 5 to level 1 resolution is progressively lowered to match the base level. Higher resolved zones are independently identified by the code in order to correctly solve the equations, especially at discontinuities and in high velocity zones.

RMHD equations are solved with a cell-centered approach, where primary physical quantities are discretized at the cell center in a dimensionally unsplit manner. The method of solution is based on a second-order discretization where piecewise linear reconstruction is used inside each region. The time integration is achieved by two-stage Runge-Kutta TVD algorithm, with a CFL number of 0.25. The high-Lorentz factor flow is managed by the selective use of the HLL Riemann solver in the most relativistic regions, or the HLLD solver (Mignone et al., 2009) for the smoother part of the system.

The solenoidal condition of the magnetic field ($\vec{\nabla} \cdot \vec{B} = 0$) is assured by the *divergence-cleaning* condition, which augments the equations with a generalized Lagrange multiplier providing the propagation and dumping of the divergence errors by means of a mixed hyperbolic/parabolic explicit cleaning step (Dedner et al., 2002; Mignone et al., 2010).

Additional dissipation in the proximity of the strong shock is assured by the *MULTID shock flattening* option[4].

Our simulations have been successively tested, optimized and ran/still running on 2048 or 4096 CPUs at the FERMI cluster.

[4]Complete details of PLUTO's facilities can be exhaustively find in the PLUTO users guide, freely downloadable at http://plutocode.ph.unito.it/files/userguide.pdf.

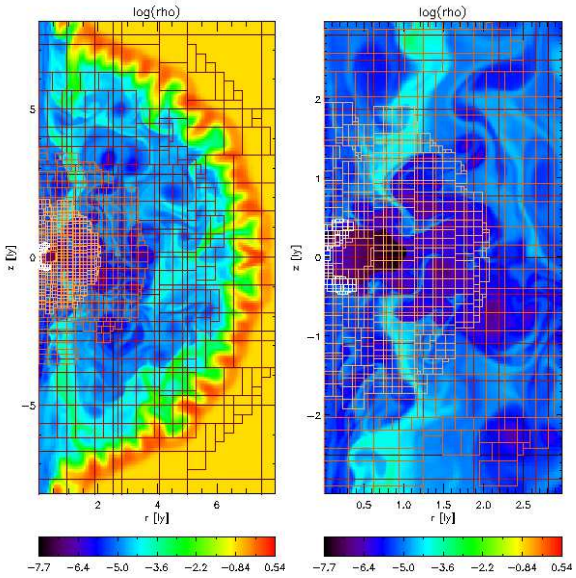

Figure 6.1: AMR levels, displayed with different colors, in two logarithmic plots of the mass density at the end of the simulation. Filamentary structures seen in the left panel at the PWN contact discontinuity, in green and red colors, are effects of the Rayleigh-Taylor instability. In the right panel a zoom of the inner region is displayed.

2D tests with low magnetization

The code was first tested with a 2D cylindrical run, in order to have direct comparison with our results from previous works. The simulation have been run on the FERMI cluster, with 1024 CPUs.

The simulation is initialized following exactly the prescriptions given in Chap. 4, with almost the same set of free parameters for the PW modelization, namely: $\sigma = 0.01$, $b = 10$, $\alpha = 0.1$. The physical domain is defined with the cylindrical radius ranging between 0 and 10 ly and z coordinate ranging in $-10\,\mathrm{ly} \leq z \leq +10\,\mathrm{ly}$, with a base level of 68x128 cells. 6 AMR levels are defined in order to increase resolution in the innermost regions, with the maximum resolution corresponding to 4352×8192 cells. Axisymmetric boundary conditions are imposed at the origin in the radial direction, while at external boundaries outflow conditions are imposed (i.e. zero gradient across the boundary).

In Fig. 6.1 different AMR levels are visible in density plots at the final time of the simulation. At the PWN contact discontinuity, located at a radius of $\sim$ 7 ly, signatures of the Rayleigh-Taylor instability are perfectly visible as fingers of dense material intruding inside the PWN bubble.

Other dynamical features are shown in Fig. 6.2. In the right panel the velocity magnitude within 3 ly from the pulsar is reported. The red region in the centre is the TS, from which

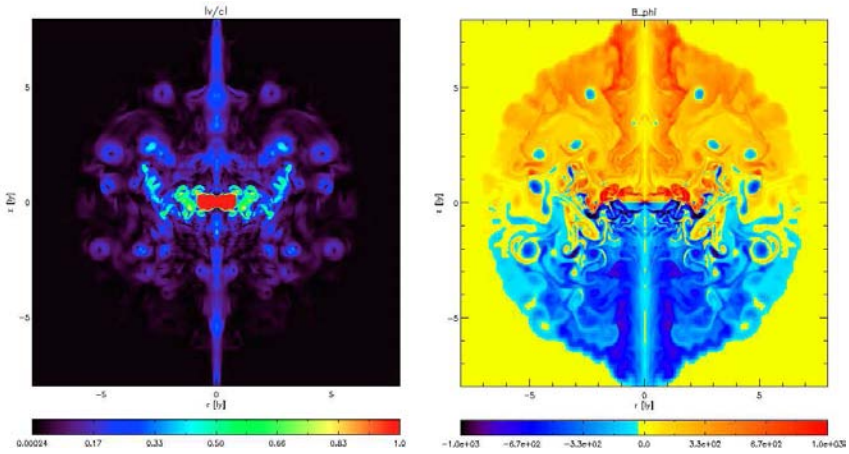

Figure 6.2: *Right panel:* plot of the velocity magnitude in the inner nebula, in units of c. *Left panel:* plot of the toroidal magnetic field in μG. On the axes the distance from the pulsar, in cylindrical coordinates, is displayed in ly units.

high velocity turbulent motion originates, giving rise to vortexes of high-speed moving material around the equatorial region. A mildly relativistic outflow is also present in the polar direction.

In the left panel of the same figure, the magnetic field structure in the whole nebula is shown. Opposite polarities of the field are shown as different colors (red/blue). The current sheet, where the magnetic field inverts, detaches from the oblique zone of the TS, and twist and tangles around the equatorial plane, causing the mixing of the opposite polarities of the field. Isolated islands of negative field polarity can be easily found in the region in which the field is predominantly positive (the upper hemisphere), and vice versa.

The overall dynamics is in good agreement with our previous findings; moreover the magnetic field appears to be less diffuse and it is a bit higher in the nebula with respect to the spherical case, probably as a combined effect of the higher resolution and of the use of the HLLD solver rather than less accurate HLL one. A qualitative comparison can be done by looking at the left panel of Fig. 3.2 and at Fig. 4.1.

Testing the 3D model on a reduced physical domain

Since a complete 3D simulation is very expensive in terms of computational time, we have first test the setup on a reduced spatial grid of $[-2.5; 2.5]^3$ ly with 32 cells in each direction at the base level and 6 AMR levels of refinement. The resulting finest grid is thus made up of $(2048)^3$ cells at level 6. This resolution was chosen in order to match the one that is supposed to be used in the full 3D simulation. Boundary conditions are imposed to be zero gradient

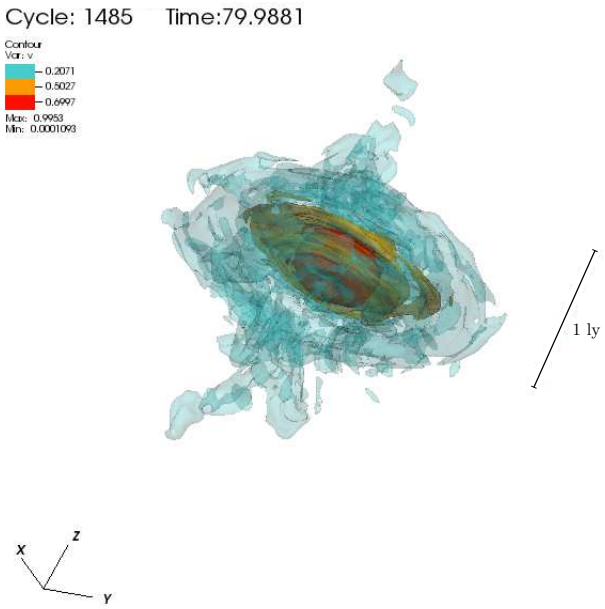

Figure 6.3: 3D representation of the velocity magnitude at $t \simeq 80$ yr. Different colors in the right-hand legend represent the chosen contours of $0.7c$, $0.5c$, $0.25c$.

in each direction, and the system was evolved for $\sim$ 80 years. This simulation was tested and ran at the Arcetri local cluster of 64 CPUs, Brahma, and it needs about 10 days to reach $t = 80$ yr. The pulsar wind is modeled with the same set of free parameters used in the 2D cylindrical test discussed previously. In Fig. 6.3 the 3D flow magnitude pattern is shown in a volumetric contour plot at $t \simeq 80$ yr, with the axes inclined as the real nebula in the plane of the sky. The jet-torus structure of the inner nebula is clearly visible. Contour surfaces are drawn for $0.7c$, $0.5c$, $0.25c$. As expected the most of the high velocity flow (i.e. $v \gtrsim 0.5c$) is confined near to the TS, in the innermost part of the nebula. Here the absence of high velocity flow in the jet regions is probably due to the chosen value of the wind magnetization, which is too low in 3D to allow efficient collimation of the equatorial flow to form powerful polar jets.

As the third dimension is introduced, the high ordered magnetic field of 2D axisymmetric simulations disappears. Kink instability and 3D turbulence tend to randomize the field, and a non-vanishing poloidal component of the field develops. In Fig. 6.4, the complex structure of the total magnetic field is shown in the left panel. As expected the toroidal component of the field still dominates near to the termination shock and in the torus region (see Fig. 6.4, right panel). However the jet region and equatorial zones far from the shock show a predominancy of the poloidal field, as can be see in the bottom panel, where the ratio B_p/B_ϕ is represented.

Figure 6.4: In the upper panel 3D contour maps of the total magnetic field magnitude (left side) and of the toroidal component alone (right side) are shown. In the bottom row, the ratio between the poloidal and toroidal magnetic field components (B_p/B_ϕ) is shown. As indicated by the color band on the left, red-orange colored zones are those with dominant toroidal field, while blue regions are predominantly poloidal.

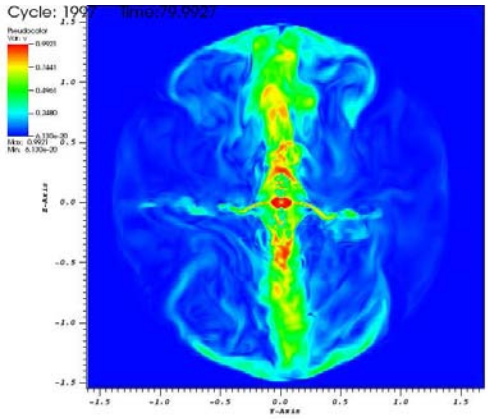

Figure 6.5: 2D slice of the velocity magnitude of the 3D simulation at $t = 80$ yr. The image shows a zoom of the inner zone of the numerical domain, where the nebula is at this stage of evolution. The red region in the center is the TS, which is much smaller than in the case with low magnetization. Moreover, the region of the jets is characterized by the presence of high velocity flows, which are absent in the low magnetized case.

Even if the magnetization in this run is still quite low, the mean value of the field in the nebula is approximatively an order of magnitude stronger than in the corresponding 2D simulation.

6.1.3 Preliminary results from the 3D simulation

At present our long-term 3D simulation is still running on FERMI at CINECA, and it has just reached $t = 80$ years of evolution. In this last section we will present some preliminary results to highlight the differences between the low magnetized case, discussed in the previous section, and the present case with high magnetization.

The used numerical setup is the one described previously in Sec. 6.1.2. The physical domain has a corse gride of $[-10\,,+10]^3$ ly, with 128 cells at the base level and 7 AMR refinement levels. The pulsar wind is again parametrized as specified in the previous sections, but here we are interested in testing higher values of the wind magnetization, and in particular this run has $\sigma = 1$.

In Fig. 6.5 a slice map of the velocity magnitude at $t = 80$ years can be seen. As expected, as one can easily deduced by a comparison with similar maps for 2D or low-σ 3D cases, here the TS shows a much smaller elongation on both the polar and equatorial directions. Moreover, a strong velocity flux is present along the z axis, where jets are expected to be.

The same behavior can be also seen in the left panel of Fig. 6.6, which can be directly compared with the low magnetized case shown in Fig. 6.3. Different colors of this 3D contour

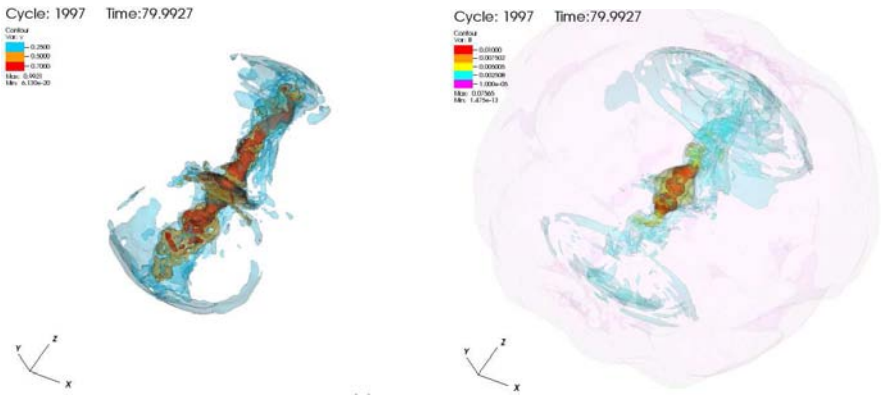

Figure 6.6: *Left panel:* representation of the velocity magnitude in a 3D contour map at t=80 yr. As in Fig. 6.3, different colors of the legend show velocity levels of $0.7c$, $0.5c$, $0.25c$. *Right panel:* 3D contour map of the total magnetic field magnitude at t=80 yr, to be compared with Fig. 6.4.

maps defines the same velocity levels: $0.7c$, $0.5c$, $0.25c$. Again we can easily see that the elongation of the TS is much smaller then in the previous case with $\sigma = 0.01$, and that the jet region is characterized by strong velocity fluxes, with fluxes moving at $0.7c$ near to the TS and in the z direction. On the contrary the equatorial region is characterized by a lower velocity with increasing the distance from the TS. Moreover at this stage of evolution the torus is still very small compared with the same stage of the low magnetized run.

Obviously the higher value of the magnetization also affected the magnetic field morphology, which can be observed in the right panel of Fig. 6.6. The maximum value of the field is enhanced by more than one order of magnitude, and highly magnetized regions are present around the shock and at the base of the polar jets.

Even if the results presented here are only preliminary, as we expected the morphology of the nebula is very different from the low magnetized case. Moreover, with this simulation we were able for the first time to reach such high value of the wind parametrization and to inspect the morphology of the resulting nebula under this hypotheses. Our findings seem in particular promising in terms of the jets formation, which is one of the problem of the simulation by Porth et al. (2014). They were in fact able to roughly reproduce the torus emission, but not the emission form jets, which are only poorly reproduced by increasing the contrast between emission from the torus and the jets themselves.

We expect to be able to reproduce a complete analysis of the emission and spectral properties of the simulated nebula in the next few months, as soon as the system will reach the self-similar phase of evolution.

Conclusions

Relativistic axisymmetric MHD simulations provide a powerful tool for the investigation of the physics of the relativistic magnetized and hot plasma in PWNe, and possibly the best tool to investigate the physical mechanisms at work in the central engine, a fast spinning, highly magnetized neutron star. While many open questions remain, the advent of relativistic MHD simulations has allowed to answer a number of problems in recent years, and has opened a promising way to answer more. The axisymmetric MHD modeling of these objects is generally regarded as very successful, especially at explaining the high energy morphology of PWNe. Within this framework, the initially puzzling jet-torus structures observed in the X-ray emission of a number of nebulae have found a straightforward interpretation as the result of the pulsar wind structure and in particular of the anisotropy of its energy flux.

The striking agreement between the simulated and observed high energy morphology of the Crab nebula suggests indeed that the flow structure in the inner regions of this object must be very close to what simulations predict (Del Zanna et al., 2006). On the other hand the same axisymmetric simulations require values of the wind magnetization of the order of 10^{-2}, which are incompatible with the integrated emission spectrum, since they lead to a nebular magnetic field which is too low to account for the whole emission. As already highlighted by Volpi et al. (2008), reproducing the synchrotron part of the spectrum requires thus conversion into accelerated particles with efficiencies larger than one, and the Inverse Compton emission results largely over-predicted.

First 3D studies on these objects seem to provide a solution to this problem. They show that kink instabilities, which are artificially suppressed in 2D, efficiently reduce the hoop stresses that force the magnetization to have such low values in 2D, allowing to reproduce the expected morphology with larger values of the magnetization. Recent works about cur-

rent driven instabilities in 3D (Mizuno et al., 2011; Mignone et al., 2013) confirm in fact the formation of kinks in jets, even if the flow arising from the termination shock and the hoop stresses in the nebula itself are not taken into account.

Preliminary work with full 3D relativistic MHD modeling of the entire system (Porth et al., 2013a,b) seems to finally provide a solution to the long-standing σ paradox: since magnetic flux can be effectively destroyed in the body of the nebula, thanks to the development of kink instabilities, even an ultra-relativistic pulsar wind at equipartition allows for the formation of a PWN with features similar to those observed in the Crab nebula, although the jets are now very weak and almost invisible. These 3D simulations only extend for a very short time ($\sim$ 70 yr) after the SN explosion, and at the end of the simulation the self-similar expansion phase has not been reached yet. Even more critical, in our view, is the fact that the average magnetic field in the nebula is already around $100\mu G$ at this very young age, and likely to decrease by a factor larger than 10 by the time the simulated nebula gets to the Crab current age. No strong conclusions can be drawn at this stage, and a further analysis must be done.

In the present work we tried to investigate some of the most important open questions in PWNe theoretical modeling.

In Chap. 3 we have presented the first attempt at a complete study of the low energy emission of the Crab nebula in the framework of 2D MHD models. Despite 2D MHD models have proven to be very powerful tools for PWNe modeling, they had never been used before to investigate lower energy emission, in spite of the fact that clarifying the origin of radio particles is fundamental in order to answer many open questions in pulsar physics. In fact, knowing whether radio emitting particles are fossil from previous epochs, or rather currently injected in the nebula as part of the pulsar wind, would allow one to constrain the wind Lorentz factor and the pulsar multiplicity κ (Amato, 2014). The question to be assessed is whether radio particles are part of the pulsar outflow, and accelerated at the TS, or if they have a different origin and/or they are accelerated elsewhere.

We approached this problem by considering three different hypotheses. In the first scenario (case A), radio particles are considered as part of the pulsar outflow, continuously injected and accelerated at the TS with the higher energies. The second possibility is that they are produced elsewhere in the nebula, for instance in the thermal filaments, and then accelerated by interaction with local turbulence (case B) (Komissarov, 2013). Finally, since radio particles are characterized by large number and long life-times against synchrotron

losses, they could be of relic origin, born in a primordial outburst of the pulsar soon after the supernova explosion (case C) (Atoyan and Aharonian, 1996).

The synthetic emission properties at radio frequencies are then compared with available data in the case of the Crab nebula. Our main conclusion is that the global radio emission is basically insensitive to the spatial distribution of the particles, as long as they are not pure relics. Whether they are currently part of the pulsar outflow or uniformly distributed in the nebula, the surface brightness maps are almost identical, and the variability of the inner regions ('radio wisps') is very similar too, which proves that within the MHD framework wisps naturally arise from the properties of the flow.

As we showed in the previous analysis, within an MHD description, wisps arise as results of regions in which the magnetic field is strong and the flow speed is high and points towards the observer.

Wisps are seen at radio, optical and X-ray frequencies, and they are not coincident at the different wavelengths, with differences measured both in term of spatial locations and of outward velocities Bietenholz et al. (2004); Schweizer et al. (2013). Within the framework of MHD, the only way to account for the different properties of the wisps at different frequencies is to assume some differences in the spatial distribution of the particles that are responsible for the emission in the different wavelengths. An obvious difference among particles of different energies (and hence emitting in different frequency bands) is the role of energy losses. However, losses are not very important in the innermost regions of the nebula from which wisps are observed. Any other difference in the spatial distribution of the particles of different energies suggests differences in the acceleration sites. In other words, if wisps are different at radio and X-ray frequencies, the particles responsible for radio emission must have had a different history than the particles responsible for X-ray emission and the simplest explanation is that they were accelerated in different locations.

In Chap. 5 we have thus performed a multiwavelength analysis of wisp properties, with the aim of constraining the history, and in particular the acceleration sites, of the emitting particles.

Essentially two acceleration mechanisms are proposed to be at work at the termination shock in the case of the Crab Nebula (Amato, 2014): Fermi I acceleration (particles gain energy through multiple crossings of the shock front) or driven magnetic reconnection (particles are accelerated by the electric fields associated with magnetic reconnection

regions). Typical spectral indices resulting from these two different processes are suitable to describe the distribution of X-ray and radio emitting particles respectively. The viability of the two mechanisms requires different physical conditions: Fermi I acceleration can be operative at relativistic shocks only where the magnetization is low enough (namely $\sigma < 0.001$) Spitkovsky (2008); Sironi and Spitkovsky (2011), while driven magnetic reconnection requires extremely large multiplicities Lyubarsky (2003); Lyubarsky and Liverts (2008); Sironi and Spitkovsky (2011).

Our analysis started with the assumption of different scenarios for the injection of particles in different energy ranges. In case (1) particles are injected uniformly at the TS surface; in case (2) we define a wide equatorial zone, with $\theta \in [20°, 90°]$ and a narrow polar one ($\theta \in [0°, 20°]$); in case (3) we define a narrow equatorial zone, corresponding to the striped region of the wind ($\theta \in [70°, 90°]$), and a wide polar one ($\theta \in [0°, 70°]$).

We found that the properties of X-ray wisps are best reproduced if injection in a narrow belt around the pulsar rotational equator is considered. The equatorial region is presumably where the flow magnetization is lower, if effective magnetic dissipation takes place in the striped wind. Then the mechanism responsible for the acceleration of those highest energy particles could be Fermi I, which has been proven to be very effective at relativistic shocks of low enough magnetization Spitkovsky (2008); Sironi and Spitkovsky (2011), and which naturally provide a particle spectral index close to that inferred from X-ray observations.

Constraining the radio emission properties is much more complicated: the only scenario that radio observations directly exclude is one in which low energy particles are injected in a narrow polar cone, since almost no wisps are found. But emission properties in the case of uniform injection, or injection in a wide polar or equatorial band, are basically indistinguishable.

Based on our findings, a possible scenario for the particle acceleration should be one in which high energy particles are injected in a narrow equatorial zone, where the magnetic dissipation is strong enough to allow Fermi I processes to be viable, while radio particles are injected in a wider region, where physical conditions are such that driven magnetic reconnection would be operative.

Finally we have presented some preliminary results from our long-term 3D simulation of the Crab nebula in Chap. 6. At present this simulation is still running at the CINECA FERMI supercomputer, and we expect to have complete information in a few months.

The aim of the work is to compare results from complete and realistic 3D simulations with observations of the Crab nebula, reproducing emission maps at multi-wavelengths and the full integrated spectrum, with special attention to the IC component. With a correct representation of the magnetic field we expect to be able to fit properly the IC spectrum, obtaining thus information on the real number of emitting particles in the wind. A correct interpretation of the IC spectral component can also infer information about the possible presence of an hadronic component in the pulsar wind (protons), which should produce photons in the γ-rays band via the Π^0 decay, $\Pi^0 \rightarrow 2\gamma$ (Amato et al., 2003).

The inferred emission properties can also confirm or discard the capability of 3D models to solve to the σ paradox, since it is not clear at all if highly-magnetized winds ($\sigma \gtrsim 1$) can efficiently account for the observed emission properties.

In conclusion, the present work represent a comprehensive study of PWNe numerical modeling, integrated with a complete set of post-processing tools for multi-wavelengths and time-variability analysis of the emission properties. The fact that the Crab nebula is so near and bright makes it the perfect object to compare with, and also a perfect laboratory to test models of extremely relativistic and magnetized plasmas. Results of 3D models, developed and optimized in the case of the Crab, and the entire set of facilities for the emission analysis, can be then applied to other relativistic objects, such as Gamma Ray Bursts (GRBs) or Active Galactic Nuclei (AGN), for which a direct inspect is much more complicated, as well as other PWNe.

List of acronyms

1. **AGN:** Active Galactic Nuclei;
2. **AMR:** Adaptive Mesh Refinement;
3. **CMB:** Cosmic Microwave Background;
4. **CR:** Cosmic Ray;
5. **GRB:** Gamma-Ray Bursts;
6. **HD:** Hydrodynamics;
7. **HLL:** Harten-Lax-van Leer Riemann solver;
8. **HLLD:** Harten-Lax-van Leer-Discontinuities Riemann solver;
9. **HST:** Hubble Space Telescope;
10. **IC:** Inverse Compton (scattering process);
11. **ISM:** Interstellar Medium;
12. **MHD:** Magneto-hydrodynamics;
13. **MPI:** Message Passing Interface library;
14. **PSF:** Point Spread Function;
15. **PW:** Pulsar Wind;
16. **PWN:** Pulsar Wind Nebula;

17. **RMHD:** Relativistic regime of Magneto-hydrodynamics;

18. **SNR:** Supernova Remnant;

19. **TS:** Termination Shock;

20. **TVD:** Total Variation Diminishing discretization scheme;

21. **VLT:** Very Large Telescope;

Bibliography

Amato, E.: 2014, *International Journal of Modern Physics Conference Series* **28**, 60160

Amato, E., Guetta, D., and Blasi, P.: 2003, *A&A* **402**, 827

Amato, E., Salvati, M., Bandiera, R., Pacini, F., and Woltjer, L.: 2000, *A&A* **359**, 1107

AMS-02 coll.: 2013, *Physical Review Letters* **110(14)**, 141102

Arons, J.: 1983, *Nature* **302**, 301

Arons, J.: 2012, *Space Sci. Rev.* **173**, 341

Arzoumanian, Z., Chernoff, D. F., and Cordes, J. M.: 2002, *ApJ* **568**, 289

Atoyan, A. M.: 1999, *A&A* **346**, L49

Atoyan, A. M. and Aharonian, F. A.: 1996, *MNRAS* **278**, 525

Bandiera, R., Neri, R., and Cesaroni, R.: 2002, *A&A* **386**, 1044

Bandiera, R., Pacini, F., and Salvati, M.: 1984, *ApJ* **285**, 134

Becker, W.: 2009, *INeutron stars and pulsars*, Springer

Begelman, M. C.: 1998, *ApJ* **493**, 291

Begelman, M. C.: 1999, *ApJ* **512**, 755

Begelman, M. C. and Li, Z.-Y.: 1992, *ApJ* **397**, 187

Bietenholz, M. F., Frail, D. A., and Hester, J. J.: 2001, *ApJ* **560**, 254

Bietenholz, M. F., Hester, J. J., Frail, D. A., and Bartel, N.: 2004, *ApJ* **615**, 794

Bietenholz, M. F., Yuan, Y., Buehler, R., Lobanov, A. P., and Blandford, R.: 2015, *MNRAS* **446**, 205

Blandford, R. D., Ostriker, J. P., Pacini, F., and Rees, M. J.: 1973, *A&A* **23**, 145

Blasi, P. and Amato, E.: 2011, *ArXiv:1007.4745*

Blondin, J. M., Chevalier, R. A., and Frierson, D. M.: 2001, *ApJ* **563**, 806

Blondin, J. M., Mezzacappa, A., and DeMarino, C.: 2003, *ApJ* **584**, 971

Blumenthal, G. R. and Gould, R. J.: 1970, *Reviews of Modern Physics* **42**, 237

Bocchino, F. and Bykov, A. M.: 2001, *A&A* **376**, 248

Bogovalov, S. and Tsinganos, K.: 2001, *Astronomical and Astrophysical Transactions* **20**, 303

Bogovalov, S. V., Chechetkin, V. M., Koldoba, A. V., and Ustyugova, G. V.: 2005, *MNRAS* **358**, 705

Bogovalov, S. V. and Khangoulyan, D. V.: 2002, *Astronomy Letters* **28**, 373

Brinkmann, W., Aschenbach, B., and Langmeier, A.: 1985, *Nature* **313**, 662

Brownsberger, S. and Romani, R. W.: 2014, *ApJ* **784**, 154

Bucciantini, N.: 2002, *A&A* **387**, 1066

Bucciantini, N., Amato, E., Bandiera, R., Blondin, J. M., and Del Zanna, L.: 2004, *A&A* **423**, 253

Bucciantini, N., Amato, E., and Del Zanna, L.: 2005a, *A&A* **434**, 189

Bucciantini, N., Arons, J., and Amato, E.: 2011, *MNRAS* **410**, 381

Bucciantini, N., Blondin, J. M., Del Zanna, L., and Amato, E.: 2003, *A&A* **405**, 617

Bucciantini, N. and Del Zanna, L.: 2006, *A&A* **454**, 393

Bucciantini, N. and Del Zanna, L.: 2013, *MNRAS* **428**, 71

Bucciantini, N., del Zanna, L., Amato, E., and Volpi, D.: 2005b, *A&A* **443**, 519

Bucciantini, N., Thompson, T. A., Arons, J., Quataert, E., and Del Zanna, L.: 2006, *MNRAS* **368**, 1717

Camus, N. F., Komissarov, S. S., Bucciantini, N., and Hughes, P. A.: 2009, *MNRAS* **400**, 1241

Cerutti, B., Werner, G. R., Uzdensky, D. A., and Begelman, M. C.: 2014, *Physics of Plasmas* **21(5)**, 056501

Chevalier, R. A.: 1976, *ApJ* **207**, 872

Chevalier, R. A.: 1977, in D. N. Schramm (ed.), *Supernovae*, Vol. 66 of *Astrophysics and Space Science Library*, p. 53

Chevalier, R. A.: 1982, *ApJ* **258**, 790

Chevalier, R. A.: 1998, *Mem. Soc. Astr. Ita.* **69**, 977

Chevalier, R. A., Kirshner, R. P., and Raymond, J. C.: 1980, *ApJ* **235**, 186

Cocke, W. J., Disney, M. J., and Taylor, D. J.: 1969, *Nature* **221**, 525

Contopoulos, I., Kazanas, D., and Fendt, C.: 1999, *ApJ* **511**, 351

Cordes, J. M., Romani, R. W., and Lundgren, S. C.: 1993, *Nature* **362**, 133

Coroniti, F. V.: 1990, *ApJ* **349**, 538

Cox, D. P.: 1972, *ApJ* **178**, 159

de Jager, O. C., Harding, A. K., Michelson, P. F., Nel, H. I., Nolan, P. L., Sreekumar, P., and Thompson, D. J.: 1996, *ApJ* **457**, 253

Dedner, A., Kemm, F., Kröner, D., Munz, C.-D., Schnitzer, T., and Wesenberg, M.: 2002, *Journal of Computational Physics* **175**, 645

Del Zanna, L., Amato, E., and Bucciantini, N.: 2004, *A&A* **421**, 1063

Del Zanna, L. and Bucciantini, N.: 2002, *A&A* **390**, 1177

Del Zanna, L., Bucciantini, N., and Londrillo, P.: 2003, *A&A* **400**, 397

Del Zanna, L., Volpi, D., Amato, E., and Bucciantini, N.: 2006, *A&A* **453**, 621

Dodson, R., Legge, D., Reynolds, J. E., and McCulloch, P. M.: 2003, *ApJ* **596**, 1137

Dubner, G. M., Velázquez, P. F., Goss, W. M., and Holdaway, M. A.: 2000, *AJ* **120**, 1933

Duyvendak, J. J. L.: 1942, *PASP* **54**, 91

Ferrand, G. and Safi-Harb, S.: 2012, *Advances in Space Research* **49**, 1313

Fesen, R. A., Saken, J. M., and Shull, J. M.: 1988, *Nature* **334**, 229

Frail, D. A., Giacani, E. B., Goss, W. M., and Dubner, G.: 1996, *ApJLett* **464**, L165

Frail, D. A. and Kulkarni, S. R.: 1991, *Nature* **352(6338)**, 785

Gaensler, B. M., Arons, J., Kaspi, V. M., Pivovaroff, M. J., Kawai, N., and Tamura, K.: 2002, *ApJ* **569**, 878

Gaensler, B. M. and Frail, D. A.: 2000, *Nature* **406**, 158

Gaensler, B. M. and Slane, P. O.: 2006, *ARA&A* **44**, 17

Gaensler, B. M., van der Swaluw, E., Camilo, F., Kaspi, V. M., Baganoff, F. K., Yusef-Zadeh, F., and Manchester, R. N.: 2004, *ApJ* **616**, 383

Gallant, Y. A. and Arons, J.: 1994, *ApJ* **435**, 230

Giacani, E. B., Dubner, G. M., Kassim, N. E., Frail, D. A., Goss, W. M., Winkler, P. F., and Williams, B. F.: 1997, *AJ* **113**, 1379

Ginzburg, V. L. and Syrovatskii, S. I.: 1965, *ARA&A* **3**, 297

Gold, T.: 1969, *Nature* **221**, 25

Goldreich, P. and Julian, W. H.: 1969, *ApJ* **157**, 869

Gotthelf, E. V., Koralesky, B., Rudnick, L., Jones, T. W., Hwang, U., and Petre, R.: 2001, *ApJLett* **552**, L39

Green, D. A. and Scheuer, P. A. G.: 1992, *MNRAS* **258**, 833

Gruzinov, A.: 2005, *Physical Review Letters* **94(2)**, 021101

Harding, A. K. and Muslimov, A. G.: 2011, *ApJ* **743**, 181

Helfand, D. J., Collins, B. F., and Gotthelf, E. V.: 2003, *ApJ* **582**, 783

Hester, J. J., e. a.: 1995, *ApJ* **448**, 240

Hester, J. J.: 2008, *ARA&A* **46**, 127

Hester, J. J., Mori, K., Burrows, D., Gallagher, J. S., Graham, J. R., Halverson, M., Kader, A., Michel, F. C., and Scowen, P.: 2002, *ApJLett* **577**, L49

Hibschman, J. A. and Arons, J.: 2001, *ApJ* **560**, 871

Hillebrandt, W., Reinecke, M., and Niemeyer, J. C.: 2000, *ArXiv Astrophysics e-prints*

Janka, H.-T.: 2007, *Astronomische Nachrichten* **328**, 683

Kargaltsev, O., Rangelov, B., and Pavlov, G. G.: 2013, *ArXiv e-prints*

Kaspi, V. M.: 1998, *Advances in Space Research* **21**, 167

Kennel, C. F. and Coroniti, F. V.: 1984a, *ApJ* **283**, 694

Kennel, C. F. and Coroniti, F. V.: 1984b, *ApJ* **283**, 710

Kirk, J. G.: 2004, *Physical Review Letters* **92(18)**, 181101

Kirk, J. G., Lyubarsky, Y., and Petri, J.: 2009, in W. Becker (ed.), *Astrophysics and Space Science Library*, Vol. 357 of *Astrophysics and Space Science Library*, p. 421

Komissarov, S. S.: 2004, *MNRAS* **350**, 427

Komissarov, S. S.: 2006, *MNRAS* **367**, 19

Komissarov, S. S.: 2013, *MNRAS* **428**, 2459

Komissarov, S. S. and Lyubarsky, Y. E.: 2003, *MNRAS* **344**, L93

Komissarov, S. S. and Lyubarsky, Y. E.: 2004, *MNRAS* **349**, 779

Komissarov, S. S. and Lyutikov, M.: 2011, *MNRAS* **414**, 2017

Livingstone, M. A., Kaspi, V. M., and Gavriil, F. P.: 2005, *ApJ* **633**, 1095

Lobanov, A. P., Horns, D., and Muxlow, T. W. B.: 2011, *A&A* **533**, A10

Lundmark, K.: 1921, *PASP* **33**, 225

Lyubarsky, Y. and Kirk, J. G.: 2001, *ApJ* **547**, 437

Lyubarsky, Y. and Liverts, M.: 2008, *ApJ* **682**, 1436

Lyubarsky, Y. E.: 2002, *MNRAS* **329**, L34

Lyubarsky, Y. E.: 2003, *MNRAS* **345**, 153

Mayall, N. U. and Oort, J. H.: 1942, *PASP* **54**, 95

Meyer, M., Horns, D., and Zechlin, H.-S.: 2010, *A&A* **523**, A2

Michel, F. C.: 1973, *ApJLett* **180**, L133

Michel, F. C.: 1974, *ApJ* **187**, 585

Migliazzo, J. M., Gaensler, B. M., Backer, D. C., Stappers, B. W., van der Swaluw, E., and Strom, R. G.: 2002, *ApJLett* **567**, L141

Mignone, A., Bodo, G., Massaglia, S., Matsakos, T., Tesileanu, O., Zanni, C., and Ferrari, A.: 2007, *The Astrophysical Journal Supplement Series* **170(1)**, 228

Mignone, A., Striani, E., Tavani, M., and Ferrari, A.: 2013, *MNRAS in press.*

Mignone, A., Tzeferacos, P., and Bodo, G.: 2010, *Journal of Computational Physics* **229**, 5896

Mignone, A., Ugliano, M., and Bodo, G.: 2009, *MNRAS* **393**, 1141

Mignone, A., Zanni, C., Tzeferacos, P., van Straalen, B., Colella, P., and Bodo, G.: 2012, *ApJS* **198**, 7

Mizuno, Y., Lyubarsky, Y., Nishikawa, K.-I., and Hardee, P. E.: 2011, *ApJ* **728**, 90

Mori, K., Burrows, D. N., Hester, J. J., Pavlov, G. G., Shibata, S., and Tsunemi, H.: 2004a, *ApJ* **609**, 186

Mori, K., Burrows, D. N., Pavlov, G. G., Hester, J. J., Shibata, S., and Tsunemi, H.: 2004b, in F. Camilo and B. M. Gaensler (eds.), *Young Neutron Stars and Their Environments*, Vol. 218 of *IAU Symposium*, p. 181

Morlino, G.: 2013, *Nuclear Instruments and Methods in Physics Research A* **720**, 70

Ng, C.-Y., Bucciantini, N., Gaensler, B. M., Camilo, F., Chatterjee, S., and Bouchard, A.: 2012, *ApJ* **746**, 105

Olmi, B., Del Zanna, L., Amato, E., Bandiera, R., and Bucciantini, N.: 2014, *MNRAS* **438**, 1518

Olmi, B., Del Zanna, L., Amato, E., and Bucciantini, N.: 2015, *MNRAS* **449**, 3149

Pacini, F.: 1967, *Nature* **216**, 567

Pacini, F. and Salvati, M.: 1973, *ApJ* **186**, 249

PAMELA coll.: 2009, *Nature* **458**, 607

Pavlov, G. G., Teter, M. A., Kargaltsev, O., and Sanwal, D.: 2003, *ApJ* **591**, 1157

Porth, O., Komissarov, S. S., and Keppens, R.: 2013a, *MNRAS* **431**, L48

Porth, O., Komissarov, S. S., and Keppens, R.: 2013b, *ArXiv:1310.2531*

Porth, O., Komissarov, S. S., and Keppens, R.: 2014, *MNRAS* **438**, 278

Rees, M. J. and Gunn, J. E.: 1974, *MNRAS* **167**, 1

Reynolds, S. P.: 2008, *ARA&A* **46**, 89

Reynolds, S. P. and Chevalier, R. A.: 1984, *ApJ* **278**, 630

Rybicki, G. B. and Lightman, A. P.: 1979, *Radiative processes in astrophysics*, Wiley-VCH, New York

Scargle, J. D.: 1969, *ApJ* **156**, 401

Schweizer, T., Bucciantini, N., Idec, W., Nilsson, K., Tennant, A., Weisskopf, M. C., and Zanin, R.: 2013, *MNRAS* **433**, 3325

Serpico, P. D.: 2012, *Astroparticle Physics* **39**, 2

Shapiro, S. L. and Teukolsky, S. A.: 1983, *Black Holes, White Dwarfs, and Neutron Stars: the Physics of Compact Objects*, John Wiley

Shull, J. M., Fesen, R. A., and Saken, J. M.: 1989, *ApJ* **346**, 860

Sironi, L. and Spitkovsky, A.: 2011, *ApJ* **741**, 39

Sironi, L., Spitkovsky, A., and Arons, J.: 2013, *ApJ* **771**, 54

Spitkovsky, A.: 2006, *ApJLett* **648**, L51

Spitkovsky, A.: 2008, *ApJLett* **682**, L5

Spitkovsky, A. and Arons, J.: 2004, *ApJ* **603**, 669

Staelin, D. H. and Reifenstein, III, E. C.: 1968, *Science* **162**, 1481

Stephenson, F. R. and Green, D. A.: 2002, *Historical supernovae and their remnants, by F. Richard Stephenson and David A. Green. International series in astronomy and astrophysics, vol. 5. Oxford: Clarendon Press, 2002, ISBN 0198507666* 5

Sturrock, P. A.: 1970, *Nature* **227**, 465

Suvorov, E. V. and Chugunov, Y. V.: 1973, *Ap&SS* **23**, 189

Tanvir, N. R., Thomson, R. C., and Tsikarishvili, E. G.: 1997, *NewA* **1**, 311

Tchekhovskoy, A., Spitkovsky, A., and Li, J. G.: 2013, *MNRAS* **435**, L1

Timokhin, A. N. and Arons, J.: 2013, *MNRAS* **429**, 20

Trimble, V.: 1982, *Reviews of Modern Physics* **54**, 1183

van den Bergh, S. and Pritchet, C. J.: 1989, *ApJLett* **338**, L69

Van Der Swaluw, E., Achterberg, A., and Gallant, Y. A.: 1998, *Mem. Soc. Astr. Ita.* **69**, 1017

van der Swaluw, E., Achterberg, A., and Gallant, Y. A.: 2002, in P. O. Slane and B. M. Gaensler (eds.), *Neutron Stars in Supernova Remnants*, Vol. 271 of *Astronomical Society of the Pacific Conference Series*, p. 135

van der Swaluw, E., Achterberg, A., Gallant, Y. A., and Tóth, G.: 2001, *A&A* **380**, 309

van der Swaluw, E., Downes, T. P., and Keegan, R.: 2004, *A&A* **420**, 937

Veron-Cetty, M. P. and Woltjer, L.: 1993, *A&A* **270**, 370

Vink, J.: 2012, *A&A Rev.* **20**, 49

Volpi, D., Del Zanna, L., Amato, E., and Bucciantini, N.: 2008, *A&A* **485**, 337

Weisskopf, M. C., Elsner, R. F., Kolodziejczak, J. J., O'Dell, S. L., and Tennant, A. F.: 2012, *ApJ* **746**, 41

Weisskopf, M. C., Hester, J. J., Tennant, A. F., Elsner, R. F., Schulz, N. S., Marshall, H. L., Karovska, M., Nichols, J. S., Swartz, D. A., Kolodziejczak, J. J., and O'Dell, S. L.: 2000, *ApJLett* **536**, L81

White, R. L. and Long, K. S.: 1991, *ApJ* **373**, 543

Woosley, S. and Janka, T.: 2005, *Nature Physics* **1**, 147

Woosley, S. E. and Weaver, T. A.: 1986, in *Bulletin of the American Astronomical Society*, Vol. 18 of *Bulletin of the American Astronomical Society*, p. 1016

Acknowledgments

First and foremost I would like to thank my supervisor Dott. Luca Del Zanna, for his guide and precious teachings, and for allowing me to grow as a person and a researcher. I would also like to give special thanks to Dott. Elena Amato and Dott. Niccolò Bucciantini for all the prolific discussions and for sharing with me their expertise. My gratitude is also extended to the entire high energy group of the Arcetri observatory, who welcomed me with open arms since the first day of my master thesis. They have been an important benchmark for me during my Ph.D. course.

I also would like to thank the referees of my Ph.D. thesis, Dott. Andrea Mignone and Dott. Francesco Rubini, for being so willing to accept the revision of this work, even with the tight schedule imposed by our bureaucracy. Special thanks to Dott. Andrea Mignone also for his precious support in my transition to the PLUTO code.

My Ph.D. colleagues have helped me immensely, sharing the same problems, fears and doubt and a lot of good and funny moments. Sara, Susanna, Lorenzo (and Lorenzo), Mirko, Giacomo, Eleonora, Greta, Claudia, thank you all guys!

Special thanks to Stefano, with whom I've started my Ph.D.: I could not find a better friend for sharing this journey. Other special thanks to Antonio, who shared with me mostly of his worries and doubts, teaching me that I am not the only one.

Dozens of people have been important and irreplaceable in my life during the last years: my friends from the Polo Scientifico, as they became my enlarged family during the years, and always supported me, sharing good and bad moments. I must thank too many people here for doing it one by one, and I really apologize for this. Guys, you know I am very proud of being one of you! Last but not least I would like to thank my family, who supports and loves me every moment, encouraging me to take the best out of every situation. And of course, I have to thank Davide, who is part of my family and the one with whom I shared everything of my life in the last nine years. I love you all.